DIVISION OF BIOMEDICAL ENGINEERING

DEPARTMENT OF HUMAN BIOLOGY

UNIVERSITY OF CAPE TOWN

Articulated Statistical Shape Modelling of the Shoulder Joint

Author:

Tewodros Alemneh

(ALMTEW001)

Supervisor:

Dr. Tinashe Mutsvangwa

Co-Supervisor:

Professor Tania Douglas

Submitted to the Department of Human Biology at the University of Cape Town in partial fulfilment of the requirements for the degree of MSc in Biomedical Engineering by coursework and dissertation.

January 2020

DECLARATION

I, Tewodros Alemneh, hereby declare that the work on which this dissertation is based is my original work (except where acknowledgements indicate otherwise) and that neither the whole work nor any part of it has been, is being, or is to be submitted for another degree in this or any other university.

I empower the university to reproduce for the purpose of research either the whole or any portion of the contents in any manner whatsoever.

Signed: Signed by candidate

Date: 27/01/2020

ABSTRACT

The shoulder joint is the most mobile and unstable joint in the human body. This makes it vulnerable to soft tissue pathologies and dislocation. Insight into the kinematics of the joint may enable improved diagnosis and treatment of different shoulder pathologies. Shoulder joint kinematics can be influenced by the articular geometry of the joint.

The aim of this project was to develop an analysis framework for shoulder joint kinematics via the use of articulated statistical shape models (ASSMs). Articulated statistical shape models extend conventional statistical shape models by combining the shape variability of anatomical objects collected from different subjects (statistical shape models), with the physical variation of pose between the same objects (articulation).

The developed pipeline involved manual annotation of anatomical landmarks selected on 3D surface meshes of scapulae and humeri and establishing dense surface correspondence across these data through a registration process. The registration was performed using a Gaussian process morphable model fitting approach. In order to register two objects separately, while keeping their shape and kinematics relationship intact, one of the objects (scapula) was fixed leaving the other (humerus) to be mobile. All the pairs of registered humeri and scapulae were brought back to their native imaged position using the inverse of the associated registration transformation. The glenohumeral rotational center and local anatomic coordinate system of the humeri and scapulae were determined using the definitions suggested by the International Society of Biomechanics. Three motions (flexion, abduction, and internal rotation) were generated using Euler angle sequences. The ASSM of the model was built using principal component analysis and validated. The validation results show that the model adequately estimated the shape and pose encoded in the training data.

Developing ASSM of the shoulder joint helps to define the statistical shape and pose parameters of the gleno humeral articulating surfaces. An ASSM of the shoulder joint has potential applications in the analysis and investigation of population-wide joint posture variation and kinematics. Such analyses may include determining and quantifying abnormal articulation of the joint based on the range of motion; understanding of detailed glenohumeral joint function and internal joint measurement; and diagnosis of shoulder pathologies. Future work will involve developing a protocol for encoding the shoulder ASSM with real, rather than handcrafted, pose variation.

ACKNOWLEDGMENT

I would like to thank my supervisor, Dr Tinashe Mutsvangwa for his continuous support, encouragement and endless patience throughout this project. Without his guidance and help, this thesis would not have been possible. I would also like to thank my co-supervisor, Professor Tania Douglas, whose advice has been especially important during the research.

I would like to thank Medical Image-based Inferencing & Distributed Diagnostics (MI^2D^2) research group in the Division of Biomedical Engineering at the University of Cape Town (UCT) for all their friendship and support over the years. Special thanks to Jean-Rassaire Fouefack for his support and advice during the research.

I would also like to extend my thanks to Jimma Institute of Technology (JIT) School of Biomedical Engineering, which gave me an opportunity to develop my career through studying at UCT. In addition, I would like to thank Professor Esayas Alemayehu, the former vice director of JIT for his special support and contribution during the scholarship process.

I would also like to acknowledge the financial support provided by CINOP Global through the Netherlands (EP-Nuffic) funded NICHE-project: NICHE/ETH/247 'Capacity Building of Biomedical Engineering Training & Research'. Special thanks to Mr Rene Nelson, the CINOP Global program coordinator.

I would also like to thank my beloved wife Azmera Michale (Azmi) you are a lovely wife and brave mother. I realize how life was challenging while raising our boy, Abenezer Tewodros alone, but you did it.

Finally, I would like to thank everyone who has helped me during my MSc.

And especially to God, who makes all things possible.

TABLE OF CONTENTS

LIST OF FIGURES

LIST OF TABLES

LIST OF ABBREVIATIONS

2D	Two-dimensional
3D	Three-dimensional
AA	Acromial angle
ASSMs	Articulated statistical shape models
CCA	Canonical correlation analysis
CT	Computed tomography
CPD	Coherent point drift
Detcov	Determinant of covariance matrix
DICOM	Digital imaging and communications in medicine
DoF	Degree of freedom
FE	Finite element
FFD	Free form deformation
GH	Glenohumeral
GHRC	Glenohumeral rotational center
GPA	Generalized Procrustes analysis
GPM	Gaussian process model
GPMM	Gaussian process morphable model
HSCL	High surface curve line
IA	Inferior angle
ICP	Iterative closest point
ISB	International Society of Biomechanics
JCS	Joint coordinate system
LE	Lateral epicondyle
ME	Medial epicondyle
MDL	Minimum description length
MISS	Manually initialized subdivision surfaces
M-rep	Medial representation
NM	Normalization method

OPA	Ordinary Procrustes analysis
PDM	Point distribution model
PLS	Partial list square
SCoRE	Symmetrical centre of rotation estimation
SMDS	Simplex mesh diffusion snakes
SPHARM	Spherical harmonics descriptors
SSMs	Statistical shape models
TS	Trigonum spinae
TSR	Total shoulder replacement

1. INTRODUCTION

1.1. Background

The shoulder joint is the most mobile, unstable and repeatedly dislocated joint in the human body. The annual incidence of shoulder disorders is estimated around 7% in the global population; their one-year and life time prevalence are estimated 10% and 50%, respectively (Van der Heijden, 1999). Currently, there is limited prevalence data for the South African context. However, data on incidence and prevalence is documented for the most popular sports in South Africa such as rugby and cricket which expose players to severe shoulder injury. For instance, according to Lynch et al. (2013), who studied university club rugby players in South Africa, dislocation and impingement are the leading clinical problems which account for 31% and 12% of all injuries, respectively.

It is now known that the biomechanics of joints can be influenced by the shape of their articular geometries (Smoger et al., 2015). Thus, insight into how the anatomy of the shoulder relates to its kinematics may aid in diagnosis of and treatment planning for different shoulder pathologies such as osteoarthritis, impingement and dislocation. Such insight may also provide clinical information for parameterising shoulder implant design. In orthopaedics, most reports on numerical modelling have been on the hip and knee joints with very limited work on the shoulder joint. This can be attributed to two reasons: firstly, joint replacement on the shoulder is less common than for hip and knee joints (Yong et al., 2008); secondly, the shoulder joint is very complex, exhibiting relatively higher mobility and more degrees of freedom, in terms of permissible movement, than other joints (Högfors et al., 1995). The latter reason makes it susceptible to soft tissue pathologies and dislocation. Additionally, there is a relatively smaller success rate in shoulder replacement outcomes compared to the hip and knee (Valstar et al., 2002), attributable to its complex construction.

Statistical shape models (SSMs) describe the shape variability of anatomy collected from different subjects. They have been used for predicting pre-morbid shapes during surgical planning and in aiding diagnosis via classification and evaluation of different pathologies (Yang et al., 2008, Sarkalkan et al., 2014). In biomechanics, SSMs have been applied in automatic image segmentation, subject-specific biomechanics models, and bone morphometry studies (Borotikar and Mutsvangwa, 2018). The main limitation of ordinary SSMs is that they do not encode kinematics information. This means that they lack the ability to explain the shape and kinematics relationship between two or more interacting objects in a complex.

An articulation model on the other hand, encodes the relative positions of multiple objects in a complex, provided the objects share articulating surfaces. Articulated statistical shape models (ASSMs) are an extension of the conventional SSM. These models combine the statistical variation of shape with variation in relative position of individual objects (Bindernagel, 2013). The relative pose of these objects relies on their natural degrees of freedom, hence the pose of one object with respect to neighbouring objects can be used to reflect anatomical joint posture.

Various studies have been reported on the development and use of ASSMs of different joints including the hip (Kainmueller et al., 2009), knee (Bindernagel et al., 2011), and wrist (Chen et al., 2014, Van De Giessen et al., 2009). However, to the best of the author's knowledge at the time of writing, there has not been any report of an ASSM of the shoulder joint.

In a healthy shoulder joint the geometries of the two main articulating surfaces, the humeral head and the glenoid cavity, correspond with regard to shape. This means that the shape of one is congruent with the shape of the other; this provides a natural space of allowable movement based on this morphology. In glenohumeral (GH) motion only part of the humerus (the humeral head) is always in contact with part of the scapula (the glenoid) at any position of the joint (Hess, 2000). Articulated statistical shape models aim to capture this correlation and encode the coupled shape variation of two or more neighbour bones in a single model. An ASSM of shoulder joint would permit the analysis and investigation of joint posture variation and kinematics and improve understanding of shoulder joint pathology (Zhu et al., 2012). Possible analyses would include determining and quantifying abnormal articulation of the joint based on the range of motion, understanding of detailed glenohumeral joint function and performing internal joint measurement. Additional ASSM applications would include the management of pathologies through prosthesis design, development of patient-specific finite element models, and surgery planning for shoulder fracture and management of osteoarthritis. In shoulder arthroplasty for instance, anatomy as well as shape, size, and orientation of the humeral head and the glenoid are the key characteristics considered during surgical planning (Karelse et al., 2007).

1.2. Problem Statement

The human body consists of different joints; from these, the shoulder joint has the highest range of motion of any joint. However, because of this range of motion and the complex morphology of the shoulder, analysing shoulder joint kinematics is challenging. Insight into shoulder joint kinematics may help to prevent shoulder injury and may improve outcomes of

surgical interventions related to the joint (Massimini et al., 2011). An ASSM of the shoulder joint may enable analysis of the variation of joint posture, determination and quantification of pathological joints based on the degree of freedom, and define the coupling of the two bones with respect to their shape and kinematics relationship. Such kinematic studies could allow investigation of clinical parameters in the glenohumeral joint.

This project aimed to develop an ASSM of the shoulder joint that encodes both the shape and the relative pose variation of two bones of the shoulder complex, namely the scapula and the humerus.

1.3. Aim and objectives

The aim of this project was to develop an ASSM of the shoulder joint using computed tomography (CT) image data. To achieve this aim, the following objectives were identified:

1. To develop a post-processing reconstruction pipeline for the CT data including identification of reliable anatomical landmarks to guide registration.
2. To develop a robust methodology to build an ASSM of the shoulder joint.
3. To validate the shoulder joint ASSM using in-correspondence data.

1.4. Project scope and limitations

The primary focus of the project was to develop an ASSM of the shoulder joint from shoulder CT images. As there were no dynamic image data available, artificial pose variation was prescribed in the training data permitting a simulation of the three orientation motions (abduction, flexion and internal rotation). The research used International Society of Biomechanics (ISB) standards for deriving the motions. However, the artificial motion was limited to 50^{o} from a 0^{0} position in order to remove correlation between shape and pose in the training data.

1.5. Ethical considerations

This research study relied on CT image data of cadaveric specimens. The images were obtained in a previous study under ethical clearance by the University of Cape Town's Human Research Ethics Committee (HREC: 2013/060). Ethical approval for using the images for this project was granted by the same committee (HREC: 419/2018). The specimens had been obtained, with permission, from the Department of Human Biology, Faculty of Health Sciences, University of Cape Town.

1.6. Dissertation overview

This thesis is structured as follows: A review of the literature related to the project is presented in Chapter 2. Chapter 3 provides a project overview and materials used in the project. Correspondence establishment, generation of synthetic pose variability and the development of the ASSM of the shoulder joint, are described in Chapters 4, 5 and 6, respectively. Finally, Chapter 7 presents the discussion, conclusion, and recommended future work.

2. LITERATURE REVIEW

2.1. Anatomy of shoulder

The shoulder complex is composed of several tissue types including bones, ligaments, tendons, muscles, nerves, blood vessels and burse. The bony structure of the shoulder complex (Figure 2.1) consists of the musculoskeletal system of the proximal humerus, the clavicle, and scapula (shoulder blade) (De Groot et al., 1999). The humerus is one of the longest bones of the upper arm; its proximal portion composed of the humeral head, surgical neck, greater tuberosity, and lesser tuberosity. The greater tuberosity is located laterally on the humeral head and it is serves as the insertion site for the three rotator cuff muscles known as supraspinatus, infraspinatus, and teres minor. The lesser tuberosity is a smaller tubercle which is located anteriomedially. The anatomical neck provides attachment to the articular capsule of the joint.

The scapula is the other major bony component of the shoulder and serves mainly as a muscle attachment site for muscles that stabilise the joint and instantiate motion. The anatomy of the scapula includes the acromion, the coracoid process, glenoid cavity and the supraglenoid tubercle. The acromion serves as a lever arm for the deltoid muscle and articulates with the distal end of the clavicle to form the acromioclavicular (AC) joint (Terry and Chopp, 2000). The coracoid process extends anteriorly and laterally from the upper border of the head of the scapula that serves as attachment points for ligament and muscle. The glenoid cavity is found on the scapula and articulates with the head of the humerus to form the shoulder joint. The supraglenoid tubercle is a small projection found at the superior margin of glenoid cavity that serves as the origin cavity of the long head of the biceps muscle.

The anatomical joints in the shoulder complex include the shoulder joint (glenohumeral (GH)) joint, the AC joint and the sternoclavicular (SC) joint (Figure 2.1). The shoulder joint is a synovial ball-and-socket joint formed by the articulation of the head of the humerus in a shallow socket of the glenoid (specifically with the glenoid fossa). However, the glenohumeral joint does not act as a simple ball-and-socket joint due to the complex articulation between the humerus and the glenoid (Lee and Lee, 2010).

The shoulder joint is the most mobile and unstable joint in the human body, regardless of the support afforded by ligaments, tendons, and muscles. This instability is due to disproportional surface area of the glenoid and humeral head articulating surfaces; i.e. the large spherical humeral head articulates against the small shallow socket of the glenoid cavity. Around 30% of the articulating surface of the humeral head is covered by the glenoid surface during articulation (Owaydhah et al., 2017, Moore et al., 2013, Lugo et al., 2008); hence, the

congruency between the two articulating parts is small compared to other ball and socket joints. The shoulder joint is surrounded by different group of muscles, such as the supraspinatus, infraspinatus, teres major and subscapularis which converge from the scapula to the humerus (McMinn, 2005). These four muscles assist in stabilizing the humeral head to the glenoid.

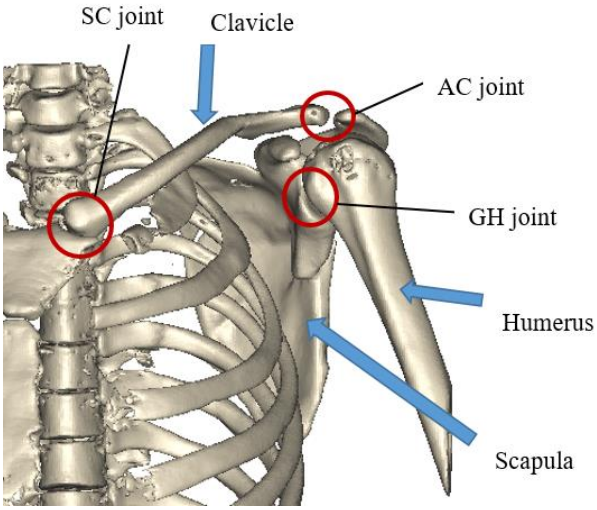

Figure 2.1. The shoulder girdle

2.2. Glenohumeral joint kinematics

Kinematics deals with the motion of objects without considering the causes of motion. Shoulder kinematics describes the shoulder joint geometrical motion according to its degrees of freedom (DoF). Biomechanical studies on the shoulder joint help to assess shoulder injury and improve surgical treatment modalities for shoulder pathologies (Massimini et al., 2011). The shoulder joint is the centre of movement of the shoulder complex and allows for a range of motions in three anatomical planes (Kadavkolan and Jawhar, 2018, Culham and Peat, 1993). The three orthogonal anatomical planes: coronal, sagittal and transverse; describe the location and orientation of the human body structures (Figure 2.2). The coronal plane separates the body into ventral and dorsal parts. The sagittal plane separates the body into the right and left parts. Finally, the transverse plane divides the body into upper and lower parts.

The shoulder joint movement incorporates three DoFs over a large range of motion (figure 2.3) known as: abduction/adduction - an articulation from 150-180^0 in the coronal plane; flexion/extension in the sagittal plane, representing 0 to 180^0 and 40-60^0, respectively; as well as medial/lateral rotation representing motion of up to 90^0 in the transverse plane (Haering et al., 2014).

- **Abduction** refers to movement of the arm away from the midline.
- **Adduction** refers to the movement of the arm towards the midline.
- **Flexion** refers to the movement that decreases the angle between the two articulating bones.
- **Extension** refers to the movement that increases the angle between the two articulating bones.
- **Internal rotation** represents the movement of the arm medially along the longitudinal axis.
- **External rotation** describes the movement of the arm laterally along the longitudinal axis.

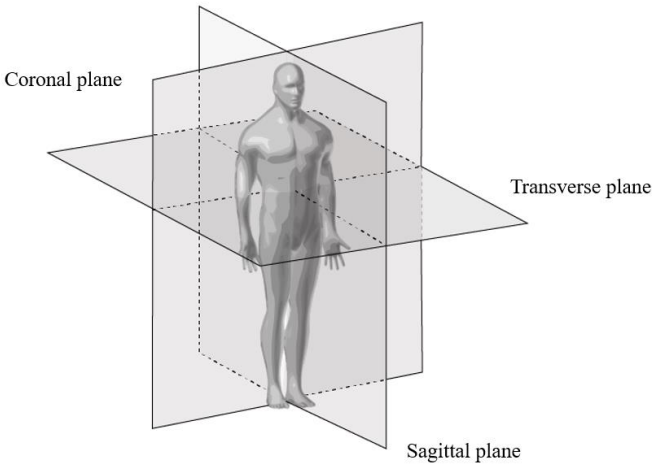

Figure 2.2. Anatomical planes of the human body

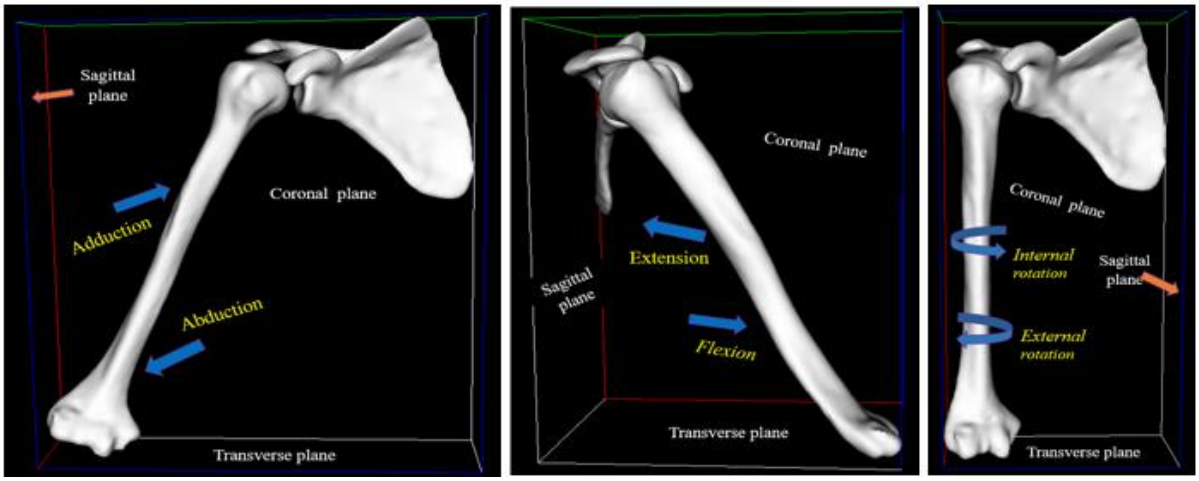

Figure 2.3. The shoulder joint and different motion types

2.3. Anatomical coordinate systems

The anatomical coordinate system is a continuous space in two- or three dimensions (2D/3D, respectively) in which anatomical objects can be represented. In defining the anatomical coordinate system in 3D rigid body, three non-collinear identification points are required so that local anatomic coordinate system can be constructed.

A joint coordinate system (JCS) is used to describe the comparative position and orientation of two adjacent bony segments such as the humerus relative to the scapula. The JCS of the shoulder is used to quantify the standardized local axis system and provides a more functional description of the rotation at a joint (Wu et al., 2005). The humerus coordinate system (HCS) (figure 2.4a) represents the moving JCS relative to the scapula in shoulder kinematics. The HCS is defined using the bony landmarks on the two lateral (LE) and medial (ME) epicondyles, as well as the glenohumeral rotational centre (GHRC) (Meskers et al., 1997). The GHRC can be estimated by using either predictive or functional methods (Lempereur et al., 2010). The predictive method computes GHRC based on the relationship between specific anatomical landmark positions (Meskers et al., 2007). On the other hand, the functional method defines the GHRC based on the relative motion of adjacent body segments (Halvorsen, 2003, Gamage and Lasenby, 2002).

Several functional methods have been reported for determining the kinematic joint rotation center of ball joints (Ehrig et al., 2006). These include the “instantaneous helical axis” (Woltring et al., 1985), “symmetrical centre of rotation estimation (SCoRE)” (Ehrig et al., 2006), “bias compensated approach” (Halvorsen, 2003), “regression method” (Meskers et al., 1997), and “sphere fitting” (Rachakonda et al., 2017). The accuracy of three of the functional methods above, namely regression, sphere fitting, and helical axis, has been evaluated. The sphere fitting and helical axis methods were reported to be the most reliable methods for locating the GHRC (Stokdijk et al., 2000). The helical axis method calculates both the center and the axis of rotation. The sphere fitting method on the other hand, can only compute the rotational center.

The scapular coordinate system (Figure: 2.4 b), which represents the reference JCS, is defined by using three anatomical bony landmarks, namely: trigonum spinae (TS), inferior angle (IA), and acromial angle (AA).

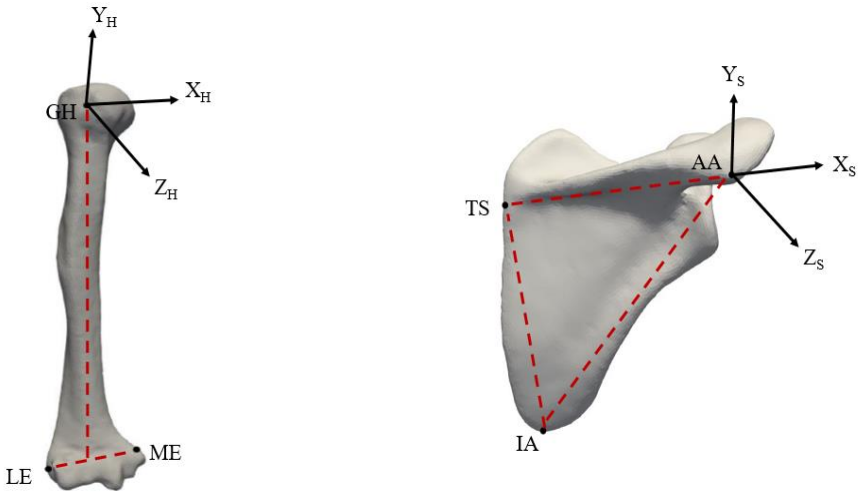

a b

Figure 2.4. Anatomical coordinate system: a) humerus b) scapula

2.4. Statistical shape models - overview

A shape is any geometrical information which is invariant to translation , rotation and scale effects (Stegmann and Gomez, 2002). Statistical shape models (SSMs) describe the mean shape and the modes of variation from a set of training examples (Cootes et al., 1995). Statistical shape models have been used in patient-specific reconstruction of healthy joints, implant design, surgery planning as well as for the development of finite element (FE) models (Mutsvangwa et al., 2014, Sarkalkan et al., 2014). Bryan et al. (2009) used a SSM to design and apply a biomechanical FE model of the femur bone. Gregory et al. (2007) exploited SSMs of the femoral head and neck to examine the differences in hip osteoarthritis between healthy and pathological subjects. Poltaretskyi et al. (2017) used a SSM of the proximal humerus to predict the pre-morbid proximal humeral anatomy. Specific to the shoulder joint, Yang et al. (2008) reported on shape prediction of the scapula and humerus in the glenohumeral joint using canonical correlation analysis (CCA) and partial least square regression (PLS) method. The above studies indicate that SSMs can be useful for quantifying various bone related-pathologies. However, the studies mentioned above only consider single object SSM. The utility of such kind of models is limited especially when considering shape correlation in articulating bones.

2.5. Statistical shape models – theoretical overview

Developing a SSM from medical image data often includes segmentation and reconstruction of 3D surfaces; identification and selection of anatomical landmarks; alignment of samples in the datasets through rigid and non-rigid registration; and development of the

SSMs (Sarkalkan et al., 2014). The methods and choice of algorithms used, however, depend on the type of objects to be modelled, particularly the complexity of the anatomy. Below is a description of each of the steps above and the different approaches reported in the literature to perform each step.

2.5.1. Segmentation

Image segmentation is a process of identifying and labelling non-overlapping regions within an image into specific component regions based on different features such as intensity and texture (Swamy and Holi, 2012, Pham et al., 2000). Different segmentation approaches exist but all can be categorised according to the level of user-participation required; i.e. manual, semi-automatic and fully-automatic methods. Manual segmentation is simple to implement but is tedious and time consuming for the operator. On the other hand, fully automatic methods have some limitations in terms of providing accurate labels of regions of interest. Any of the approaches can involve bottom-up only strategies such as intensity-based segmentation or employ top-down strategies such as model-based segmentation; or a combination of both strategies. Model-based segmentation uses prior knowledge in the form of analytical or statistical models of training example data and includes methods such as active contour, atlas, and deformable models (Nguyen et al., 2007, Pham et al., 2000, Schmid et al., 2011). Intensity-based segmentation operates on the intensity distribution of pixels in the images. It relies on the similarity of localized space features which includes edge detection, thresholding, region growing, and region mapping (Swamy and Holi, 2012). Edge detection segmentation is a method of identifying pixels on a region boundary of the image. The edge of the image can be obtained by measuring the gray value differences between adjoining pixels (Kaganami and Beiji, 2009). The region growing segmentation strategy involves selecting random pixels in the image and merging these to neighbour pixels based on similarity, to the region; the process is repeated until all the pixels belongs to some region (Ning et al., 2010, Sharma et al., 2012). Region growing can provide a better results with less noise, however, it is time consuming when the image is either noisy or has higher intensity variation (Sharma et al., 2012).

A number of model-based segmentation approaches have been applied to the different body joints such as knee (Williams et al., 2003, Fripp et al., 2007), and hip (Xia et al., 2014, Schmid et al., 2011, Chandra et al., 2014). However, there exists limited reports on bone segmentation using model-based approaches in the shoulder region (Yang et al., 2015).

When dealing with computed tomography (CT) data, bony structures are often segmented by intensity-based methods such as thresholding. Threshold-based segmentation

groups pixels according to their intensity values (Kumari, 2017). However, for articulated joints, segmentation may be more tedious using thresholding techniques alone (Kainmueller et al., 2008, Liu et al., 2008, Yogamangalam and Karthikeyan, 2013) because different bones present with similar intensity values, and also because partial volume effects can blur voxel intensities, causing multiple bones to appear fused together.

Once the volumetric datasets are segmented and extracted from the labelled images, 3D triangular surface meshes can be created. The 3D triangular mesh is a construction of the labelled regions consisting of a set of triangles that are connected by common edges. The Marching Cubes algorithm (Lorensen and Cline, 1987) is a well-known method for generating triangular mesh models of constant density surfaces from 3D medical data. On triangulated model, the topological quality of a triangular mesh is measured by the average number of vertices around each vertices of the triangulation (Delingette, 1999). Landmark points are used to guide registration of surface data in order to establish correspondence.

2.5.2. Landmarking

Landmarks in this document refer to sets of points on the 3D mesh models. These can be a sparse set that are manually annotated but the notion of landmarks can be also be extended to mean the vertices describing the full mesh. The density of landmarks describing a shape should be appropriately determined across the sample population. Too few landmarks can generate models which are not anatomically descriptive of the objects being modelled. Conversely, too many landmarks may result in noise being obtained in the model (Hutton et al., 2001).

Correspondence between landmarks across a population of shapes is a key step in the shape modelling process. Establishing correspondence entails finding a one-to-one mapping at homologous anatomical sites across the examples of shape objects. The level of difficulty in establishing correspondence ranges from relatively easy for a sparse landmark set; up to difficult for sophisticated and complex non-rigid registration required to obtain dense correspondence. A successful strategy for dense shape matching from the literature involves a two-step process: 1) Use a sparse set of easily identifiable landmarks to align the surface data; 2) Use non-rigid registration to obtain a dense one-to-one correspondence where all the vertices in a reference sample can be used in the shape analysis (Bookstein, 1997, Lorenz and Krahnstöver, 2000, Cates et al., 2007).

2.5.3. Shape registration

Registration is defined as the process of finding an optimal transformation that aligns the corresponding positions of two or more shapes or images (Oliveira and Tavares, 2014). Shape

registration is particularly focused on the mapping of 3D surface meshes of biological objects. Since rigid bodies of the same species of biological structure often exhibit high morphological variability, it is often necessary to register objects at both a global and also a local level. Global registration often entails a simple rigid alignment of the objects, while local registration requires elastic non-linear transformations between the source and target objects.

Rigid registration consists of translations and rotations that enable alignment without object deformation. Once landmarks are selected, object alignment should be performed i.e., all the 3D datasets should be transformed into the same coordinate system. The iterative closest point (ICP) method (Besl and McKay, 1992) is one of the methods used for such transformations. The ICP algorithm seeks first to establish an alignment between the shapes and then candidate correspondence between features is derived, post alignment. The process is repeated until an operator defined convergence criterion for alignment and correspondence is met. The main drawback of ICP is that it requires a very good initialization in order not to settle on local minima during the optimization process (Heimann and Meinzer, 2009).

Non-rigid registration allows deformations between surfaces to be defined by affine, projective and curved similarity transformations on top of translation and rotation (Oliveira and Tavares, 2014). Various methods for non-rigid registration have been proposed including high order graph matching (Zeng et al., 2010), thin plate splines (TPS) (Bookstein, 1989), Möbius voting algorithm (Lipman and Funkhouser, 2009), coherent point drift (CPD) (Myronenko et al., 2007), simplex mesh deformable model (Delingette, 1999), simplex mesh diffusion snakes (SMDS) (Tejos et al., 2009), and more recently, Gaussian process model fitting (Gerig et al., 2014).

A Gaussian process is a generalization of a multivariate normal distribution to infinitely many variables such that it allows for defining distributions over functions (Rasmussen, 2006). A Gaussian process $GP(\mu, k)$ is defined by its mean, $\mu: \Omega \rightarrow \Re^2$ and a covariance function or kernel, $k: \Omega * \Omega \rightarrow \Re^{2*2}$. The mean function defines the mean deformation $\mu(x)$ for every point $x \in \Omega$; the covariance function defines the covariance $k(x, x^i)$ between any deformation for points x and x^i (Ledoit and Wolf, 2004). A Gaussian process registration involves computing shape deformations between the target object and reference object (see Section 2.5.5 for more detail on Gaussian process models).

Gaussian process model fitting has been reported as a method for establishing dense correspondence through deforming a reference mesh to fit the target mesh (Lüthi et al., 2018). If the deformed reference mesh represents the target mesh adequately, then it can replace the

original target and both objects, reference and deformed reference, will be in-correspondence. This correspondence establishment process is made possible by developing a free form deformation model (FFDM) of the reference mesh prior to fitting; the FFDM is able to warp on the target mesh in what is essentially a non-rigid registration process.

2.5.4. Alignment of in-correspondence shapes

Once dense correspondence has been established across the training shape data, all shapes are realigned to remove position, scale, and rotation effects in order to eliminate any variation not attributable to shape differences. Often the shape alignment process requires minimization of metrics such as the Hausdorff distance (Hausdorff, 1918), strain energy (Sclaroff and Pentland, 1995), and the Procrustes distance (Bookstein, 1997, Dryden and Mardia, 1998). The former two can be applied to datasets with an unequal number of landmark points, while Procrustes distance can only be applied to objects having equal sets of corresponding points. Procrustes analysis exists in two forms; when a single object is aligned on to another, this is referred to as ordinary Procrustes analysis (OPA). When three or more objects are aligned by superimposition, this is referred to as generalized Procrustes analysis (GPA) (Gower, 1975); According to Stegmann and Gomez (2002), the alignment procedure in GPA follows the following steps:

i. Select one random training set as reference shape.
ii. Superimpose all example data with respect to the reference shape at their centroids.
iii. Compute a mean shape from superimposed datasets and set the reference to the mean shape.
iv. Iterate step (ii) to step (iii) until the difference between the mean shape and the reference falls below the threshold.

When the perfect matching occurs, the shapes in the datasets said to be aligned.

2.5.5. Shape model building from in-correspondence data

After alignment of the in-correspondence data in the training dataset, the shape model can be developed by establishing the mean shape and the modes of variation. To find a small set of modes that best describe the observed variation, the dimensionality of the data sets should be reduced. This is often done using principal component analysis (PCA). Principal component analysis (PCA) is a statistical procedure that uses an orthogonal transformation to convert a set of observations of possibly correlated variables into a set of values of linearly uncorrelated variables called principal components (PCs) (Jolliffe and Cadima, 2016). The largest

proportion of the total variance in the data is represented by the first PC. The second largest proportion of the variance is represented by the second PC, and so on for all PCs.

Traditionally, a class of SSMs known as point distribution models (PDMs) were developed by modelling distributions over meshes in-correspondence. More recently, the modelling can be performed over the set of deformation fields from each shape object towards the reference mesh. This class of SSM are called Gaussian process morphable models (GPMM) (Lüthi et al., 2018) and the resultant SSM can be represented using equation (2.1), which is known as the Karhunen-Loève (KL) expansion of the Gaussian process (Berlinet and Thomas-Agnan, 2011). More concretely, every deformation (u), is represented by the Gaussian process, $u \sim GP\ (\mu, k)$ such that $\mu: \Omega \rightarrow \Re^2$ represent the mean function and $k: \Omega * \Omega \rightarrow \Re^{3*3}$ represent the covariance function. These functions represent mean deformation $\mu(x)$ for all the points $x \in \Omega$ and the covariance function defines the covariance $k\ (x, x^i)$ between deformation point for x and x^i. The following derivation is adopted from Bouabene (2017).

$$\boldsymbol{u = \mu + \sum_{i=1}^{\infty} \alpha_i \sqrt{\lambda_i}\ \emptyset_i,\ \ \alpha_i\ \sim N(0, 1)} \qquad [\mathbf{2.1}]$$

where $\emptyset_i$, λ_i , $i = 1, \ldots \infty$ are eigenfunction and eigenvalue (respectively) pairs of the operator associated with the covariance function K.

For deformation fields that are defined on a discrete domain, each discretised function $\breve{u}$ can be represented as a vector $\vec{u} = (u_1, \ldots, u_n)^T$ and define a distribution over function $\breve{u}$ as (equation 2.2):

$$\boldsymbol{\vec{u} \sim N(\vec{\mu}, K)} \qquad [\mathbf{2.2}]$$

where K is a symmetric, positive semi-definite matrix and hence admits eigen decompositions (Gerig et al., 2014). Moreover, K is formulated as:

$$\boldsymbol{K = \Phi D \Phi^T} = \begin{pmatrix} \overrightarrow{\emptyset_1} & \cdots & \overrightarrow{\emptyset_n} \\ \vdots & \ddots & \vdots \\ . & \cdots & . \end{pmatrix} \begin{pmatrix} \boldsymbol{d_1} & \cdots & . \\ \vdots & \ddots & \vdots \\ . & \cdots & \boldsymbol{d_n} \end{pmatrix} \begin{pmatrix} \overrightarrow{\boldsymbol{\phi_1}} & \cdots & \overrightarrow{\boldsymbol{\phi_n}} \\ \vdots & \ddots & \vdots \\ . & \cdots & . \end{pmatrix}^{\mathbf{T}} \qquad [\mathbf{2.3}]$$

where $\overrightarrow{\emptyset_i}$ refers to the i-th column of Φ and represents the i-th eigenvector of K, and d_i is the corresponding eigenvalue. This decomposition can be computed using singular value

decomposition (SVD). Decomposing equation (2.3) using a SVD results in an expansion of the eigenpairs d_i,$\overrightarrow{\emptyset_i}$.

$$\vec{u} = \vec{\mu} + \sum_{i=1}^{n} \sqrt{d_i}\ \vec{\emptyset}_i \alpha_{i,}\ \ \alpha_i\ \sim N(0,1) \qquad [2.4]$$

Where the expected value of $\vec{u}$ is $E[\vec{u}] = \vec{\mu}$ and its covariance matrix $E[(\vec{u} - E[\vec{u}])(\vec{u} - E[\vec{u}])^T] = K$. Therefore, $\vec{u} \sim N(\vec{\mu}, K)$.

Principal component analysis is the KL expansion for a discrete representation of the data with their covariance matrix being based on example shapes. Therefore, given set of discrete deformation fields $\widetilde{u_1}$ …, $\widetilde{u_m}$ which are also representable as vectors $\overrightarrow{u_1}$,…, $\overrightarrow{u_m}$, $\overrightarrow{u_i} \in \mathbb{R}^n$, where the vector $\overrightarrow{u_i}$ represents a full deformation field and n is quite large. PCA assumes that the covariance function is estimated from a class of shapes (Williams & Rasmussen, 2006).

$$\sum = \frac{1}{m}\sum_{i=1}^{m}(\overrightarrow{u_i} - \bar{u})(\overrightarrow{u_i} - \bar{u})^T =: \frac{1}{M} XX^T \qquad [2.5]$$

where the data matrix X is defined as $X = (\overrightarrow{u_1} - \bar{u}, \ldots, \overrightarrow{u_m} - \bar{u}) \in \mathbb{R}^{n \times m}$, and $\bar{u}$ is the sample mean such that $\bar{u} = \frac{1}{m}\sum_{i=1}^{m} \overrightarrow{u_i}$.

The rank of Σ in equation (2.5) is at most m as opposed to that in equation (2.4) which is n. m is a parameter chosen to be much less than n by design. This allows for efficient computation of decomposition by performing a SVD on the smaller data matrix X. As a result, the expansion reduces to $\vec{u} = \vec{\mu} + \sum_{i=1}^{m} \sqrt{d_i}\ \overrightarrow{\emptyset_i}\ \alpha_{i,}\ \ \alpha_i\ \sim N(0,1)$. Hence, any deformation $\vec{u}$ can be completely specified by a coefficient vector $\alpha_i \in \mathbb{R}^m$.

2.6. Multi-object shape and pose modelling

A multi-object complex is a collection of adjacent anatomical objects in a common coordinate system. In a multi-object complex, the shape and pose (scale, orientation and position) of individual structures are all of importance (Cates et al., 2008). As explained in section 2.4, conventional shape analysis primarily focuses on the characterisation of single objects. However multi-object shape modelling and analysis may benefit from statistical analyses of correlations between adjacent anatomical objects rather than analysing the individual constituent structures, separately (Gorczowski et al., 2010). Thus, for multi-object shape modelling to be more useful in a medical application, the anatomical characteristic features of individual objects should be addressed simultaneously.

Multi-object SSMs have been proposed in several studies. Cootes et al. (1999) developed multi-object shape statistics by concatenating the shape features from all objects in a complex in long vectors and applying standard statistical multivariate analysis. However, the local inter-object relationships between the respective objects under consideration were not considered. Another approach to multi-object statistical shape modelling found in the literature is the medial representation (m-rep) approach introduced by Pizer et al. (1999). Medial representation has been applied in multi-object statistical analysis of deep brain structures (Gorczowski et al., 2007a, Gorczowski et al., 2010, Styner et al., 2006, Gorczowski et al., 2007b), and bladder-prostate-rectum complex in the male pelvis (Jeong et al., 2006, Pizer et al., 2005). In the m-rep paradigm, shape representation is based on medial atoms which comprise of position (p), radius (r) and a two unit-length normal vector boundary (U). The multi-object models are developed through basic linear transformations such as translation, rotation, and scaling. This is achieved by processing the individual adjacent objects from the multi-object complexes, independently. Although this approach is valid for multi-object modelling of soft tissues; in particular, for embedded tissue structures such as grey matter surrounded by white matter in the brain; it may not be suitable for objects which have a large range of pose variation. For example, it was reported that m-rep is not suitable for modelling the wrist joint (Semechko (2011). Given that most major joints in the body exhibit greater ranges of motion than the wrist joint, it can be concluded that the m-rep approach may not be ideal for such joints.

2.6.1. Multi-object registration

Various registration methods have been proposed in multi-object shape modelling for establishing anatomical correspondence. One of the more common approaches is applying rigid registration on each individual object in a multi-object complex, independently. In this approach the initial spatial relationships between all objects in the complex are inherently lost (Van De Giessen et al., 2007).

Another registration approach simultaneously registers all objects in a rigid fashion. This approach has been applied in modelling of heart ventricle (left ventricle, left ventricle myocardium, and right ventricle) (Frangi et al., 2002) and brain structures (Tsai et al., 2004). However, this approach suffers from a lack of definition of the relative position and spacing between objects. In articulations, the relative poses of different components vary during the joint motion. Thus, this registration approach is not suited for establishing correspondence in joints.

The above two registration approaches have been combined and applied on vertebrae (Roberts et al., 2005) and brain structures (Yang et al., 2004). In both studies, pose variation between adjacent objects was not considered.

In general, applying registration for multi-objects separately without considering the spatial inter-relationship is not desirable for analysing the anatomical relationship and the pose variation between objects.

2.7. Model validation methods

Once the SSMs are developed, it is common to measure the intrinsic quality of the models. Three evaluation assessments known as generality, specificity and compactness are recommended in the literature (Styner et al., 2003, Van Kaick et al., 2011).

Generality, denoted here as $G(m)$, refers to model's ability to represent unseen instances outside of the training set (Davies et al., 2010). Generalization may be estimated by conducting a leave-one out experiment using the training set. The procedure is implemented by constructing an SSM with $N-1$ training shapes and then reconstructing or fitting the excluded shape object with m principal components ($m = 0,1, \dots, N-2$). The process is repeated for all training examples. The generalization ability is then computed by using equation 2.6.

$$\boldsymbol{G(m) = \frac{1}{N}\sum_{i=1}^{N} |V_i^*(m) - V_i|^2} \qquad [\mathbf{2.6}]$$

where $V_i^*(m)$ is the best model reconstruction of V_i using m principal components. V_i is the excluded training instance.

Specificity, $S(m)$, defines ability of the model to generate shape instances similar to the training sets from which the model was constructed (Davies et al., 2010). The specificity measure is computed by generating random shapes $\{V_j\}$ from the training shape parameters and comparing them to the closest match in the training set, V_j^*. Specificity can be calculated using equation 2.7.

$$\boldsymbol{S(m) = \frac{1}{N}\sum_{i=1}^{N} |V_j(m) - V_j^*|^2} \qquad [\mathbf{2.7}]$$

where N is the number of random samples, $V_j(m)$ are randomly generated example shapes using m principal components, and V_j^* is the closest example of training dataset to V_j.

Compactness, $C(m)$, refers to the model's ability to capture most of the available shape variance with a few parameters (Davies et al., 2010). This means that a compact model uses a

sparse parametrisation to represent most of the shape variation in the training set. Compactness can be calculated using equation 2.8:

$$\boldsymbol{C(m) = \sum_{i=1}^{m} \lambda_i} \qquad [\mathbf{2.8}]$$

where λ_i is the i^{th} largest eigenvalue and $C(m)$ is the cumulative variance of m^{th} mode.

2.8. Literature summary

In summary, SSMs can be developed from a number of training examples which are in-correspondence. However, the most SSM approaches do not consider encoding pose variability between adjacent anatomical objects. This means that, the ability to explain the shape and kinematics relationship between two or more interacting objects in an anatomical complex is limited. Articulated statistical shape models are an extension of the conventional SSM which encode the relative positions of multiple objects in a complex, provided the objects share articulating surfaces.

The shoulder joint is the most mobile and unstable joint in the human body and its movement incorporates three DoFs over a large range of motion known as abduction/adduction, flexion/extension, and internal/external rotation. Articulated statistical shape models of the shoulder joint may enable the analysis of anatomical features and pose characteristics between the two articulating bones (the humeral head and the glenoid cavity). However, an ASSM of the human shoulder has not been demonstrated in the literature.

3. PROJECT OVERVIEW AND MATERIALS

This project aimed to develop an ASSM of the shoulder joint. First, 3D surface mesh data of humeri and scapulae were acquired from previous study. Next, manual anatomical landmarks were annotated on the mesh data and free form deformation models (FFDMs) of each bone were developed to facilitate the establishment of correspondence using Gaussian process morphable model (GPMM)-based non-rigid registration. The registration was performed on each humerus and scapula separately using randomly selected examples (from the training data) of each bone as references. Since this project focussed on developing a shape with pose model, the shape and kinematics relationship between the humeri and the scapulae had to be maintained. To do so, all the pairs of registered humeri and scapulae had to be brought back to their native position. This was done by applying the inverse of each of the registration transformations from the preceding step. The determination of the glenohumeral rotational center (GHRC) and local anatomic coordinate system of the humeri and scapulae was performed based on definitions suggested by the International Society of Biomechanics (ISB). Three motions (flexion, abduction, and internal rotation) were generated using an Euler angle sequence. The ASSM of the model was built using principal component analysis (PCA) and validated through the assessment as generality, specificity and compactness. Figure 3.1 shows the overview schematic following in building an ASSM of the shoulder joint.

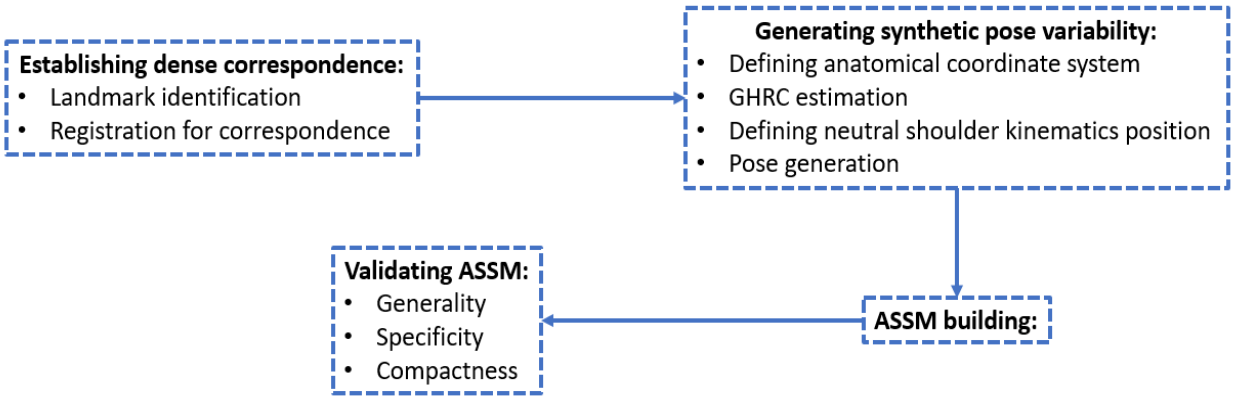

Figure 3.1. ASSM development pipeline overview

3.1. Description of the image data

Segmented 3D meshes of scapulae and humeri from computed tomographic (CT) images of eighteen South African cadaveric shoulders constituted the data used in this project. Thus, equal pairs of left and right sided-shoulders (thirty-six in total) were available for the ASSM development. Five of the cadaveric torsos obtained were from female decedents while

the remaining thirteen were from male decedents. All decedent's shoulders were deemed functional at the time of death, by a clinical scientist. The age at death varied from 29 up to 80 years (see Table 3.1). The cadaveric specimens, CT images and 3D segmentations had been obtained in a previous study under ethical clearance by the University of Cape Town's Human Research Ethics Committee (HREC: 2013/060). Ethical approval for using the images and segmentations for this project was granted by the same committee (HREC: 419/2018).

Table 3.1. Description of cadaveric shoulder data

Specimen No.	Sex of decedent	Age at time of death
1	M	43
2	M	34
3	M	60
4	M	55
5	M	33
6	M	36
7	F	78
8	F	39
9	M	35
10	M	51
11	M	51
12	M	77
13	M	50
14	M	42
15	F	56
16	M	32
17	F	42
18	F	64

3.2. Description of software tools used in project

The following software was used in the project: 1) **Amira v6.2.0** (Fei Imaging: http://www.fei.com/) software. Amira is a 3D visualization, analysis and modelling system which allows to visualize scientific datasets from various application areas. 2) Scalable Image Analysis and Shape Modelling (Scalismo) (https://scalismo.org/) software. Scalismo is an open

source library for statistical shape modelling and model-based image analysis. The software was developed by the Graphics and Vision Research Group at the University of Basel, Switzerland.

4. ESTABLISHING CORRESPONDENCE IN DATA

Statistical shape modelling requires a training shapes with well-defined correspondences. An important step in statistical shape model (SSM) building involves establishing dense correspondence between shape primitives. Establishing dense correspondence (i.e. vertex-level homology) in 3D mesh surfaces of the human anatomy is not trivial. To guide the process, some user-identified corresponding landmarks were employed. These anatomical landmarks had to be reliably identifiable across the training data. Once reliable landmarks were identified, rigid and non-rigid registration were performed to obtain dense correspondence across the 3D meshes surfaces. The landmarks were firstly used for a rigid alignment of both scapula and humerus to their respective references. Secondly, the landmarks were used as prior knowledge about correspondence in a model fitting process. Templates for each bone were developed using the iterative median closest point Gaussian mixture model (IMCP-GMM) method developed by Mutsvangwa et al. (2015). The model fitting required developing a free form deformation model (FFDM), as a Gaussian process, and using the references as templates. Each of these steps is described in detail below.

4.1 Landmark identification

Landmarks should be reproducible across the data set to achieve reliable dense correspondence. Reliability analysis helps to evaluate the uncertainty in landmark identification. To this end, a landmark reliability analysis was conducted in this project. The analysis aimed to determine which landmarks, on both the scapula and humerus, could be consistently identified by operators with high precision.

4.1.1. Landmark reliability analysis

A total of 7 and 15 anatomical landmarks were manually annotated in all 3D mesh data for humeri and scapulae, respectively. Tables 4.1 and 4.2 provide anatomical descriptions of the landmarks. Figures 4.1 and 4.2 illustrate the positions of the landmarks on each bone. These landmarks were selected because: 1) intuitively, they provide suitable anchoring points for the registration process, and 2) they provide adequate coverage of the anatomies concerned (i.e. they are no concentrated in one region). Two operators performed the annotations; twice for each operator, with more than a 24-hr interval between annotations to remove recall bias. The author and a colleague used an unpublished landmarking protocol developed in-house as guidance for learning to perform the landmarking. The reliability metric adopted for the

analysis considered the correlation between identical landmarks made on the same object per landmarking session (intra-operator reliability) and per operator (inter-operator reliability).

Table 4.1. Anatomical landmarks description of scapular bone

Landmark No.	Anatomical Landmark description
1	The most superior point of the glenoid
2	The most anterior point of the glenoid
3	The most posterior point of the glenoid
4	The most inferior point of the glenoid
5	The point at the tip point of scapular notch
6	The most tip point of superior boarder
7	The most tip point of superior angle scapular blade
8	The most superior point of medial border
9	The most inferior point of medial border
10	The most tip point of inferior angle
11	The point at the lateral boarder
12	The most peak point of acromion angle
13	The most peak point of the acromion
14	The most peak point of the coracoid process
15	The most peak point of the acromion

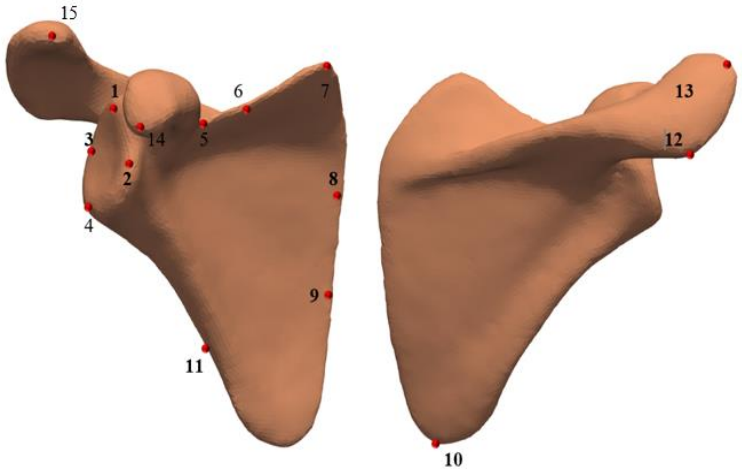

a b

Figure 4.1. Anatomical landmarks (red points) identification on a scapula: a) Anterior view, b) Posterior view

Table 4.2. Anatomical landmarks description of humeral bone

Landmark No.	Anatomical Landmark description
1	The most tip point of greater tubercle
2	The most tip point of lesser tubercle
3	The center point of coronoid fossa
4	The center point of radial fossa
5	The most tip point of medial epicondyle
6	The center point of olecranon fossa
7	The most inferior point of anatomical neck

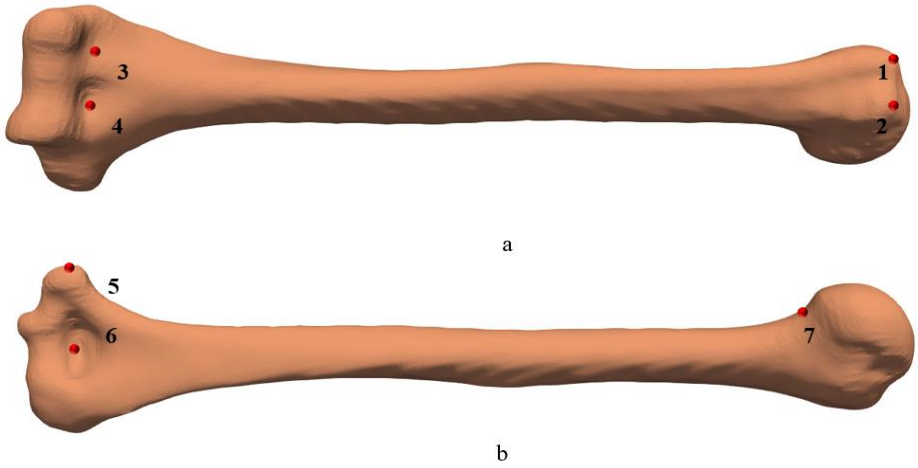

Figure 4.2. Anatomical landmarks (red points) identification on a humerus: a) Anterior view, b) Posterior view

The intra-operator and inter-operator landmarks reliability were analysed using equation 4.1 and 4.2, respectively (Mutsvangwa et al., 2011).

$$\text{Intra-operator reliability} = \frac{1}{2}\sum_{i=1}^{2}\sqrt{(x_i - x_a)^2 + (y_i - y_a)^2 + (z_i - z_a)^2} \qquad [4.1]$$

where x_i, y_i, z_i are the landmark coordinates from the first sets of both operators' annotations; similarly, x_a, y_a, z_a are the landmark coordinates from the second sets of both operators' annotations.

$$\text{Inter-operator reliability} = \frac{1}{2}\sum_{i=1}^{2}\sqrt{(x_{1i} - x_{2i})^2 + (y_{1i} - y_{2i})^2 + (z_{1i} - z_{2i})^2} \qquad [4.2]$$

where x_{1i}, y_{1i}, z_{1i} represent an average of observer 1 measurement, as well as, x_{2i}, y_{2i}, z_{2i} belongs to an average measurement of observer 2 measurements, at time i.

4.1.2. Results of landmark reliability analysis

Figures 4.3 and 4.4 show the intra-operator reliability for the humeri and scapulae, respectively. Figures 4.5 and 4.6 show the inter-operator reliability for the humeri and scapulae, respectively. The tolerance threshold distance for inter-operator reliability were based on those proposed by Mutsvangwa et al. (2011). The authors suggested that a difference of 1mm or less between the two set of measurements be considered "highly precise"; between 1mm and 1.5 mm, "moderately precise". In this study the threshold mean inter landmark error was 1.5 mm for both humeri and scapulae. Based on those results, all landmarks annotated in each mesh were at least moderately precise and thus could be considered reliable.

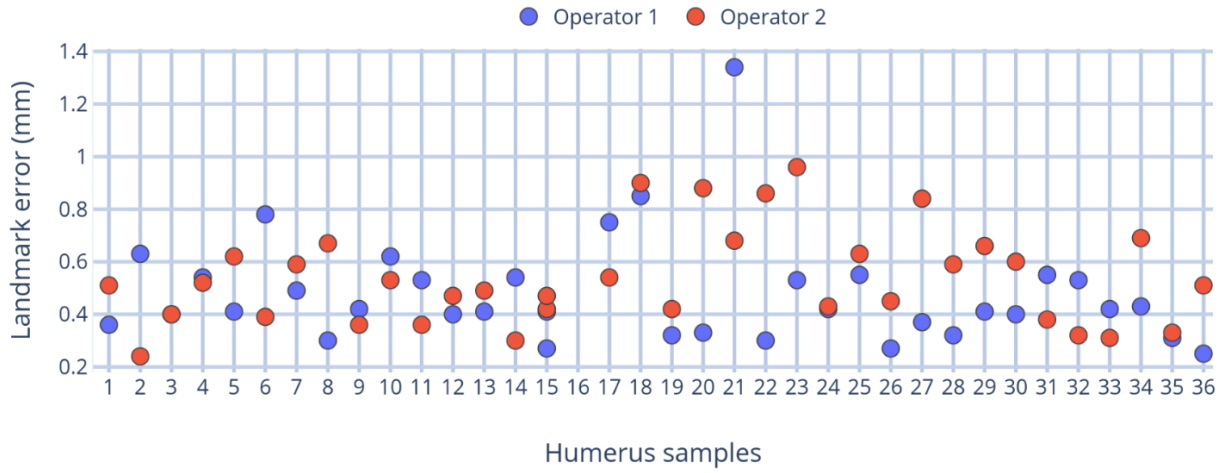

Figure 4.3. Intra-operator landmarking variability in humeri data

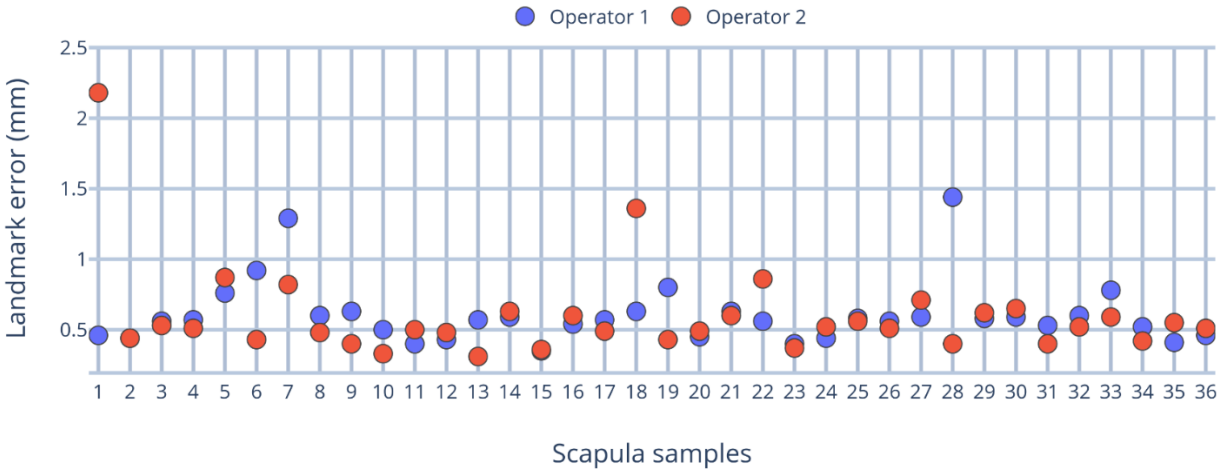

Figure 4.4. Intra-operator landmarking variability in scapulae data

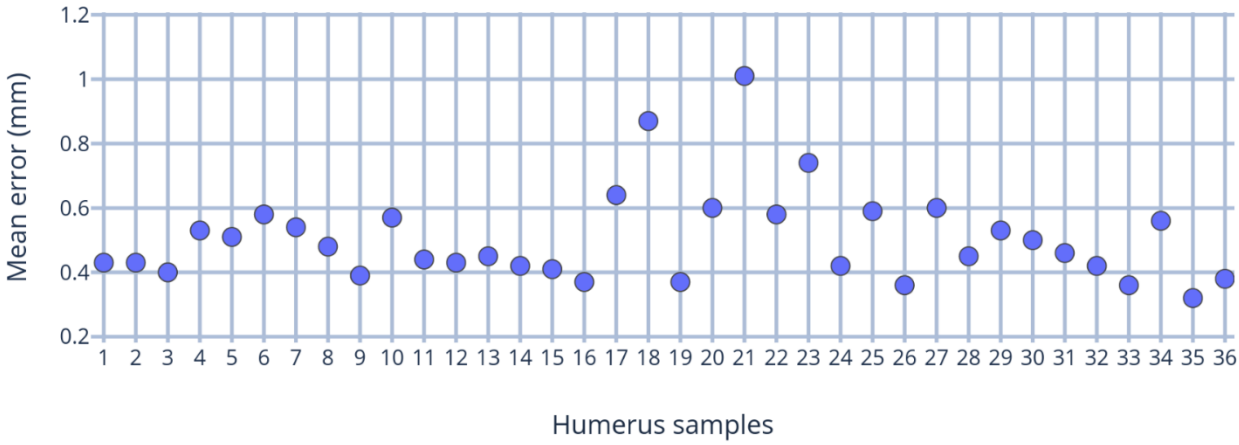

Figure 4.5. Inter-operator landmarking variability in humeri data

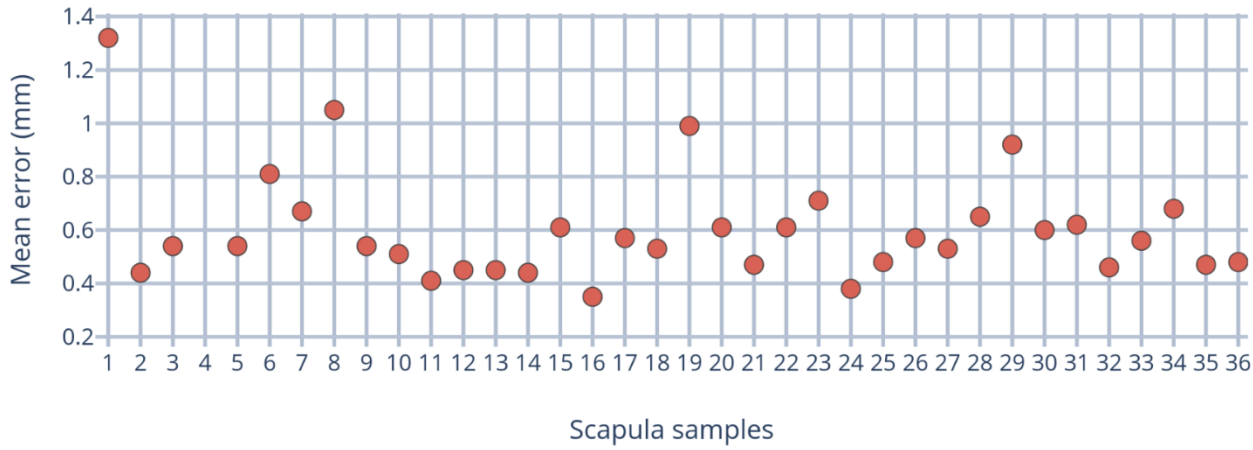

Figure 4. 6. Inter-operator landmarking variability in scapulae data

4.2. Registration for shape correspondence

Since the existing data represents the human anatomy, there existed large variation in shape and relative spatial positions of articulating structures across the data. One of the principal steps in building statistical shape models includes establishing a shape correspondence between shape boundaries over the large set of training samples. Establishing correct correspondence greatly minimizes inefficient parametrization of shape and leads to more reliable shape models. In addition to the shape correspondence, having kinematics (pose) correspondence helps to get anatomically feasible (valid) positional information between the humerus with respect to the scapula.

One way to establish dense correspondences among the 3D surface training set data is via non-rigid registration using a common reference shape example. The non-rigid registration can be performed through fitting the reference to the other shapes in the training data. This requires the reference mesh to be deformable. The GPMM framework allows for a simple way

to develop deformability of the reference mesh using the concept of a FFDM. In this process, the reference mesh acts as the domain on which the FFDM is prescribed. One issue with this approach is that the FFDM exhibits an implicit topological bias towards the reference mesh. To overcome this, an unbiased reference mesh for each bone was developed following the iterative median closest point Gaussian mixture model (IMCP-GMM) framework implemented as in-house software developed by Mutsvangwa et al. (2015).

4.2.1. Developing a FFDM

A FFDM was established over the unbiased references above (one for each bone) following the IMCP-GMM framework using internal software (Mutsvangwa et al., 2015). In the framework, the FFDM is developed over the reference which represents the new mean of the Gaussian Process. A kernel function representing how the mean shape deforms was used (equation 4.2).

$$\boldsymbol{k_g}\,(\boldsymbol{x},\boldsymbol{y}) = \boldsymbol{S}\,\mathbf{exp}(-\left|\left|\boldsymbol{x}-\boldsymbol{y}\right|\right|^{\mathbf{2}}/\,\boldsymbol{\sigma}^{\mathbf{2}}) \qquad [\mathbf{4.2}]$$

Where $\boldsymbol{S}$ and $\boldsymbol{\sigma}$ are tuneable parameters that determine the variance (i.e. scale) and the span of deformation of the features on the mean shape, respectively (Lüthi et al., 2018). Note that, any deformation sampled from *GP* gives rise to a new shape by warping the mean shape. The FFDM developed for each bone was tuned by empirically determining that best values of $\boldsymbol{\sigma}$ and $\boldsymbol{S}$ that would allow enough flexibility to deform to all target meshes. This process is outlined below.

4.2.2. Application of FFDM for registration

For the humerus, values for $\boldsymbol{s}$ and $\boldsymbol{\sigma}$ of *50mm* and *150mm* were empirically found to provide the best deformation characteristics for fitting the training data. However, given the geometric complexity of the scapula a combination of kernels was implemented. Combined kernels are a simple means of modelling deformations at multiple scales (Lüthi et al., 2018). In this project this was done by summing up multiple smooth Gaussian kernels, with decreasing scale and band width (equation 4.3).

$$k_{MS}(x,y) = \left[S_{1\,exp}\left(\frac{-(x-y)^2}{\sigma_1^2}\right)\right] + \left[S_{2\,exp}\left(\frac{-(x-y)^2}{\sigma_2^2}\right)\right] + \left[S_{3\,exp}\left(\frac{-(x-y)^2}{\sigma_3^2}\right)\right] +$$

$$\left[S_{4\,exp}\left(\frac{-(x-y)^2}{\sigma_4^2}\right)\right] + \left[S_{5\,exp}\left(\frac{-(x-y)^2}{\sigma_5^2}\right)\right] + \left[S_{6\,exp}\left(\frac{-(x-y)^2}{\sigma_6^2}\right)\right] + \left[S_{7\,exp}\left(\frac{-(x-y)^2}{\sigma_7^2}\right)\right] \qquad [4.3]$$

where $k_{MS}(x,y)$ is multiple smooth Gaussian kernel, S and σ determine the scale and smoothness, respectively, of deformation on the mean shape.

Seven different Gaussian kernels were summed up with different scales and bandwidths {k_1 *[s=200mm* and *σ=100mm]; k_2 [s=70mm* and *σ=5mm]; k_3 [s=50mm* and *σ=10mm]; k_4 [s=5mm* and *σ=5mm]; k_5 [s=0.5mm* and *σ=5mm*] to achieve the best fitting of scapulae data.

4.3. Establishing shape and kinematics correspondence

Once the FFDMs were developed, dense correspondence was established between the FFDMs of each bone and their respective targets using Gaussian process model fitting (Lüthi et al., 2018). In this process, rigid alignment was first performed using the landmarks in section 4.1 and the iterative closest point (ICP) algorithm. The ICP algorithm allows for the transformation of landmarks of the FFDM to the corresponding landmarks on each of the target shapes (see figure 4.3). Next, the actual correspondence between the set of landmarks is used as prior information to obtain a posterior model. A posterior model refers to an instance of the FFDM that closely resembles an individual target (see figure 4.4).

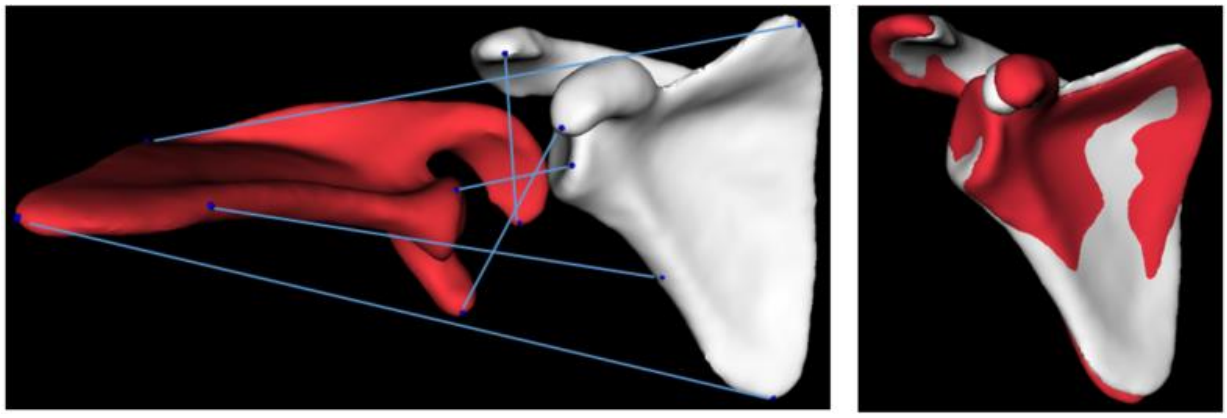

a b

Figure 4.7. Protocol to achieve rigid alignment illustrated using a sample target scapula (red) and an FFDM (grey): a) before rigid alignment, b) after rigid alignment. The blue points represent a subset of the anatomical landmarks used and the light blue lines indicate which points are corresponding points

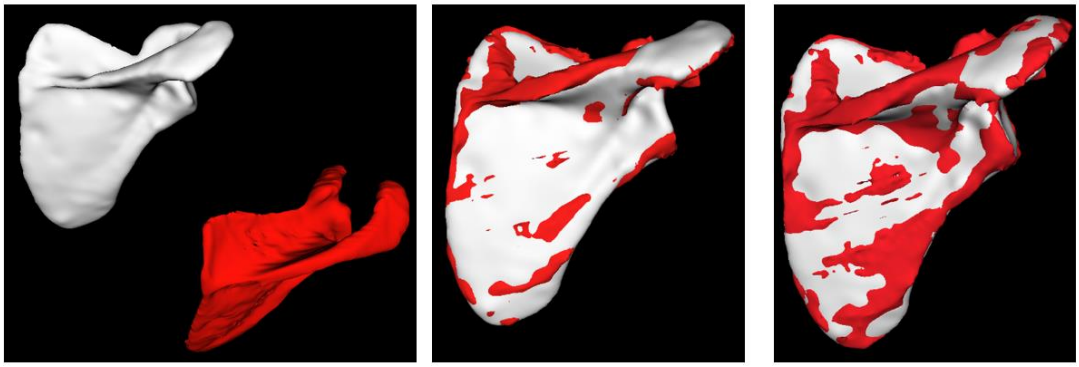

a b c

Figure 4.8. Non-rigid registration protocol: a) initial registration b) during registration the FFDM (grey) deforms and fit to the target (red), b) end of registration: the FFDM (grey) closely represents the target (red)

The joint kinematics describe the geometrical motion in objects and systems of objects. If shape registration for establishing correspondence between two objects in a complex is performed separately, the relative position between the two objects would not be preserved. In order to register two objects while keeping their shape and kinematics relationship, the method proposed by Fouefack et al. (2019) was adopted. The method assumes that one of the two objects is fixed and the other is allowed to move. Anatomically, the fixed and the moving objects are defined as the proximal body and the distal body, respectively. As the scapula is more proximal than the humerus, and positioned closer to the anatomical middle line, the humerus was described as the moving object. After the shape registration step above was complete, each moving segment (humerus) mesh was brought back to its original position using an inverse transform to the registration transformation above. Equation 4.4 succinctly describes how the shape and kinematics established (Fouefack et al., 2019):

$$\begin{pmatrix} \boldsymbol{O_f} \\ \boldsymbol{O_m} \end{pmatrix}_{\boldsymbol{r}} = \begin{pmatrix} \boldsymbol{T_f}(\boldsymbol{O_f}) \\ \boldsymbol{T_f}\left(\boldsymbol{T_f^{-1}}\,(\boldsymbol{O_m}) \circ \boldsymbol{T_m}\,(\boldsymbol{O_m^r})\right) \end{pmatrix} \qquad [\mathbf{4.4}]$$

Where *f, m and r* represent abbreviations for fixed, moving and registered objects, respectively. $\begin{pmatrix} O_f \\ O_m \end{pmatrix}$ represents the target objects; T_f defines the registration transformation for the fixed object (O_f); and T_m defines the registration transformation (O_m) for the moving object.

4.3.1. Results

As the shape and kinematics correspondence need to be defined based on GPMM, the shape and kinematics of the humerus related to the scapula was well defined. Each registered humerus was brought back to its original position, as shown in figure 4.5 and 4.6.

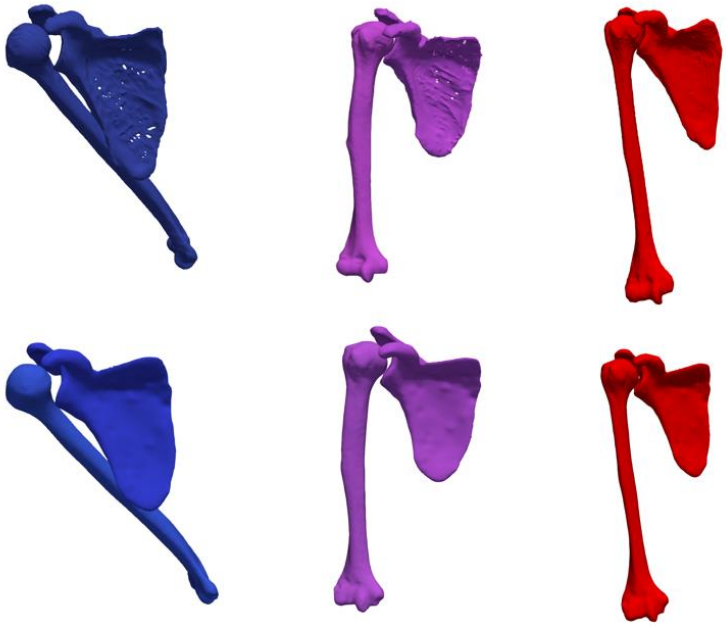

Figure 4.9. Examples of training data specimens (3 out of the total 36 specimens) used to build statistical shape and kinematics model. The top row shows the target data at random pose; the bottom row shows target meshes obtained using registration

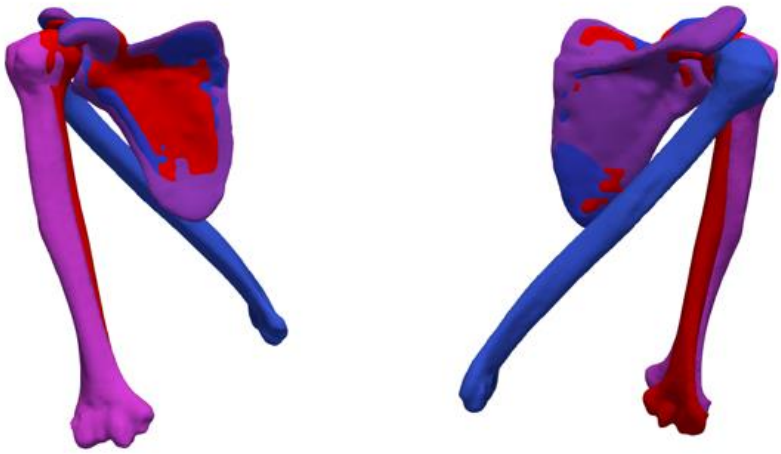

a b

Figure 4.10. Each registered humerus mesh brought back to its original position: a) anterior view, b) posterior view

4.3.2. Assessing registration error

The registration errors for humeri and scapulae data are shown in figure 4.11. The errors were calculated by measuring the surface-to-surface distances between each original mesh and its approximation (or "fit") after registration via model fitting. Hausdorff distance was used as the distance metric. It determines that how close points in one mesh are to the corresponding points in the other mesh. Small registration errors signal that the approximation is sufficiently close to the original mesh in morphological terms. This is desired as the approximations are used in developing the model, because they are in dense correspondence with the reference. The result shows that the Hausdorff distances for the humeri bones ranged between 1.0 mm and 2.30 mm. For the scapulae bones, the Hausdorff distance ranged between 1.31mm and 2.50 mm. The average Hausdorff distances for humeri and scapulae were 1.15 mm and 1.79 mm, respectively with standard deviations of 0.22 mm and 0.27 mm, respectively.

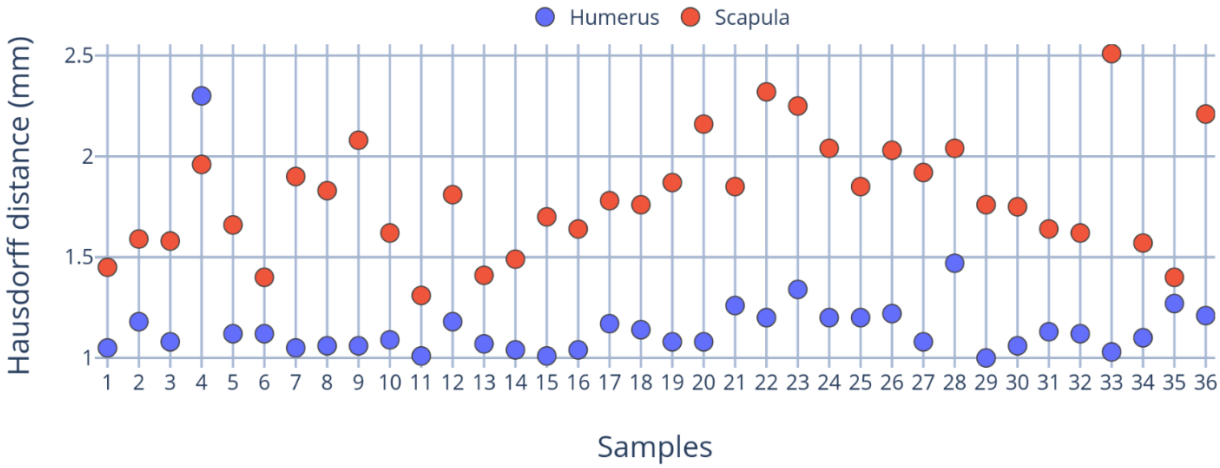

Figure 4. 11. Landmark registration error for individual humeri and scapulae

The errors on both meshes indicated that there were human errors due to landmarking process. In addition, there had been shown higher registration error in scapular mesh than the humeri. This may be attributed to scapulae being morphologically more complex than humeri (Mutsvangwa et al., 2015)

The shape and kinematic correspondence were suited for building the ASSM. In shape and kinematics correspondence definition, in addition to the shape registration the positional correlation between the two bones in the shoulder (humerus and scapula) were defined.

4.4. Chapter summary

A framework for establishing proper shape correspondence was developed. The framework included a reliability analysis for the landmarking. These landmarks were suitable candidate points for sparse feature shape model fitting. High level of landmark precision with mean error was found in scapula than the humerus. This landmark reliability helps to generate a proper dense correspondence across the dataset during registration.

In the development of the FFDMs, a square exponential and a multiple smooth Gaussian kernel were used as the model's kernel for the humerus and scapula, respectively so that the span (σ) and degree (s) of deformation values for the kernel were determined empirically. The degree of deformability of each bone FFDM was determined using visual inspection and determined to be sufficiently flexible for fitting to target data.

Finally, a pipeline for establishing shape and kinematics correspondence was developed. A visual inspection of the registered objects revealed that the post-fitting deformed FFDM geometries were morphologically representative of the original targets. This was confirmed by a numerical analysis of registration errors. The results showed less registration errors in humeri compare to scapulae; and globally all were low enough to justify the use of the deformed FFDM geometries in lieu of the original targets for the modelling.

5. GENERATING SYNTHETIC POSE VARIABILITY

The range of motion of the shoulder joint varies greatly between individuals. In order to define synthetic shoulder kinematics, the anatomic coordinate system of the humerus and the scapula had to be defined. Additionally, because the cadaveric shoulder images were acquired with random positioning of the humerus with respect to the scapula, the humeri in all the training data had to be virtually repositioned to a resting (0^0) position, relative to the scapulae. An estimation of the glenohumeral rotation centre (GHRC) had to be obtained on the humeral head in order to be able to generate different motion.

This chapter describes how each of these steps was carried out in order to generate realistic abduction, flexion, and internal rotation motion.

5.1. Definition of glenohumeral rotational center (GHRC)

Measurement of joint kinematics is important in biomechanics, motion synthesis and analysis (Gamage and Lasenby, 2002). Being a ball and socket joint, the shoulder joint's rotation is approximated on an arbitrarily oriented axis through a fixed center. The humeral coordinate system origin can be considered to be positioned at the GHRC (see figure 2.4). However, in-accurate location of the GHRC may have significant effect on the calculation of kinetics and kinematics of the shoulder. This means that it is critical to accurately determine the GHRC.

5.1.1. Method developed for establishing GHRC

The sphere fitting algorithm (Rachakonda et al., 2017) for calculating GHRC was implemented in Scalismo. The sphere fitting algorithm relies on a least square minimization method in order to obtain the GHRC. The process involves fitting a sphere to the articular surface of the humeral head such that the center of the sphere corresponds to the GHRC (see Figure 5.1). The GHRC is then calculated using equation 5.1.

$$\mathbf{J} = \sum_{i=1}^{n} \sqrt{(x_i - GHRC)^2 + (y_i - GHRC)^2 + (z_i - GHRC)^2} - R \qquad [5.1]$$

Where: x_i, y_i, and z_i are the three points generated on the sphere, $GHRC$ is the GH center of rotation, n is the number of the humeral head surface points, and R is the radius of the fitted sphere.

Figure 5.1. GHRC calculation using the sphere fitting method (fitted sphere is grey). The centre of the sphere (blue point) represent the GHRC

5.1.2. Validation of GHRC

It was very necessary to evaluate the reliability of the sphere fitting algorithm using a 3D mesh sphere, with ground truth radius and centre determined in SolidWorks (Dassault Systèmes, Vélizy-Villacoublay, France). SolidWorks is a fully validated, commercially available modelling software. The same sphere was imported into Scalismo as a stereolithography (STL) and the sphere fitting algorithm was used to calculate its radius. The radius of the sphere obtained from Scalismo and SolidWorks were 23.416mm (figure 5.2a) and 23.421mm (figure 5.2b), respectively. The relative error between the two results was 0.005mm**.** Therefore, it was concluded that GHRC values computed using the adopted sphere fitting algorithm would be reliable.

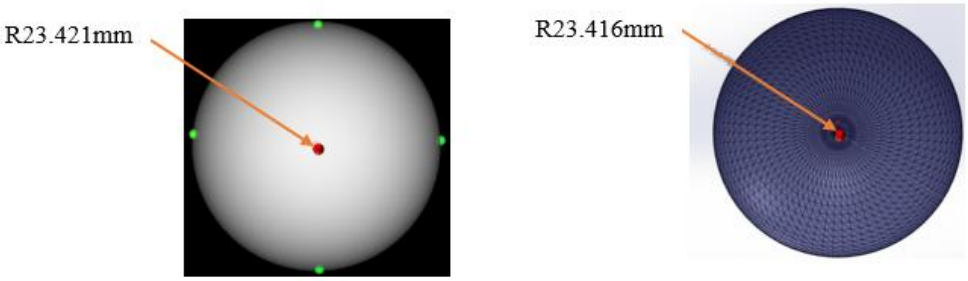

a b

Figure 5.2. Sphere mesh radius measurement and center identification: a) In Scalismo b) In Solidworks. The green individual points in "a" were used to determine the surface of sphere; the red points represent the centres of the spheres

The humeral head radius in the training data ranged between 18.8mm and 28.35mm. The mean and the standard deviations were 22.71mm, and 2.11mm, respectively. Similarly, the

mean and standard deviation of GHRC in x-, *y*-, *z*-, coordinates were [55.45, -192.22, -18.54] mm and [3.92, 2.5, 3.32] mm, respectively. The variability of the radius and GHRC could be directly attributed to the anatomical variability of the humeral heads in the training data.

5.2. Defining anatomic coordinate system

When the cadaveric shoulders were scanned in CT, their reference frame coordinate systems were not identical to their individual anatomic coordinate systems. Hence, all the 3D mesh data (in-correspondence but in their native imaging positions) had to be translated to their individual anatomic coordinate systems. The scapular and humeral anatomic coordinate systems were developed based on definitions suggested by the International Society of Biomechanics (ISB) (Wu et al., 2005). The standard shoulder anatomic coordinate system recommended by ISB is based on a set of scapular and humeral anatomical bony landmarks (see Table 5.1). These landmarks are used to define the three rotations required to transform the humerus coordinate system with respect to the scapula coordinate system (Levasseur et al., 2007). The error in identifying the anatomical landmarks had to be minimized as imprecise localization would lead to an anomalous coordinate system that would ultimately affect the developed kinematics motion (Marin et al., 2003). An assessment of the reliability of the landmarks is presented below.

5.2.1. Assessing the reliability of landmarks

Bony landmarks (see Table 5.1) on the humeri and scapulae were identified on each 3D mesh.

Table 5.1. Description of the bony landmarks in humerus and scapula used to determine anatomic coordinate system

bone	anatomical landmark	description
scapula	AA	Angulus acromialis, the most latero-dorsal point of the scapula.
	TS	Trigonum spinae, midpoint of triangular surface on medial border of the scapula in line with the scapular spine.
	IA	Interior Angulus, the most caudal point of the scapula.
humerus	GH	Glenohumeral center of rotation.
	LE	The most caudal point on lateral epicondyle.
	ME	The most caudal point on medial epicondyle.

Since all meshes were in correspondence, only one operator performed the landmarking; twice with more than a 24-hr interval between annotations. The results of the landmark reliability are shown in tables 5.2 and 5.3.

Table 5.2. Local coordinate system intra-operator landmarking error in humeri data

	humerus			
	mean error (mm)	standard deviation (mm)	minimum (mm)	maximum (mm)
Intra-operator	0.14	0.11	0.15	0.17

Table 5.3. Local coordinate system intra-operator landmarking error in scapulae data

	scapula			
	mean error (mm)	standard deviation (mm)	minimum (mm)	maximum (mm)
Intra-operator	0.30	0.10	0.17	0.39

The average local coordinate system intra-operator landmarking error obtained for both humeri and scapulae was less than 1.5mm which satisfies the "moderately precise" threshold suggested by Mutsvangwa et al. (2011).

5.2.2. Determining anatomical coordinate systems

The scapular and humeral coordinate systems (figure 5.3) were defined for each humerus and scapula. The process generated the required axes using the landmarks established above.

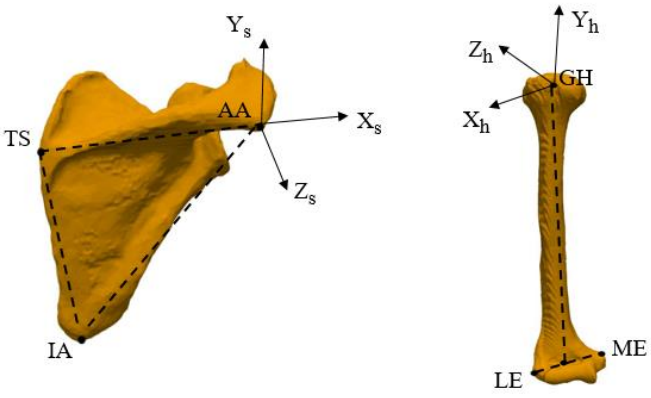

a b

Figure 5.3. Anatomical coordinate system based on ISB standards: a) scapula, b) humerus

Equations 5.2 and 5.3, describe how the anatomical axes for the humerus and scapula, respectively, were defined.

$$\mathbf{Y_h} = \frac{\overline{\mathbf{GH}} - \frac{\overline{\mathbf{ME}} + \overline{\mathbf{LE}}}{\mathbf{2}}}{\left|\overline{\mathbf{GH}} - \frac{\overline{\mathbf{ME}} + \overline{\mathbf{LE}}}{\mathbf{2}}\right|}, \qquad \mathbf{Z_h} = \mathbf{Y_h} \times \frac{\overline{\mathbf{ME}} - \overline{\mathbf{LE}}}{|\overline{\mathbf{ME}} - \overline{\mathbf{LE}}|}, \qquad \mathbf{X_h} = \mathbf{Y_h} \times \mathbf{Z_h} \qquad [\mathbf{5.2}]$$

$$\mathbf{X_s} = \frac{\overline{\mathbf{AA}} - \overline{\mathbf{TS}}}{|\overline{\mathbf{AA}} - \overline{\mathbf{TS}}|}, \qquad \mathbf{Z_s} = \mathbf{X_s} \times \frac{\overline{\mathbf{AA}} - \overline{\mathbf{IA}}}{|\overline{\mathbf{AA}} - \overline{\mathbf{IA}}|}, \qquad \mathbf{Y_s} = \mathbf{Z_s} \times \mathbf{X_s} \qquad [\mathbf{5.3}]$$

where the humerus coordinate system origin was located at GH and defined by three unit basis vectors of $X_{h,}$ $Y_{h,}$ and Z_h. The unit vector Y_h lay along the long axis of the humerus that connects the GH and the midpoint of LE and ME; the Z_h vector axis lay perpendicular to the plane formed by LE, ME and GH. The X_h vector axis was then a common line perpendicular to Y_h and Z_h. The scapular coordinate system origin was positioned at AA and its axis defined by three-unit basis vectors of $X_{s,}$ Y_s and Z_s. The Z_s vector axis was defined by a line connecting TS and AA; the X_s axis was a line perpendicular to the plane formed by IA, AA and TS. The Y_s axis was then defined by a common line perpendicular to X_s and Z_s. This entire process was developed and performed in Scalismo. Figure 5.4 shows the transformation of the original data coordinate system as defined in the CT images and the anatomical coordinate system defined after the above process.

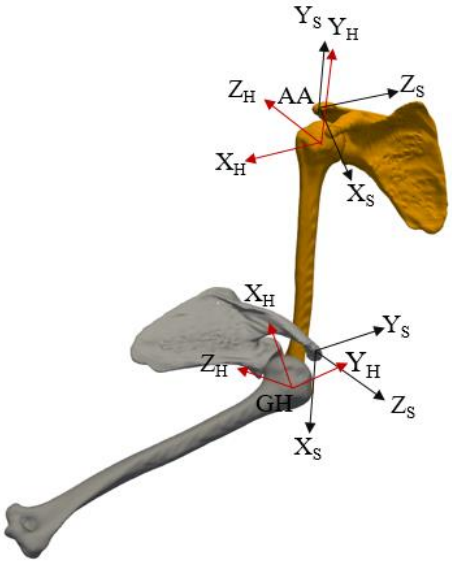

Figure 5.4. Transformation of the original (CT) data coordinate system into the anatomical coordinate system orientation, the grey and yellow coloured mesh indicates the original data and local anatomic coordinate system, respectively

5.3. Establishing shoulder resting (intrinsic) position

In order to generate meaningful motion it was required that the humerus for each shoulder be brought to 0^0 with respect to its scapula. This position is known as the shoulder resting position (Levasseur et al., 2007).

To obtain the resting shoulder position, the axis of the rotating (humeral) and the reference (scapular) coordinate frames were initially aligned to each other based on the orientation of the coordinate system (figure 5.5b). After the alignment, the origin of the scapula coordinate system was positioned at GH instead of AA, making the axis of the humerus coordinate system parallel and coincident to the axis of scapular coordinate system (figure 4.6c) (Levasseur et al., 2007). Each of the shoulder training samples were translated from their existing poses to their resting positions in Scalismo.

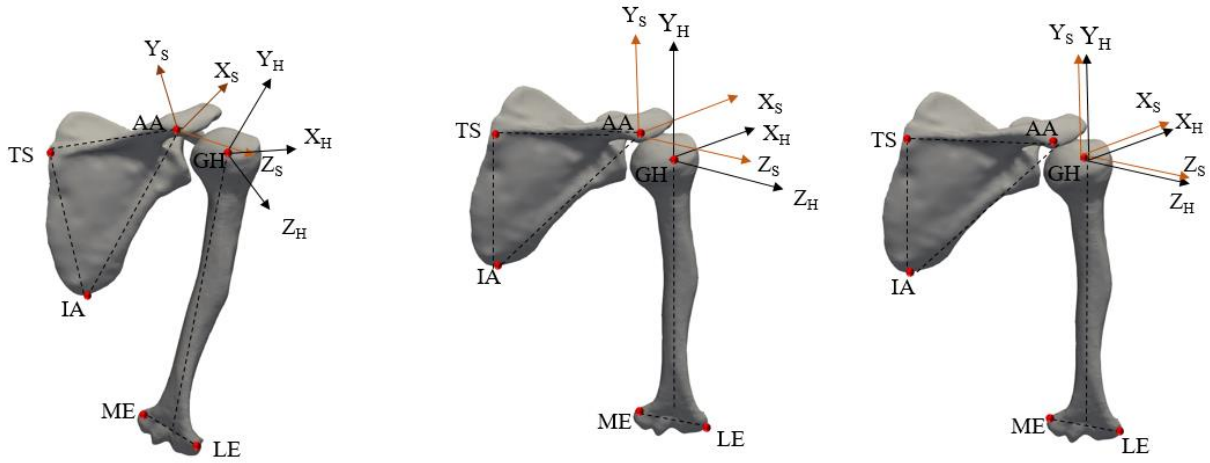

Figure 5.5. JCS definintion: a) original pose, b) resting position, c) alignment of scapula origin coordinates with humerus origin

5.4. Defining specific motions

An understanding of GH motion in normal and pathological conditions requires accurate measurement of shoulder joint kinematics (Giphart et al., 2013). Given that this project focussed on building an ASSM of the shoulder, the synthetic GH joint motion was required to realistically mimic shoulder joint kinematics. The three standard shoulder motions (abduction, flexion, and internal rotation) were simulated for different angle ranges. The rationale here was that the three motions prescribed using data of different shapes would allow for an insight into interaction between shapes and pose.

It is known that the shoulder joint has three rotational degrees of freedom (DoF); hence, its range of motion (ROM) can be defined using Euler axis sequences. Euler angles describe three successive sequences of rotation which quantifying the angular position of the rigid frame (scapula in this case) with respect to the reference frame (humerus) (Sinclair et al., 2012). When using Euler angle computations, the angle of rotation is dependent on the decomposition sequence used; the optimal sequence depends on the type of motion (Karduna et al., 1996). The standard GH joint rotation is computed using Euler *YXY* ($Y_s - X_f' - Y_h''$) sequence (Wu et al., 2005). The *YXY* sequence rotation is first about the scapular *y*-axis, followed by a rotation about the humeral *x*-axis, and finally, rotation of the humeral *y*-axis. However, this sequence can create gimbal lock (Šenk and Chèze, 2006, Bonnefoy-Mazure et al., 2010). A gimbal lock occurs when, for a sequence of rotations defined about the three axes, two or more axes become coincident and a 3-DoF cannot be represented (Hill et al., 2008, Rundquist and Ludewig, 2004).

To avoid gimbal lock, the Euler *XZY* sequence was used to orientate the humerus relative to the scapula (figure 5.6). The *XZY* rotation sequence is not vulnerable to gimbal lock (Šenk and Chèze, 2006, Bonnefoy-Mazure et al., 2010, Phadke et al., 2011). In the *XZY* ($X_s - Z_f' - Y_h''$) sequence, the first rotation (X_s) defines GH abduction/adduction in XZ plane, the second rotation (Z_f') describes flexion/extension performed in YZ plane, and the third rotation (Y_h'') quantifies the internal/external rotation along the humeral shaft axis. For Euler *XZY* sequence, the rotation matrices, which represent rotations about x, y, z axes, were multiplied in order to obtain *XZY* 3D rotation matrix as shown in equation 5.4. The angle of rotation about each of the three axes was then computed from the appropriate elements in the matrix using equation 5.5.

$$\boldsymbol{R_x R_{z'} R_{y''}} = \begin{bmatrix} \boldsymbol{C_{z'} C_{y''}} & \boldsymbol{-S_{z'}} & \boldsymbol{C_{z'} S_{y''}} \\ \boldsymbol{S_x S_{y''} + C_x C_{y''} C_{z''}} & \boldsymbol{C_x C_{z'}} & \boldsymbol{C_x S_{z'} S_{y''} - C_{y'} S_x} \\ \boldsymbol{C_{y''} S_x S_{z'} - C_x S_{y''}} & \boldsymbol{C_{z'} S_x} & \boldsymbol{C_x C_{y''} + S_x S_{z'} S_{y''}} \end{bmatrix} \qquad [\mathbf{5.4}]$$

Where $C_x = cos\ \emptyset \quad C_{z'} = cos\ \theta$, $C_{y''} = cos\ \lambda$, $S_x = sin\ \emptyset \quad S_{z'} = sin\ \theta$, $S_{y''} = sin\ \lambda$

$$\begin{aligned} \boldsymbol{\theta_x} &= \boldsymbol{tan^{-1}}\left(\frac{\boldsymbol{cos\ \theta sin\ \emptyset}}{\boldsymbol{cos\ \emptyset cos\ \theta}}\right), \\ \boldsymbol{\theta_{z'}} &= \boldsymbol{sin^{-1}}(\boldsymbol{-sin\ \emptyset\ sin\ \lambda - cos\ \emptyset cos\ \lambda cos\ \theta}), \\ \boldsymbol{\theta_{y''}} &= \boldsymbol{tan^{-1}}\left(\frac{\boldsymbol{cos\ \lambda\ sin\ \emptyset sin\ \theta - cos\ \emptyset\ sin\ \lambda}}{\boldsymbol{cos\ \theta cos\ \lambda}}\right) \end{aligned} \qquad [\mathbf{5.5}]$$

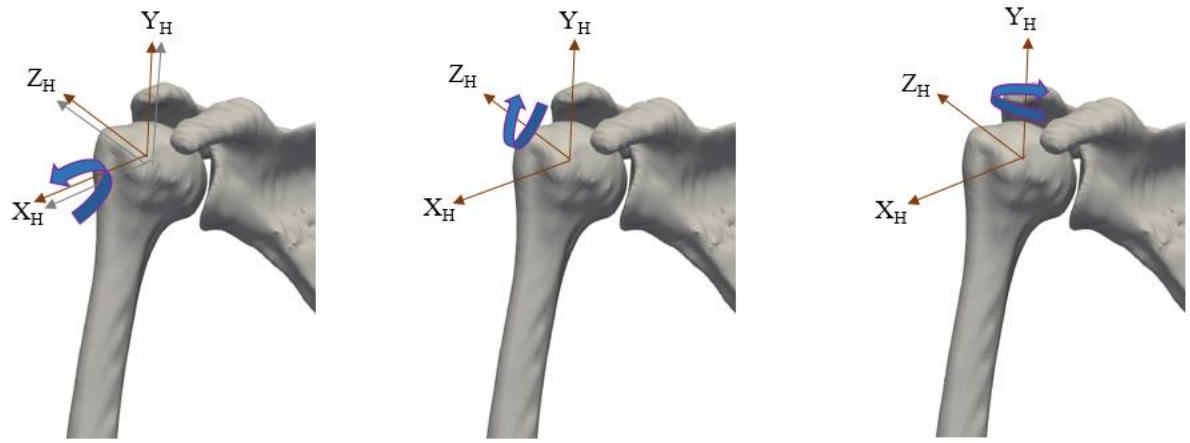

Figure 5. 6. Shoulder joint motion depicted along three axes using the XZY sequence

5.4.1. Results of defining specific motion

Simulated motions (abduction in *XZ* plane, flexion in *YZ* plane, and internal rotation in *XY* plane) were generated in Scalismo. Figure 5.7 shows the three specific motions of an example shoulder.

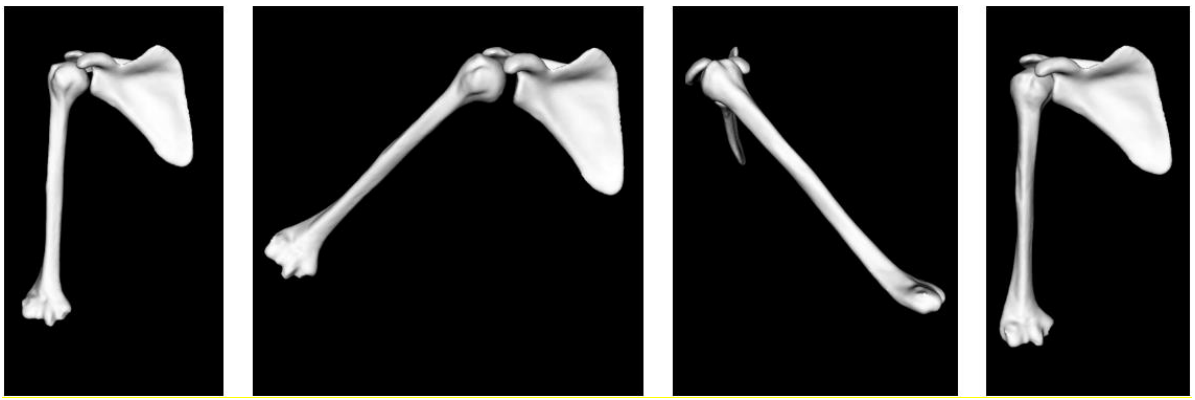

a b c d

Figure 5.7. Synthetic motion generation: a) Resting position; b), c), and d) show 40^0 abduction, flexion, and internal rotation, respectively

6. DEVELOPMENT OF ASSM OF THE SHOULDER JOINT

As outlined in the literature review, articulated statistical shape models (ASSMs) extend conventional SSMs by combining the variation in shape with variation in articulation pose. The relative pose of constituent objects in joint motion are restricted by the joint's degrees of freedom (DoF). Statistical analysis of shape and pose can be computed via principal component analysis (PCA) which provides a parametrization and succinct representation of shape and pose variability. After the ASSM is developed, it is important to test the intrinsic quality of the model using the well-established metrics of compactness, generality, and specificity. This chapter describes a protocol for building and validating the ASSM of the shoulder joint using the data from the preceding chapters.

6.1. Building ASSM of the shoulder joint

The shape and pose model can be developed by extracting the mean shape and several modes of variation (using PCA) from a collection of aligned training samples in-correspondence. Before the PCA can be performed, all the in-correspondence data need to be aligned into a common coordinate frame. The alignment is normally performed using generalized Procrustes analysis (GPA).

6.1.1. Method adopted for ASSM

In order to build the ASSM, a statistical shape and kinematics (pose) models (SSKMs) building approach by (Jean-Rassaire et al., 2019) was adopted. The approach generalizes joint parametrization to any range of motion and models the shape-pose relationship as a Gaussian process model (GPM). In this project, each joint was represented as concatenated vectors of shape parameters (the moving object vertices) of fixed object meshes and pose parameters. Using the known groupings (shape and pose) of the concatenated data set, the group mean and empirical kernel functions of the Gaussian process (GP) were defined. The following derivation is from Fouefack et al. (2019). Assume there are *n* samples in the training data, denoted as:

$$\boldsymbol{X_1} = \left[\boldsymbol{X^1_{shape}}, \boldsymbol{X^1_{pose}}\right]^{\boldsymbol{T}} \ldots \boldsymbol{X_n} = \left[\boldsymbol{X^n_{shape}}, \boldsymbol{X^n_{pose}}\right]^{\boldsymbol{T}} \qquad [\mathbf{6.1}]$$

Where X^i_{shape} and X^i_{pose} represent the point domain of shape and pose, respectively. Then a set of deformation fields $\mathcal{U}_i = i = 1. \ . \ .n$ associated to the densely corresponding objects $X_i = i = 1. \ . \ .n$. Each deformation field is a transformation that maps a point x on the

reference sample (or reference domain) to its corresponding target point $\mathcal{U}_i(x)$. The deformation fields can be modelled by a GP as shown equation 6.2:

$$\boldsymbol{GP(\mu_{ASSM}, k_{ASSM})} \qquad [\mathbf{6.2}]$$

where $\mu_{ASSM}\ (x) = \begin{pmatrix} \mu_{shape}(x) \\ \mu_{pose}(x) \end{pmatrix} = \frac{1}{n}\sum_{i=1}^{n} \mathcal{U}_i(x)$ which define the mean of deformation fields $\mathcal{U}_i$; $k_{ASSM}(x, x') = \frac{1}{n-1}\sum_{i=1}^{n}(\mathcal{U}_i(x) - \mu_{ASSM}(x))\left(\mathcal{U}_i(x') - \mu_{ASSM}(x')\right)^T$ define the covariance functions defined from the mean deformation fields (Smoger et al., 2015). The ASSM can then be generated as deformation field computed using equation 6.3:

$$\boldsymbol{ASSM = \mu_{ASSM} + \sum_{i=1}^{n} \alpha_i \sqrt{\lambda_i}\phi_i} \qquad [\mathbf{6.3}]$$

where $\alpha_i \sim \mathcal{N}(0, 1)$, and $(\lambda_i, \phi_i)_{i=1\ldots n}(x)$ is the coupled eigenvalues/eigenvectors of the sample covariance kernel. $\phi_i(x)$ is defined as concatenated vectors of shape and pose eigenvectors as shown in equation 6.4.

$$\boldsymbol{\phi_i(x) = \left(\emptyset^i_{shape}(x), \emptyset^i_{pose}(x)\right)} \qquad [\mathbf{6.4}]$$

A model sample $\begin{pmatrix} X_{new}(x) \\ X_{position}(x) \end{pmatrix}$ can the obtained as:

$$\left\{\begin{pmatrix} \boldsymbol{\mu_{shape}(x)} \\ \boldsymbol{\mu_{pose}(x)} \end{pmatrix} + \sum_{i=1}^{n} \sqrt{\lambda_i} \begin{pmatrix} \boldsymbol{\phi^i_{shape}(x)} \\ \boldsymbol{\phi^i_{pose}\,(x)} \end{pmatrix}\right\} \qquad [\mathbf{6.5}]$$

where $x \in D$ with D the reference joints point domain. A new sample is transformed rigidly to its spatial position using spatial parameters.

No dynamic data of the same object at different poses was available for developing an ASSM to investigate the real biological correlation between shape and pose. However, a method for artificially defining the shape and pose relationship using the GPM was developed. This is presented in the following sections.

6.1.2. Method adopted for the development of ASSM of the shoulder joint for the three motion

Twenty-six shoulders data (72% of the original data set) were categorised as training data and the rest, (28%) as test data. The training data were used for the ASSM building; the test data were used for model validation as described in section (6.2.1) below. The original data

set were divided into three classes with respect to each of the motions: abduction, flexion, and internal rotation. Each data pair was assigned a number 1-36, (see table 6.1).

Table 6.1. The different dataset compositions for the generation of the three motions

group sample	test data	training data	motion
one	[1-10]	[11-36]	Abduction
two	[11-20]	[1-10] + [21-36]	Flexion
three	[21-30]	[1-20] + [31-36]	Internal rotation

For abduction motion, data samples [1-10] were used as test data and the rest samples [11-36] were training data. For flexion, samples [11-20] were selected as test data and the rest of the data [1-10] and [21-30] combined as training data. Finally, for internal rotation, the data samples [21-30] and the combination of [1-20] and [31-36] were selected as test and training data, respectively. The rationale for this grouping was to avoid the same samples being used in model building of each motion i.e., there should not be correlation between shape and pose in the existing samples. For each motion, test data were generated from 0^0 to 36^0 in 4^0 motion range, while the training data motion ranged from 0^0 to 50^0 in 2^0 intervals using the XZY sequence. Models for each motion were developed based on the training data ranges in Table 6.1.

6.1.3. Results of ASSM

To visualise the dominant modes of variation encoded in the ASSM for each motion type, the mean shape complex (humerus and scapula) was warped along the directions of the first three principal components (PCs). Figures 6.1 up to 6.8 illustrate the shape and pose variation of the abduction, flexion, and internal rotation ASSM starting at two different reference angles (16^0 and 30^0). The reason for depicting the variation at these two angles is to visualize the characteristics of the shape and pose variability. Figure 6.1 illustrates the shape variation of the abduction ASSM at 16^0. The convex curvature of the scapula's lateral border increases while the superior border becomes less curved, as the mean is warped from a standard deviation (STD) of -3 to +3 along that first PC. For the second PC, the superior border changes from curved to slightly flat; the lateral border becomes wider and the scapular notch becomes both less narrow and less deep from -3 STD to +3 STD. For the third PC, the lateral border

becomes less curved. In all PCs the humeral head does not impinge on the acromion for the entire STD bandwidth.

Similarly, figure 6.2 depicts the shape and pose variation of the abduction ASSM at 30^0. From -3STD to +3STD along the first PC, the superior border becomes less curved, while the scapular notch is narrower and less deep. In addition, significant size variation of the humerus is evident. The humeral head moves away from the glenoid from -3STD to +3STD along the first PC. For the second PC, the lateral border become less curved, the superior border's convex curvature increases, and there is an increase in depth of the scapula notch. There is no significant humeral shape variation for the third PC; the only shape variation observable is a decrease in the curvature of the lateral border; some impingement is observed from -3STD to +3STD.

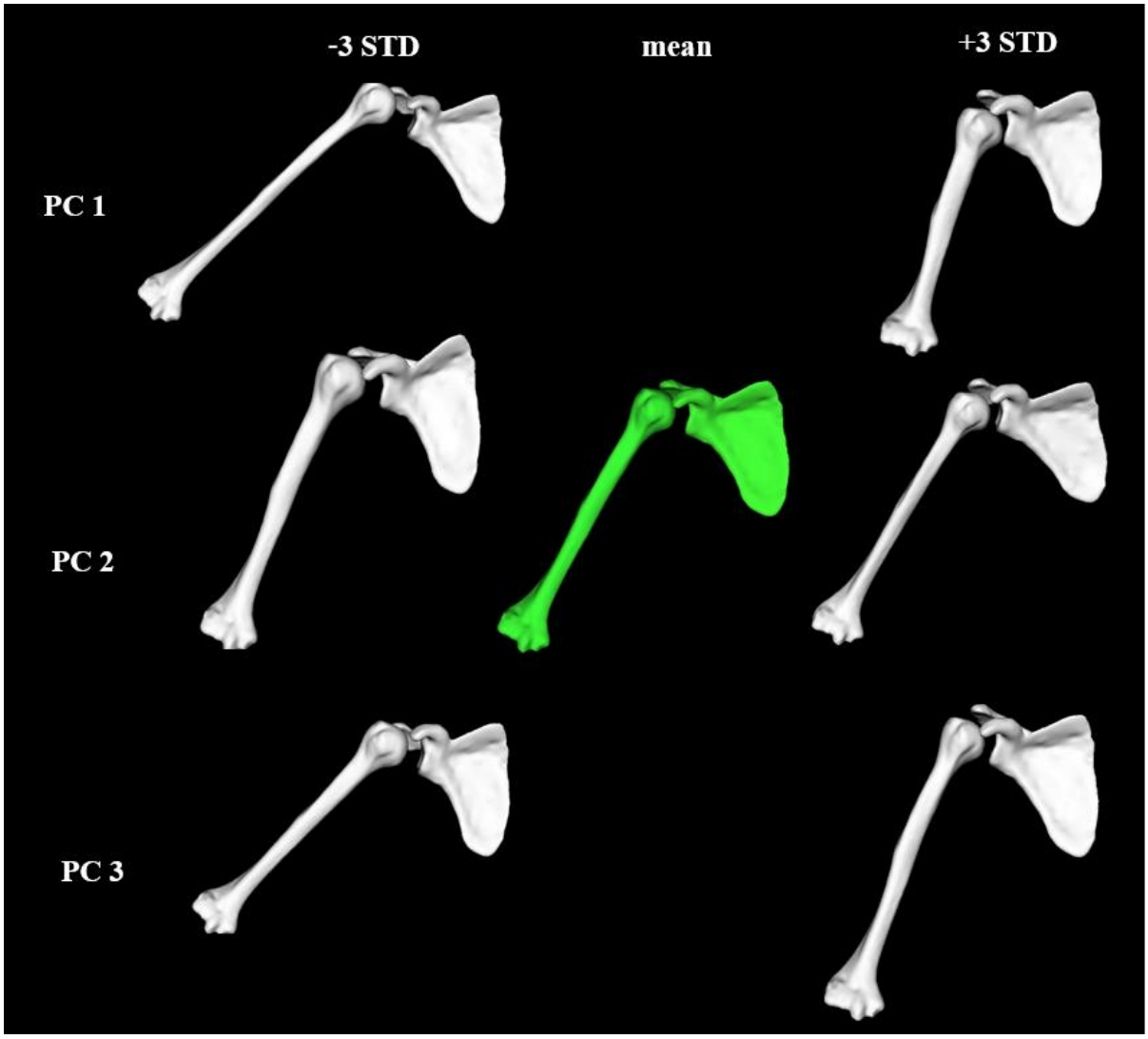

Figure 6.1. The first three PCs (modes of variation) of the abduction ASSM of the shoulder joint at 16^0 abduction. The first, second, and third rows illustrate the first, second, and third modes of variation, while the first and third column indicate a standard deviation (STD) bandwidth of -3 and +3 about the mean complex (middle column)

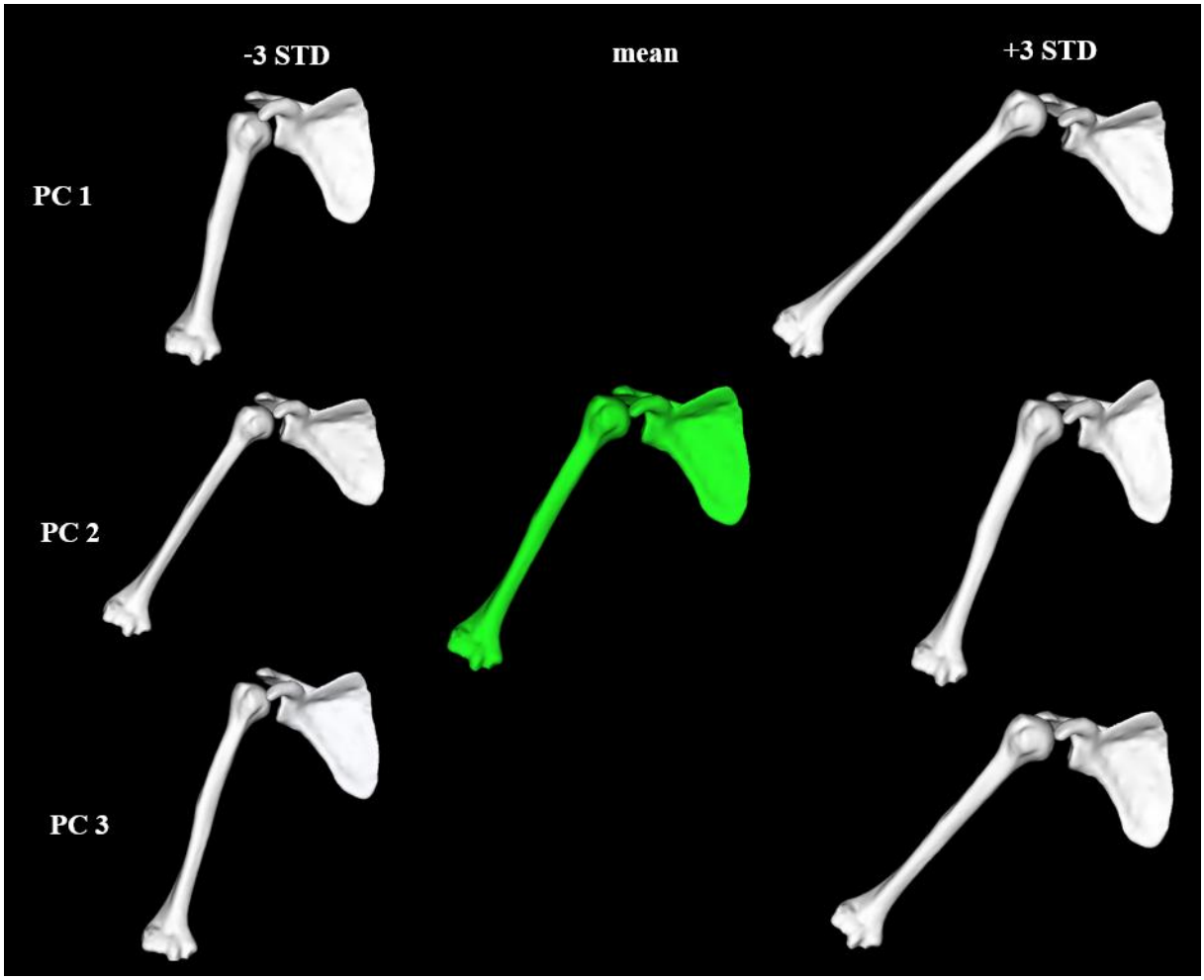

Figure 6.2. The first three PCs (modes of variation) of the abduction ASSM of the shoulder joint at 30^0 abduction. The first, second, and third rows illustrate the first, second, and third modes of variation, while the first and third column indicate a STD bandwidth of -3 and +3 about the mean complex (middle column)

Figures 6.3 and 6.4 depict the shape and pose variation of the flexion ASSM at 16^0 in frontal and sagittal plane, respectively. From -3 STD to +3STD along the first PC, the scapula lateral and superior borders become less curved; and the scapular notch becomes narrower and less deep. Additionally, the humeral head moves from superior to inferior position with respect to the glenoid. For the second PC, the shape variability on the lateral and superior borders increases in curvature, and there is an increase in the depth of the scapular notch from -3 STD to +3STD. With regards to pose variation, a slight impingement occurs from -3 STD to +3 STD along the second PC. For the third PC, both the lateral and superior borders change in curvature. Similar to the second PC, impingement also occurs from -3STD to +3 STD.

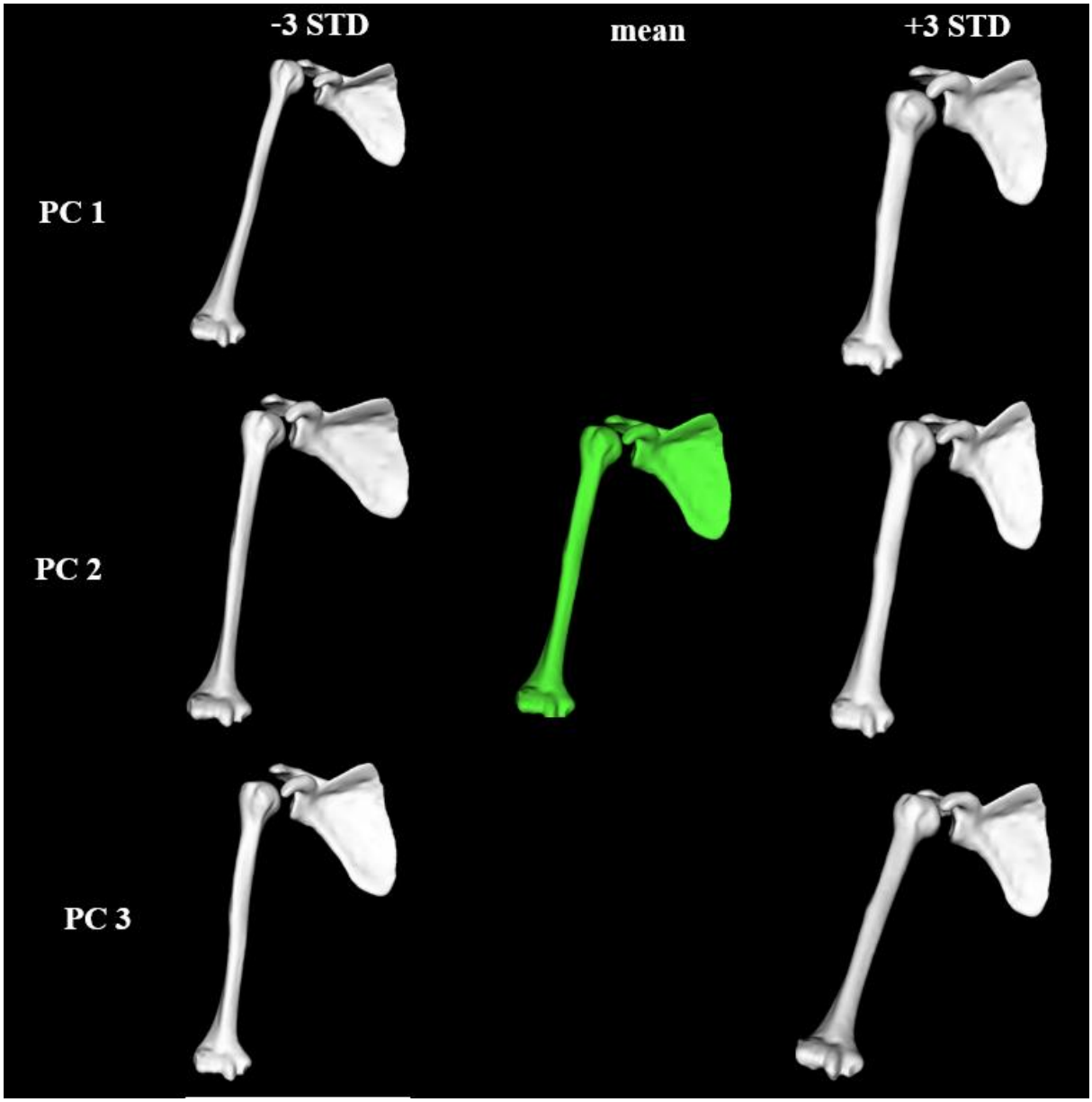

Figure 6.3. The first three PCs (modes of variation) of the flexion ASSM of the shoulder joint at 16^0 flexion (frontal plane). The first, second, and third rows illustrate the first, second, and third modes of variation, while the first and third column indicate a STD bandwidth of -3 and +3 about the mean complex (middle column)

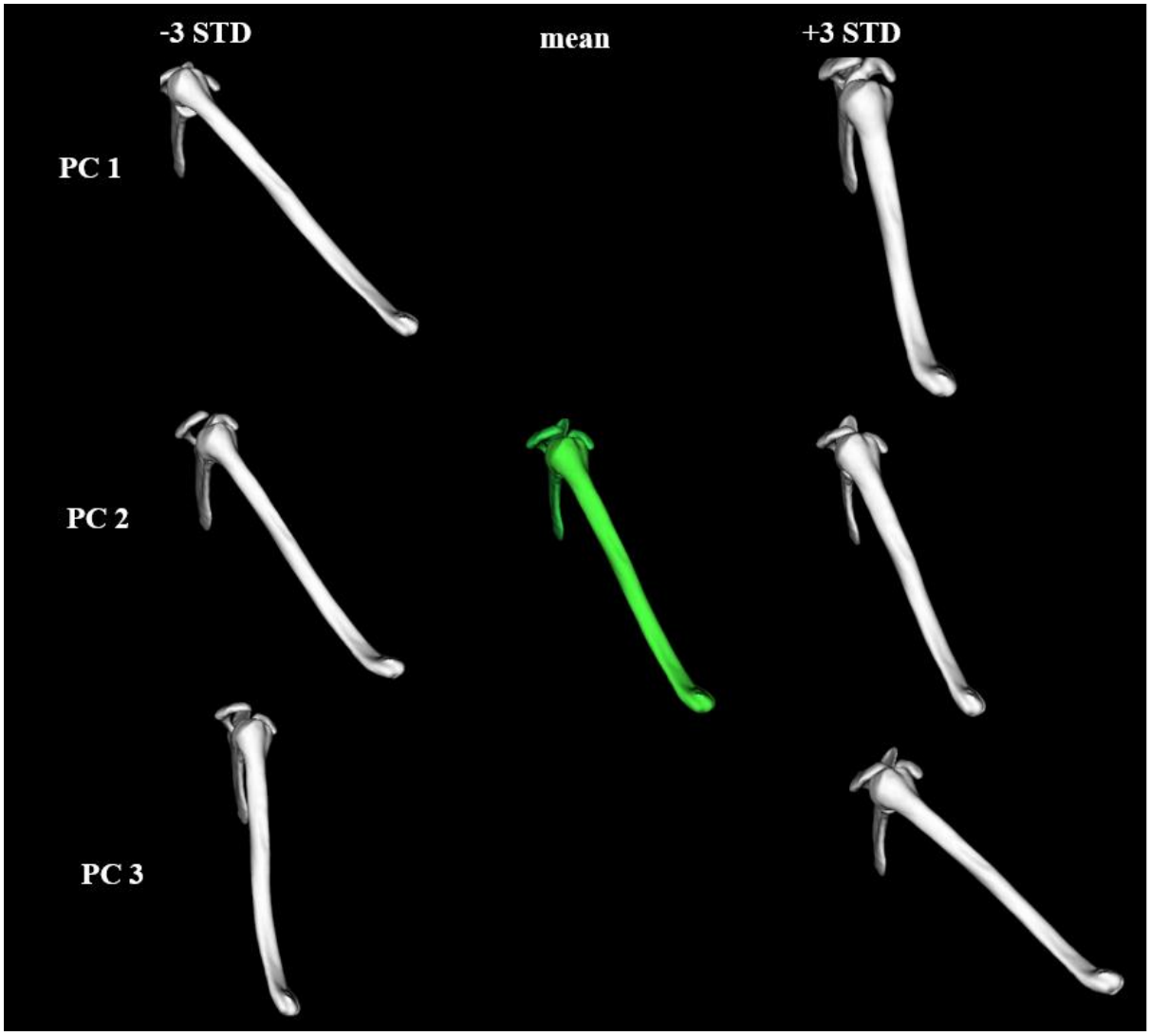

Figure 6.4. The first three PCs (modes of variation) of the flexion ASSM of the shoulder joint at 16^0 flexion (sagittal plane). The first, second, and third rows illustrate the first, second, and third modes of variation, while the first and third column indicate STD bandwidth of -3 and +3 about the mean complex (middle column)

Figures 6.5 and 6.6 depict shape and pose variation of the flexion ASSM at 30^0; in the frontal and sagittal planes, respectively. The scapula lateral border becomes less curved; and the scapular notch becomes narrower and less deep along the first PC from -3 STD to +3 STD. In addition, there is some size related variation visible on the humerus. In terms of motion encoded, the humeral head varies from a superior to an inferior position with respect to the glenoid; from -3 STD to +3STD. For the second PC, the shape variability on the lateral and superior borders increases in curvature, and there is an increase in the depth of the scapular notch from -3 STD to +3STD. Slight impingement occurs from -3 STD to +3 STD. For the third PC, the superior border becomes less curved from -3 STD to +3 STD. The motion generated is similar to that of the second PC. There is no significant shape variation observable

between the two references angles. This means regardless of starting point the motion and shapes encoded are the same, i.e. the shape and the motion generated at 30^0 flexion is very similar with those generated at 16^0 flexion.

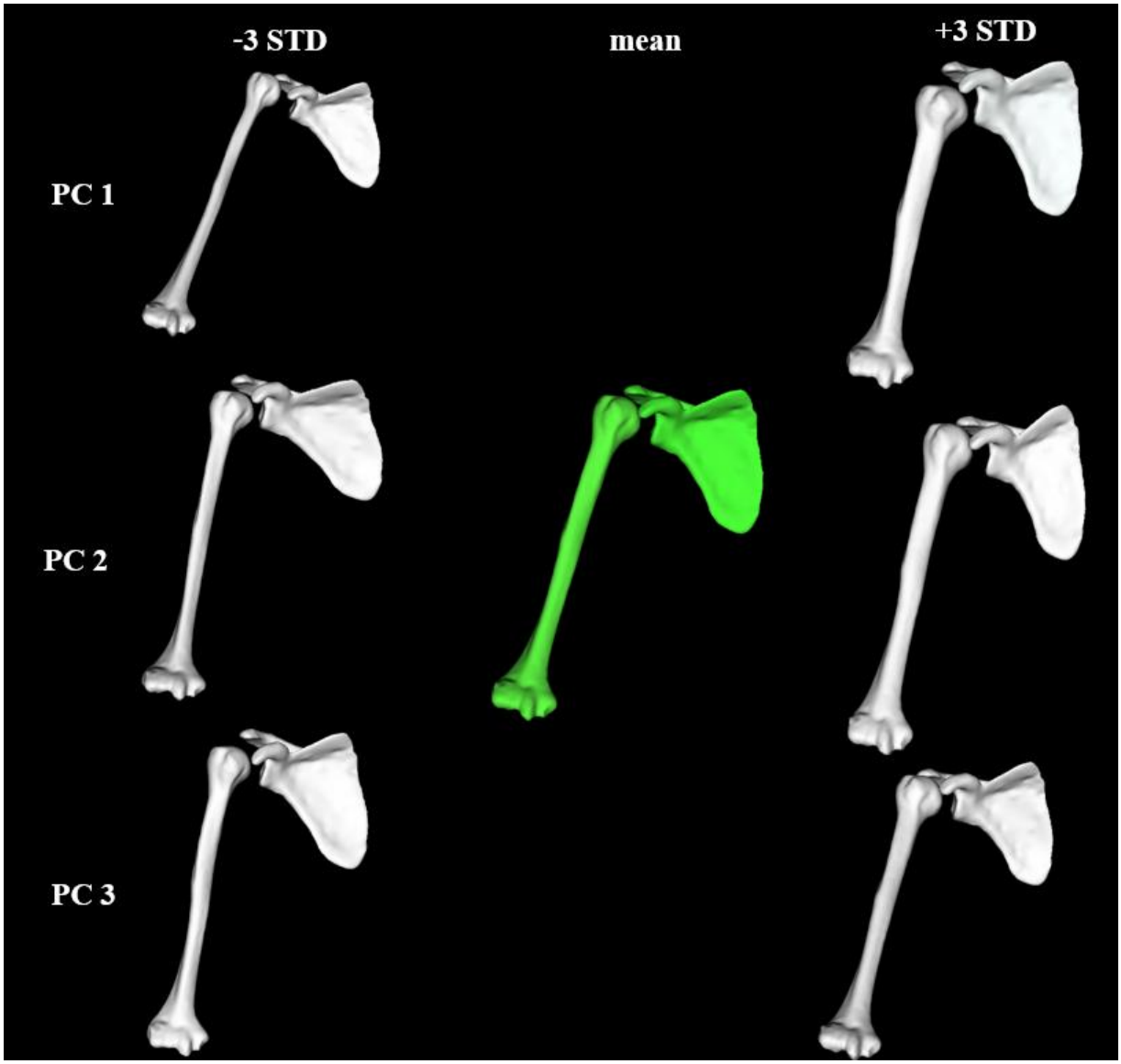

Figure 6.5. The first three PCs (modes of variation) of the flexion ASSM of the shoulder joint at 30^0 flexion (frontal plane). The first, second, and third rows illustrate the first, second, and third modes of variation, while the first and third column indicate a STD bandwidth of -3 and +3 about the mean complex (middle column)

Finally Figure 6.7 and 6.8 illustrate the shape variation of the internal rotation ASSM at 16^0 and 30^0, respectively. For the first PC, from -3 STD to +3STD, both the lateral and superior borders become less curved. In addition, the scapular notch changes to become narrower. Changes in the humerus shape occur at humeral head and deltoid tuberosity for that STD bandwidth. There is no observable difference between the first and second PCs with both

exhibiting a realistic articulation between the humeral head and the glenoid. For the third PC, the lateral border and the scapular notch become slightly curved and narrower. Similar to the first and second PCs, realistic motion is adhered to throughout the bandwidth of the STD.

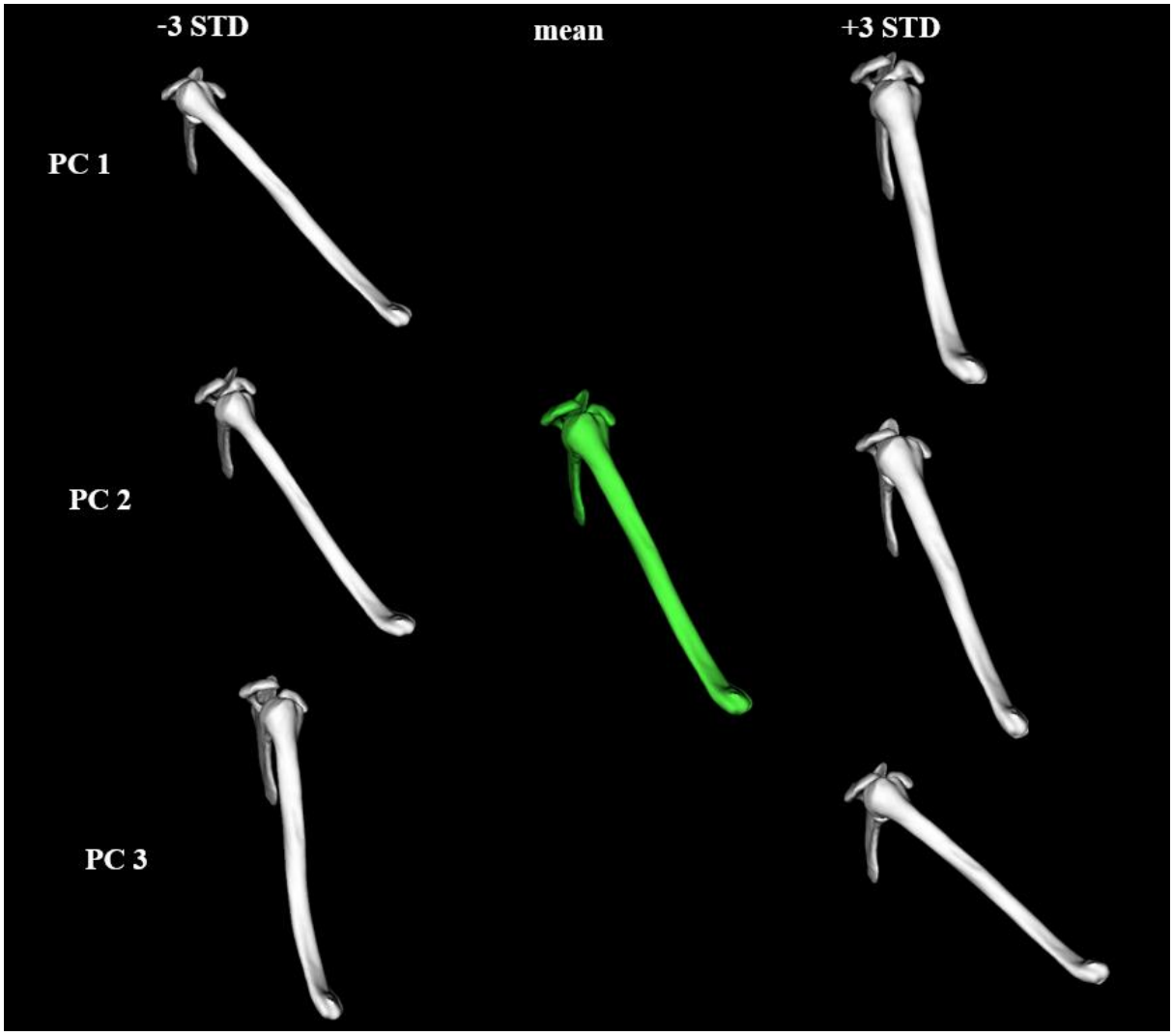

Figure 6.6. The first three PCs (modes of variation) of the flexion ASSM of the shoulder joint at 30^0 flexion (sagittal plane). The first, second, and third rows illustrate the first, second, and third modes of variation, while the first and third column indicate a STD bandwidth of -3 and +3 about the mean complex (middle column)

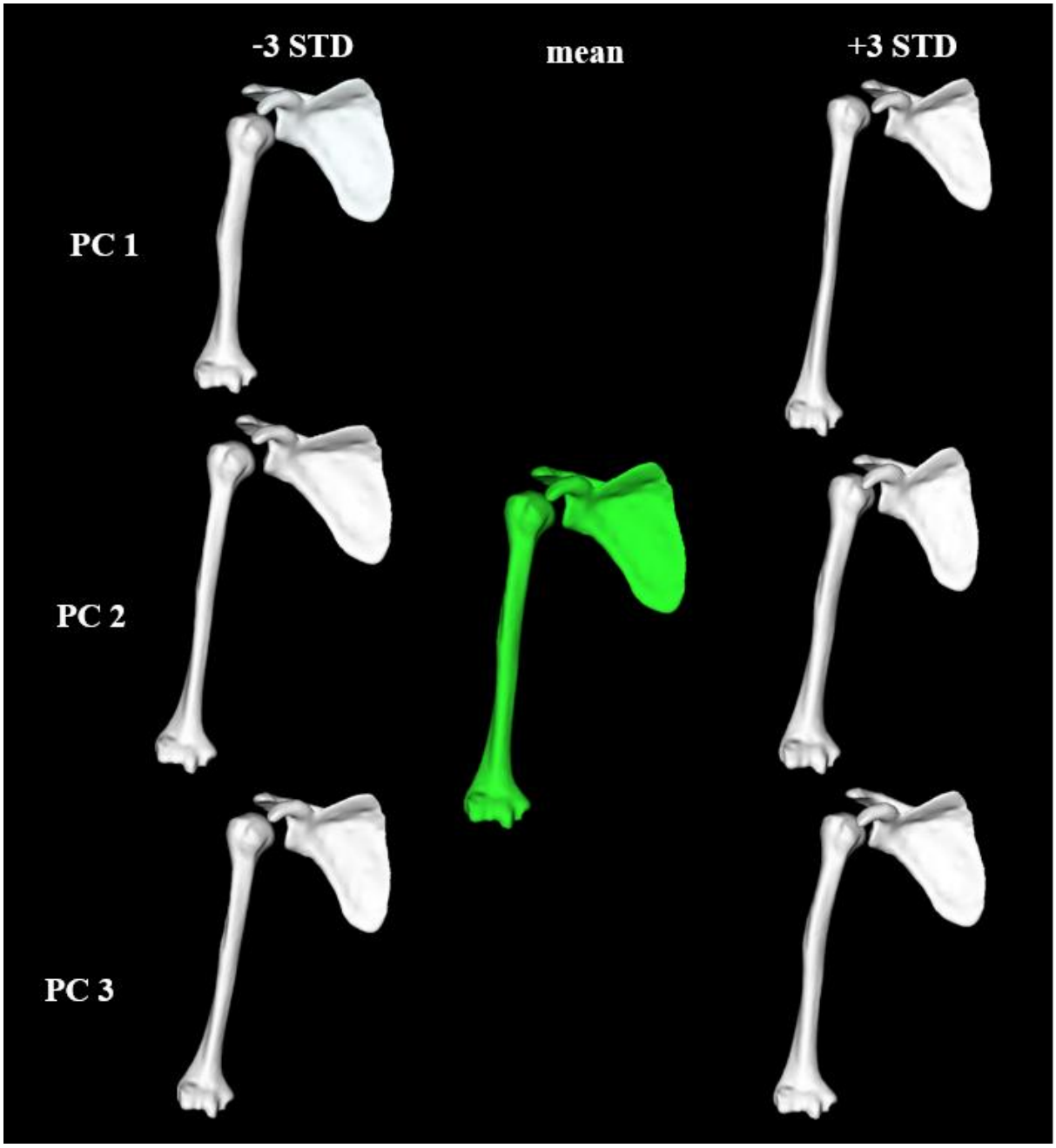

Figure 6.7. The first three PCs (modes of variation) of the internal rotation ASSM of the shoulder joint at 16^0 internal rotation. The first, second, and third rows illustrate the first, second, and third modes of variation, while the first and third column indicate a STD bandwidth of -3 and +3 about the mean complex (middle column)

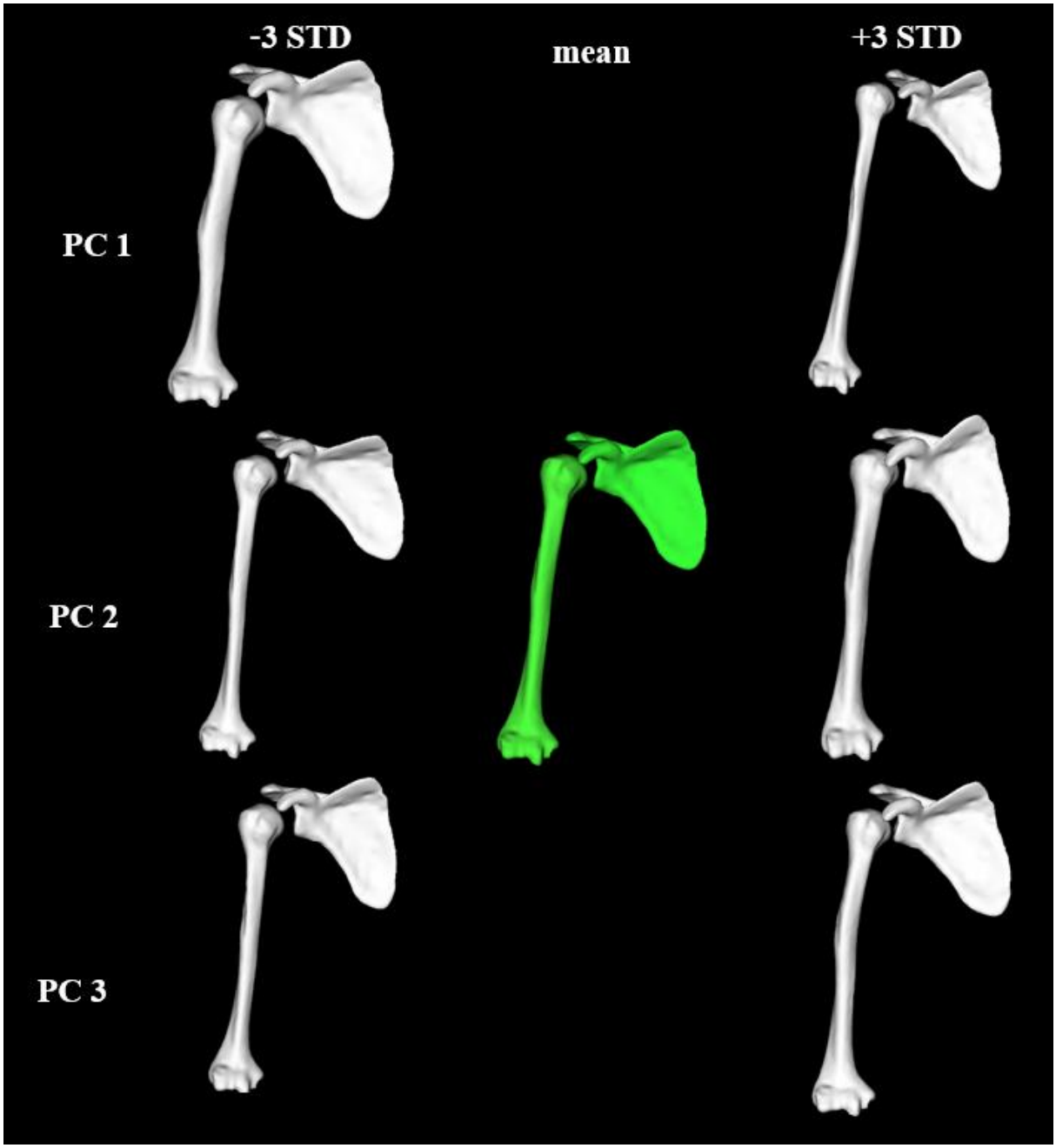

Figure 6.8. The first three PCs (modes of variation) of the internal rotation ASSM of the shoulder joint at 30^0 internal rotation. The first, second, and third rows illustrate the first, second, and third modes of variation, while the first and third column indicate a STD bandwidth of -3 and +3 about the mean complex (middle column)

In general, the shape changes are more noticeable in the scapula than the humerus, the lateral and superior borders and the scapular notch being the regions exhibiting the highest variability. Most of the humeral variation is in the length and thickness of the humeral shaft. In addition, the correlation between the shape and the synthetic pose generated behave as expected. However, comparing the two reference poses (16^0 to 30^0), differences occur in shape

and pose variability for the abduction ASSM. There is no significant shape and pose variation between the two reference angles for the flexion and internal rotation ASSMs.

6.2. Validation of ASSMs

In addition to the visual validation above, the quality of the different ASSMs were validated numerically to ensure that: 1) samples from the models represented plausible anatomical shapes and encoded realistic joint motion (generality); 2) the models could explain the training data in terms of shapes and prescribed motion (specificity); and 3) the model required as few parameters as possible to explain most of the variability in the training data (compactness). It should be noted that model validation here evaluates internal model consistency (i.e. does the model behave as expected given the encoded correlation between natural shape and synthetic motion).

6.2.1. Method adopted for validation

To assess model quality, training and test motion data were generated from the in-correspondence shoulder data. Tables 6.2 to 6.4 show the training and test motion simulated to assess the generality measure of the three motions: abduction, flexion internal rotation, respectively. For each motion, samples from the training data were selected with a 2^0 interval between the samples. These samples were used to develop each of the motion models. Test samples were selected at 4^0 intervals. These were the targets for the evaluation. This experimental design meant that all test data were within the motion range of the training data but had different shapes from any of the test data. Furthermore, the ordering of training and test samples for each motion was different so that no data grouping was used for more than one motion. The rationale for this design was to avoid the same samples being used in model building for more than one motion.

For each evaluation, one hundred samples were drawn from each model and then compared using surface to surface distance (for shape) and angle (for pose) to the each of the test samples. The metric used for the shape comparison was the Hausdorff distance. The samples from the model with the least shape and pose differences to the targets were recorded.

Table 6.2. Data generated for abduction ASSM generality assessment

Sample number	Training data samples	Pose simulated on training data samples	Test data samples	Pose simulated on test data samples
1	Data set range from 11 to 36		Data set range from 1 to 10	0^0
2				4^0
3				8^0
4				12^0
5				16^0
6				20^0
7				24^0
8				28^0
9				32^0
10				36^0
11		0^0		
12		2^0		
13		4^0		
14		6^0		
15		8^0		
16		10^0		
17		12^0		
18		14^0		
19		16^0		
20		18^0		
21		20^0		
22		22^0		
23		24^0		
24		26^0		
25		28^0		
26		30^0		
27		32^0		
28		34^0		
29		36^0		
30		38^0		
31		40^0		
32		42^0		
33		44^0		
34		46^0		
35		48^0		
36		50^0		

Table 6.3. Data generated for flexion ASSM generality assessment

Sample number	Training data samples	Pose simulated on training data samples	Test data samples	Pose simulated on test data samples
1	Data set range from 1 to 10 and 21 to 36	0^0	Data set range from 11 to 20	
2		2^0		
3		4^0		
4		6^0		
5		8^0		
6		10^0		
7		12^0		
8		14^0		
9		16^0		
10		18^0		
11				0^0
12				4^0
13				8^0
14				12^0
15				16^0
16				20^0
17				24^0
18				28^0
19				32^0
20				36^0
21		20^0		
22		22^0		
23		24^0		
24		26^0		
25		28^0		
26		30^0		
27		32^0		
28		34^0		
29		36^0		
30		38^0		
31		40^0		
32		42^0		
33		44^0		
34		46^0		
35		48^0		
36		50^0		

Table 6.4. Data generated for internal rotation ASSM generality assessment

Sample number	Training data samples	Pose simulated on training data samples	Test data samples	Pose simulated on test data samples
1	Data set range from 1 to 20 and 31 to 36	0^0	Data set range from 21 to 30	
2		2^0		
3		4^0		
4		6^0		
5		8^0		
6		10^0		
7		12^0		
8		14^0		
9		16^0		
10		18^0		
11		20^0		
12		22^0		
13		24^0		
14		26^0		
15		28^0		
16		30^0		
17		32^0		
18		34^0		
19		36^0		
20		38^0		
21				0^0
22				4^0
23				8^0
24				12^0
25				16^0
26				20^0
27				24^0
28				28^0
29				32^0
30				36^0
31		40^0		
32		42^0		
33		44^0		
34		46^0		
35		48^0		
36		50^0		

Tables 6.5 shows the training and test motion simulated to assess the specificity measure of the three motions: abduction, flexion internal rotation, respectively. For each motion, samples from the training data were selected with a 1^0 interval between the samples. These samples were used to develop each of the motion models. Test samples were selected at 4^0

intervals. Similar to the generality measure, the training and test samples for each motion were also different in order to avoid the same samples being used in model building of each motion.

For compactness, the model should have as little variance as possible and requires to use fewer parameters as possible to represent higher shape instances.

Table 6.5. Data generated for ASSM specificity assessment for each of the three motions (abduction, flexion, and internal rotation)

Sample number	Pose simulated on training data samples	Pose simulated on test data samples
1	0^0	0^0
2	1^0	
3	2^0	
4	3^0	
5	4^0	4^0
6	5^0	
7	6^0	
8	7^0	
9	8^0	8^0
10	9^0	
11	10^0	
12	11^0	
13	12^0	12^0
14	13^0	
15	14^0	
16	15^0	
17	16^0	16^0
18	17^0	
19	18^0	
20	19^0	
21	20^0	20^0
22	21^0	
23	22^0	
24	23^0	
25	24^0	24^0
26	25^0	
27	26^0	
28	27^0	
29	28^0	28^0
30	29^0	
31	30^0	
32	31^0	
33	32^0	32^0
34	33^0	
35	34^0	
36	35^0	36^0

6.2.2. Results of validation

The generality, specificity, and compactness measures for the anatomical motion (abduction, flexion and internal rotation) were generated. Table 6.6 to 6.8 indicate the generalization measure as well as table 6.9 to 6.11 express the specificity measure for the motion of abduction, flexion, and internal rotation, respectively. The tables indicate the smallest Hausdorff distance metrics of the scapula and humerus bone as well as the pose angle difference between the generated test samples and the specified test data. The compactness results in figure 6.9 show that the first 10 principal components of the ASSM represented 95.16% of the variance.

The specificity and generalization measures computed for the recommended test data are shown in appendix A.

Generality

Table 6.6. The smallest Hausdorff distance of generalization measure for abduction

motion	humerus error (mm)	scapula error (mm)	pose error (rad)
$\mathbf{0^0}$	4.02	5.96	0.14
$\mathbf{4^0}$	3.45	6.93	0.15
$\mathbf{8^0}$	3.66	5.71	0.19
$\mathbf{12^0}$	4.12	5.8	0.18
$\mathbf{16^0}$	3.73	6.69	0.17
$\mathbf{20^0}$	3.77	7.34	0.15
$\mathbf{24^0}$	4.44	7.24	0.26
$\mathbf{28^0}$	3.44	6.84	0.39
$\mathbf{32^0}$	3.19	6.85	0.36
$\mathbf{36^0}$	3.31	5.95	0.36

Table 6.7. The smallest Hausdorff distance of generalization measure for flexion

motion	humerus error (mm)	scapula error (mm)	pose error (rad)
$\mathbf{0^0}$	3.69	7.75	0.02
$\mathbf{4^0}$	3.84	7.21	0.09
$\mathbf{8^0}$	3.84	7.29	0.07
$\mathbf{12^0}$	3.71	6.92	0.31
$\mathbf{16^0}$	3.94	6.77	0.2
$\mathbf{20^0}$	3.41	7.3	0.46
$\mathbf{24^0}$	3.79	7.23	0.39
$\mathbf{28^0}$	4.44	6.24	0.49
$\mathbf{32^0}$	3.58	7.52	0.48
$\mathbf{36^0}$	3.39	7.66	0.68

Table 6.8. The smallest Hausdorff distance of generalization measure for internal rotation

Motion	humerus error (mm)	scapula error (mm)	pose error (rad)
0^0	3.33	5.57	0.14
4^0	3.61	5.45	0.14
8^0	2.16	4.64	0.13
12^0	3.26	2.48	0.14
16^0	3.05	5.45	0.27
20^0	2.54	5.84	0.24
24^0	3.24	5.67	0.39
28^0	3.27	5.52	0.31
32^0	3.47	5.44	0.44
36^0	3.14	5.06	0.36

Specificity

Table 6.9. The smallest Hausdorff distance of specificity measure for abduction motion

motion	humerus error (mm)	scapula error (mm)	pose error (rad)
0^0	3.88	6.43	0.17
4^0	3.26	6.32	0.17
8^0	4.21	6.11	0.14
12^0	3.42	5.51	0.14
16^0	3.7	6.35	0.15
20^0	3.63	6.47	0.2
24^0	3.79	5.39	0.22
28^0	3.14	5.18	0.41
32^0	3.58	4.95	0.32
36^0	3.72	5.91	0.71

Table 6.10. The smallest Hausdorff distance of specificity measure for flexion

motion	humerus error (mm)	scapula error (mm)	pose error (rad)
0^0	3.88	6.43	0.05
4^0	3.98	5.17	0.17
8^0	3.89	5.76	0.24
12^0	3.06	4.79	0.11
16^0	3.72	6.22	0.19
20^0	3.51	5.23	0.37
24^0	4.2	6.08	0.45
28^0	3.76	6.36	0.42
32^0	3.67	5.75	0.55
36^0	3.47	5.67	0.65

Table 6.11. The smallest Hausdorff distance of specificity measure for internal rotation

motion	humerus error (mm)	scapula error (mm)	pose error (rad)
0^0	3.88	6.43	0.05
4^0	3.82	5.94	0.13
8^0	3.54	6.24	0.19
12^0	3.13	6.38	0.13
16^0	3.73	5.8	0.15
20^0	3.05	6.01	0.32
24^0	3.2	4.82	0.35
28^0	3.46	6.77	0.35
32^0	3.57	6.43	0.38
36^0	3.69	5.46	0.48

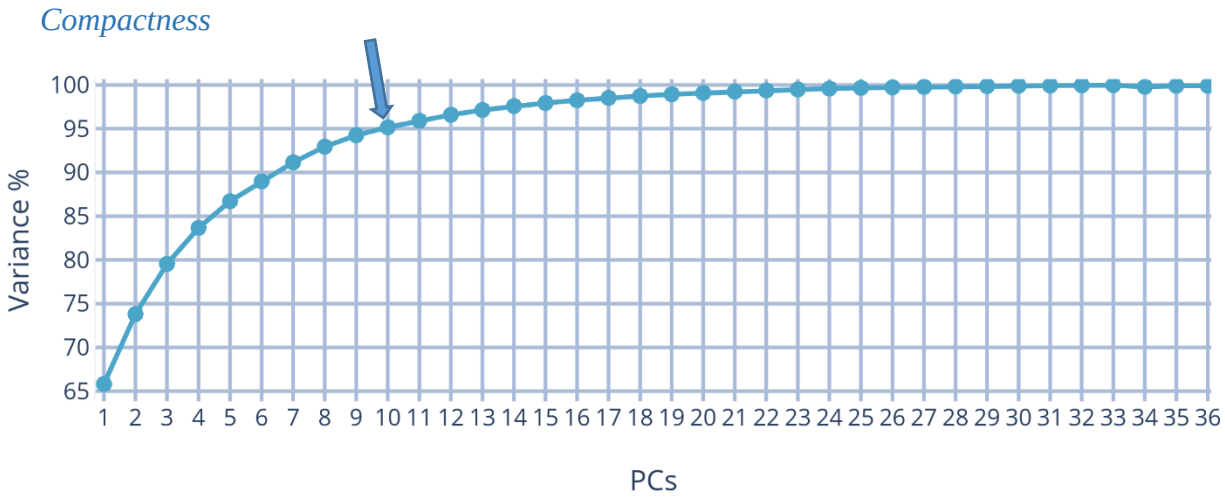

Figure 6.9. Compactness of ASSM (the blue arrow indicates to the region where the first ten PCs represent 95.16% of the total variance).

6.3. Chapter summary

This chapter described the development and validation of an ASSM of the shoulder joint from in-correspondence 3D surface meshes. Six ASSM were built, two for each specific motion (16^0 and 30^0). Building ASSM at different specific angle motion able to compare the correlation existed between the shape and the pose. The models were evaluated based on the model quality measures generality, specificity, and compactness as well as pose variability parameters.

7. DISCUSSION

This chapter discusses the results of the project on the development of an articulated statistical shape model (ASSM) of the shoulder joint. The limitations of the project and the opportunities for future work are also discussed.

7.1. Establishing shape and kinematics correspondence

Landmarking of the 3D mesh data was critical for guiding the surface to surface registration required to establish dense correspondence. An analysis of inter-operator landmark variability on both the humerus and scapula was previously reported by Inyang et al. (2017). They reported variability of greater than 3 mm for both bones. The variabilities presented in this dissertation are less than 1.4 mm. The results indicate that landmarking precision and reliability was acceptable and as such the landmarking would have minimal impact on the registration error. It should be noted that there are other approaches to calculating landmarking reproducibility (Bartlett and Frost, 2008). However, the method used to determine the reproducibility in this study was selected because it is easy to interpret (Weinberg et al., 2004). Future work could look at performing a sensitivity analysis to determine the impact of landmarks on the final model.

Although the 3D meshes of the shoulder bones existing in random poses, the registration protocol developed managed to achieve dense correspondence in training data using free form deformation models (FFDM). The main contributions of the developed registration protocol were: 1) the use of multiscale kernels for the FFDM which allowed for better registration. 2) inclusion of an unbiased reference in developing the FFDMs for each bone; and 3) the ability to retain the shape and kinematics relationship existing during the imaging after establishing dense correspondence.

The FFDM is defined by the mean and the squared exponential kernel (SEK) called the Gaussian kernel, parametrised by the value of the span (s) and the degree (σ). For the humerus, only one SEK was used. However, because of the morphological complexity of the scapula, a combination of seven SEKs were used. The combined kernels represent the global, medium, and local deformation scales that allowed for multiscale deformability in the scapula FFDM. An analysis of registration error on both the humerus and scapula was previously reported by Mutsvangwa et al. (2015). They reported the average error 1.41mm and 2.46mm for the humerus and scapula, respectively. However, the average error presented in this dissertation are lower at 1.15 mm and 1.79 mm, respectively. Meanwhile, the maximum registration error

from the humeri and scapulae data were 2.30 mm and 2.51mm, these result indicated that there might be higher anatomical variability between the deformed reference mesh and the original data samples.

Median virtual shapes (*mvs*) of the humerus and scapula, created using iterative median closest point Gaussian mixture model (IMCP-GMM), were used as a references for the FFDM. The advantage of using the *mvs* as references for the FFDM, rather than random examples from the training data, is that *mvs* remove any implicit topological bias in the FFDM models (Mutsvangwa et al., 2015). The deformation ability for both bones, as gauged using final Hausdorff distance after fitting FFDM, was less than 2.5 mm. This result is lower than that reported in Inyang et al. (2017) which was less than 12mm for both bones. The fits were morphologically close to their respective target meshes. This justified the use of the fits (which were in dense correspondence), instead of the original meshes, for subsequent steps.

Finally, the shape and kinematics relationship between the two bones was maintained by adopting the inverse transformation approach presented in Fouefack et al. (2019).

7.2. Generating synthetic pose variability from the registered mesh

For the development of glenohumeral (GH) joint kinematics there were three essential steps developed for generating synthetic motions: 1) Identifying relevant bony landmarks on each bone to define local coordinate systems; 2) Determining the glenohumeral rotational center (GHRC); 3) The establishment of the joint coordinate system (JCS).

As mentioned above the bony landmarks are used as constraints during the coordinate system definition. Typically these are identified by experts in order to keep the coordinate system consistent across the landmarking process. Large precision errors in anatomical landmark localization may result in mislocation and disorientation of the JCS that would seriously impact kinematics motion analysis (Marin et al., 2003). The mean intra-operator landmarking error for the humerus and scapula were 0.16 and 0.30 mm, respectively; much less than the landmarking error in the registration process. The smaller errors could be attributed to the fact that the later landmarking process was performed on training data already in correspondence meaning that the same vertices could be targeted in the mesh.

The GHRC can be defined using either one of two different approaches; predictive and functional. There are different methods reported for the functional approach leading to significantly different GHRC locations, depending on method. However sphere fitting and helical axis are reported to be the most reliable and accurate (Lempereur et al., 2010). In this project, the sphere fitting approach was adopted and it computes the GHRC by fitting a sphere

to the humeral head such that the centre of the sphere indicates the GHRC. However, since the GHRC locations are subject-specific, varying according to each subject's morphology, it was difficult to compare the GHRC values obtained in this project with other studies in the literature. The definition of two coordinate systems is required in order to determine JCS; one proximal, and one distal. In this study, the proximal and distal segments were represented by humerus local coordinate system and the scapula local coordinate system, respectively. The GHRC were computed as per International Society of Biomechanics (ISB) recommendation. Dey et al. (2018) reported a morphometry study on healthy humeri; comparing morphology between South African and Swiss populations. They computed and compared the radius of the humeral head on the two population while using a sphere fitting algorithm developed on MATLAB (MathWorks, Natick, MA, USA). The average humeral head radius and standard deviation for the South African population were 23.2mm and 2.6mm, respectively. The same South African shoulder data were used in this project and the mean radius and the standard deviation were 22.71 and 2.11mm, respectively. The results presented here are consistent with those presented by Dey et al. (2018). This further validates the implementation of the sphere-fitting and GHRC prediction reported in this project.

Shoulder joint kinematics refers to shoulder joint motion based on its degrees of freedom (DoF). Movements are initialized from the resting (0^0) position. During determination of the 0^0 position the humerus (mobile) axes are positioned parallel and coincident to the axes of the scapula (reference) frame as described in (Levasseur et al., 2007). The GH orientation is defined using an Euler angle sequence. Euler angles describe the motion at a joint using a rotation sequence, representing the 3D motion as a series of independent rotations about each of the three rotational DoF. In this project, the rotation was done on the distal (humerus) body coordinate system with respect to the proximal body coordinate system. The GH joint rotations can be computed using *YXY* Euler sequence, however, in order to avoid gimbal lock (Piazza and Cavanagh, 2000), the *XZY* sequence was used for the GH motion analysis. Gimbal lock refers to the adverse interaction between rotations about each of the three axes in the Euler sequence, i.e., the computed angles of rotation may not represent the true anatomical angle of rotation. Phadke et al. (2011) reported a comparison of GH motion between *YXY* and *XZY* sequence and recommended that the *XZY* sequence, was relatively more immune to gimbal lock, and was preferable for describing GH motion. Šenk and Chèze (2006) investigated different Euler sequences for GH motions and found that *XZY* sequence was the most preferable to describe the humerus elevation in the scapular or frontal plane. Finally, Bonnefoy-Mazure

et al. (2010) looked at different rotation sequences to describe the humerus motion and also concluded that *XZY* did not expose the analysed motion to gimbal lock.

7.3. Development and validation of ASSM of the shoulder joint

This study showed the development of a Gaussian process morphable model (GPMM) combining shape and kinematics parameters to form an ASSM of the shoulder joint from the training samples. The developed ASSM of the shoulder joint may be used to study the shape and kinematics variability in training samples as well as allowing for an analysis of the kinematics, separately, when we are not interested in the shape variability. The ASSM framework has several potential applications such as generalization of patient-specific motion, improvement of shoulder joint segmentation accuracy, and allowing for a more accurate reconstruction of pathological joints. However, as synthetic data was used in this study, the GH joint characteristics obtained may not faithfully represent real dynamic data.

The generality, specificity, and compactness measures were adopted for assessing ASSM model quality. For the generality and specificity, the three validation results (humerus, scapula, and pose error) were presented for each of the three synthesised motions (abduction, flexion, and internal rotation). The generality, used to gauge the quality of the models for outside-of-training scapula and humerus shapes, ranged between 5.95 mm and 7.75 mm (scapula), and between 2.16 mm and 4.44 mm (humerus). The specificity, to gauge in-training shape explanation, ranged between 4.79 mm and 6.77 mm (scapula), and between 3.05 mm and 4.21 mm (humerus). The obtained generality values for the scapula shape are similar to those of a previous study (Mutsvangwa et al., 2015), which ranged between 5.30 mm and 9.0 mm. However, the specificity values in the present study were much higher than those from the Mutsvangwa et al. study, which ranged between 1.4 mm and 1.6 mm. Additionally, the generality and the specificity values of the humerus presented here were much higher compared to another study for which they ranged from 1.9 mm to 1.7 mm, and 2.0 mm to 1.2 mm, respectively (Inyang et al., 2017). The registration method which had been implemented in previous two studies was similar to this project however, the size of the training data used in Mutsvangwa et al. and Inyang et al. were 28 and 18 coupled humeri and scapulae, respectively. With regard to compactness, the first 10 principal components of the ASSM represented 95.16% of the variance. To the author's best knowledge no previous pose validation studies have been reported on ASSM of the shoulder joint. As such there were no results in the literature with which to compare the pose validation presented here.

7.4. Limitations

This research focussed on developing an ASSM of the shoulder joint with a restricted range of motion ($0 - 50^0$). As such the results and conclusions drawn only apply to motion types (abduction, flexion and, and internal rotation) within this range. An additional limitation was that the images were of non-pathological shoulders. Thus the results described in this dissertation only represent healthy joints. Finally, there were no dynamic data for any of the joints and synthetic pose had to be generated to develop the models. Although visually realistic and following ISB recommendations in its generation, the synthetic data is not a substitute for real dynamic data.

7.5. Conclusion and future work

This project reported the development of an articulated statistical shape modelling (ASSM) framework for evaluating the correlation between the articular geometry and pose. The framework has potential for unpacking the relationship between the shapes of the humerus and the scapula, and how that relationship affects the motion of the GH joint. Future work will aim to extend the approach to the full range of pose variation and more complex movements such as circumduction exhibited by non-pathological and pathological shoulders.

7.6. Project output

The following conference paper emanated from this work:

- Fouefack, J.-R., Alemneh, T., Borotikar, B., Burdin, V., Douglas, T. S. & Mutsvangwa, T. Statistical shape-kinematics models of the skeletal joints: Application to the shoulder complex, 2019 41st Annual International Conference of the IEEE Engineering in Medicine and Biology Society (EMBC), Berlin, Germany, 2019, pp, 4815-4818.

References

Bartlett, J. & Frost, C. (2008). Reliability, repeatability and reproducibility: analysis of measurement errors in continuous variables. *Ultrasound in Obstetrics and Gynecology: The Official Journal of the International Society of Ultrasound in Obstetrics and Gynecology,* 31**,** 466-475. https://doi.org/10.1002/uog.57955

Berlinet, A. & Thomas-Agnan, C. (2011). Reproducing kernel Hilbert spaces in probability and statistics, *Springer Science & Business Media. New York*

Besl, P. J. & Mckay, N. D. (1992). Method for registration of 3-D shapes. *International Society for Optics and Photonics,* 586-607. https://doi.org/10.1117/12.57955

Bindernagel, M. (2013). Articulated Statistical Shape Models. MSc. Thesis. Humboldt-Universität zu Berlin. Available: https://www.zib.de/lamecker/research/Bindernagel-Diplom.pdf

Bindernagel, M., Kainmueller, D., Seim, H., Lamecker, H., Zachow, S. & Hege, H.-C. (2011). An articulated statistical shape model of the human knee. *Bildverarbeitung für die Medizin 2011***,** 59-63. https://doi.org/10.1007/978-3-642-19335-4_14

Bonnefoy-mazure, A., Slawinski, J., Riquet, A., Lévèque, J.-M., Miller, C. & Cheze, L. (2010). Rotation sequence is an important factor in shoulder kinematics. Application to the elite players' flat serves. *Journal of Biomechanics,* 43(10)**,** 2022-2025. https://doi.org/10.1016/j.jbiomech.2010.03.028

Bookstein, F. L. (1989). Principal warps: Thin-plate splines and the decomposition of deformations. *IEEE Transactions on pattern analysis and machine intelligence,* 11(6)**,** 567-585. https://doi.org/10.1109/34.24792

Bookstein, F. L. (1997). Landmark methods for forms without landmarks: morphometrics of group differences in outline shape. *Medical image analysis,* 1(3)**,** 225-243. https://doi.org/10.1016/S1361-8415(97)85012-8

Borotikar, B. & Mutsvangwa, T. (2018). Entering the statistical domain: Do we understand the risk and liabilities of using Deformable Statistical Shapes in biomechanics? *8th World Congress of Biomechanics.* Dublin Ireland, 8-12 July, 2018.

Bouabene, G. Lüthi, M. (2018). Statistical Shape Modelling. Available: *https://www.futurelearn.com/courses/statistical-shape-modelling/2/todo/7748*.

Bryan, R., Nair, P. B. & Taylor, M. (2009). Use of a statistical model of the whole femur in a large scale, multi-model study of femoral neck fracture risk. *Journal of biomechanics,* 42(13)**,** 2171-2176. https://doi.org/10.1016/j.jbiomech.2009.05.038

Cates, J., Fletcher, P. T., Styner, M., Hazlett, H. C. & Whitaker, R. (2008). Particle-based shape analysis of multi-object complexes. *International Conference on Medical Image Computing and Computer-Assisted Intervention*. Springer, 477-485. https://doi.org/10.1007/978-3-540-85988-8_57

Cates, J., Fletcher, P. T., Styner, M., Shenton, M. & Whitaker, R. (2007) Shape modeling and analysis with entropy-based particle systems. *Biennial International Conference on Information Processing in Medical Imaging*. Springer, 333-345. https://doi.org/10.1007/978-3-540-73273-0_28

Chandra, S. S., Xia, Y., Engstrom, C., Crozier, S., Schwarz, R. & Fripp, J. (2014). Focused shape models for hip joint segmentation in 3D magnetic resonance images. *Medical image analysis,* 18(3)**,** 567-578. https://doi.org/10.1016/j.media.2014.02.002

Chen, X., Graham, J., Hutchinson, C. & Muir, L. (2014). Automatic generation of statistical pose and shape models for articulated joints. *IEEE transactions on medical imaging,* 33(2)**,** 372-383. https://doi.org/ 10.1109/TMI.2013.2285503

Cootes, T. F., Beeston, C., Edwards, G. J. & Taylor, C. J. (1999). A unified framework for atlas matching using active appearance models. *Biennial International Conference on Information Processing in Medical Imaging.* Springer, 322-333. https://doi.org/10.1007/3-540-48714-X_24

Cootes, T. F., Taylor, C. J., Cooper, D. H. & Graham, J. (1995). Active shape models-their training and application. *Computer vision and image understanding,* 61**,** 38-59.

Culham, E. & Peat, M. (1993). Functional anatomy of the shoulder complex. *Journal of Orthopaedic & Sports Physical Therapy*, 18(1)**,** 342-350. https://doi.org/ 10.2519/jospt.1993.18.1.342

Davies, R. H., Twining, C. J., Cootes, T. F. & Taylor, C. J. (2010). Building 3-D statistical shape models by direct optimization. *IEEE Transactions on Medical Imaging,* 29(4)**,** 961-981. https://doi.org/10.1109/TMI.2009.2035048

De Groot, J. H., Van Woensel, W. & Van der Helm, F. C. (1999). Effect of different arm loads on the position of the scapula in abduction postures. *Clinical biomechanics,* 14(5)**,** 309-314. https://doi.org/10.1016/S0268-0033(98)90094-8

Delingette, H. (1999). General object reconstruction based on simplex meshes. *International journal of computer vision,* 32**,** 111-146. https://doi.org/10.1023/A:1008157432188

Dey, R., Roche, S., Rosch, T., Mutsvangwa, T., Charilaou, J. & Sivarasu, S. (2018). Anatomic variations in glenohumeral joint: an interpopulation study. *JSES Open Access,* 2(1)**,** 1-7. https://dx.doi.org/10.1016/j.jses.2017.11.007

Dryden, I. L. & Mardia, K. V. (1998). Statistical shape analysis, *Wiley Chichester*. https://doi.org/10.1002/1097-0258(20001015)19:19<2716::AID-SIM590>3.0.CO;2-O

Ehrig, R. M., Taylor, W. R., Duda, G. N. & Heller, M. O. (2006). A survey of formal methods for determining the centre of rotation of ball joints. *Journal of biomechanics,* 39(15)**,** 2798-2809. https://doi.org/10.1016/j.jbiomech.2005.10.002

Fouefack, J.-R., Alemneh, T., Borotikar., Valerie, B., Douglas, T.S. & Mutsvangwa, T. (2019). Statistical shape-kinematics models of the skeletal joints: Application to the shoulder complex. *IEEE Engineering in Medicine and Biology Society (EMBC),* 4815-4818. https://doi.org/10.1109/EMBC.2019.8857528

Frangi, A. F., Rueckert, D., Schnabel, J. A. & Niessen, W. J. (2002). Automatic construction of multiple-object three-dimensional statistical shape models: Application to cardiac modeling. *IEEE transactions on medical imaging,* 21(9)**,** 1151-1166. https://doi.org/10.1109/TMI.2002.804426

Fripp, J., Crozier, S., Warfield, S. K. & Ourselin, S. (2007). Automatic segmentation of the bone and extraction of the bone–cartilage interface from magnetic resonance images of the knee. *Physics in Medicine & Biology,* 52(6)**,** 1617. https://doi.org/10.1088/0031-9155/52/6/005

Gamage, S. S. H. U. & Lasenby, J. (2002). New least squares solutions for estimating the average centre of rotation and the axis of rotation. *Journal of biomechanics,* 35(1)**,** 87-93. https://doi.org/10.1016/s0021-9290(01)00160-9

Gerig, T., Shahim, K., Reyes, M., Vetter, T. & Lüthi, M. (2014). Spatially varying registration using gaussian processes. *International Conference on Medical Image Computing and Computer-Assisted Intervention*. Springer, 413-420. https://doi.org/10.1007/978-3-319-10470-6_52

Giphart, J. E., Brunkhorst, J. P., Horn, N. H., Shelburne, K. B., Torry, M. R. & Millett, P. J. (2013). Effect of plane of arm elevation on glenohumeral kinematics: a normative biplane fluoroscopy study. *JBJS,* 95(3)**,** 238-245. https://doi.org/ 10.2106/JBJS.J.01875

Gorczowski, K., Styner, M., Jeong, J.-Y., Marron, J., Piven, J., Hazlett, H. C., Pizer, S. M. & Gerig, G. (2007). Statistical shape analysis of multi-object complexes. *IEEE Computer Vision and Pattern Recognition, CVPR'07* 1-8. https://doi.org/10.1109/CVPR.2007.383336

Gorczowski, K., Styner, M., Jeong, J. Y., Marron, J., Piven, J., Hazlett, H. C., Pizer, S. M. & Gerig, G. (2007). Discrimination analysis using multi-object statistics of shape and pose. *International Society for Optics and Photonics,* 65121A. https://doi.org/10.1117/12.710218

Gorczowski, K., Styner, M., Jeong, J. Y., Marron, J., Piven, J., Hazlett, H. C., Pizer, S. M. & Gerig, G. (2010). Multi-object analysis of volume, pose, and shape using statistical discrimination. *IEEE transactions on pattern analysis and machine intelligence,* 32(4)**,** 652-661. https://doi.org/10.1109/TPAMI.2009.92

Gower, J. C. (1975). Generalized procrustes analysis. *Psychometrika,* 40**,** 33-51. https://doi.org/10.1007/BF02291478

Gregory, J. S., Waarsing, J. H., Day, J., Pols, H. A., Reijman, M., Weinans, H. & Aspden, R. M. (2007). Early identification of radiographic osteoarthritis of the hip using an active shape model to quantify changes in bone morphometric features: Can hip shape tell us anything about the progression of osteoarthritis? *Arthritis & Rheumatology,* 56(11)**,** 3634-3643. https://doi.org/10.1002/art.22982

Haering, D., Raison, M. & Begon, M. (2014). Measurement and description of three-dimensional shoulder range of motion with degrees of freedom interactions. *Journal of biomechanical engineering,* 136(8)**,** 084502. https://doi.org/10.1115/1.4027665

Halvorsen, K. (2003). Bias compensated least squares estimate of the center of rotation. *Journal of Biomechanics,* 36(7)**,** 999-1008. https://doi.org/10.1016/S0021-9290(03)00070-8

Hausdorff, F. (1918). Dimension und äußeres Maß. *Mathematische Annalen,* 79**,** 157-179. https://doi.org/10.1007/BF01457179

Heimann, T. & Meinzer, H.-P. (2009). Statistical shape models for 3D medical image segmentation: A review. *Medical image analysis,* 13(4)**,** 543-563. https://doi.org/10.1016/j.media.2009.05.004

Hess, S. (2000). Functional stability of the glenohumeral joint. *Manual therapy,* 5(2)**,** 63-71. https://doi.org/10.1054/math.2000.0241

Hill, A., Bull, A., Wallace, A. & Johnson, G. (2008). Qualitative and quantitative descriptions of glenohumeral motion. *Gait & Posture,* 27(2)**,** 177-188. https://doi.org/10.1016/j.gaitpost.2007.04.008

Högfors, C., Karlsson, D. & Peterson, B. (1995). Structure and internal consistency of a shoulder model. *Journal of Biomechanics,* 28(7)**,** 767-777. https://doi.org/10.1016/0021-9290(94)00134-p

Huttenlocher, D. P., Klanderman, G. A. & Rucklidge, W. J. (1993). Comparing images using the Hausdorff distance. *IEEE Transactions on pattern analysis and machine intelligence,* 15(9)**,** 850-863. https://doi.org/10.1109/34.232073

Hutton, T. J., Buxton, B. F. & Hammond, P. (2001). Dense surface point distribution models of the human face. IEEE, 153. https://doi.org/10.1109/MMBIA.2001.991711

Inyang, A. O., Fouefack, J.-R., Sivarasu, S., Roche, S., BOrotikar, B., BUrdin, V. & Mutsvangwa, T. (2017). Assessment of 3D morphological characteristics of the shoulder bones using statistical shape modeling: Prospective application to handedness. *IEEE Engineering in Medicine and Biology Society (EMBC),* 1629-1632. https://doi.org/10.1109/EMBC.2017.8037151

Jeong, J.-Y., Pizer, S. M. & Ray, S. (2006). Statistics on anatomic objects reflecting inter-object relations. 1st MICCAI Workshop on Mathematical Foundations of Computational Anatomy: *Geometrical, Statistical and Registration Methods for Modeling Biological Shape Variability.* 136-145. https://hal.inria.fr/inria-00634259

Jolliffe, I. T. & Cadima, J. (2016). Principal component analysis: a review and recent developments. *Phil. Trans. R. Soc. A,* 374(2065)**,** 20150202. https://doi.org/10.1098/rsta.2015.0202

Kadavkolan, A. S. & Jawhar, A. (2018). Glenohumeral joint morphometry with reference to anatomic shoulder arthroplasty. *Current orthopaedic practice,* 29(1)**,** 71-83. https://doi.org/ 10.1097/BCO.0000000000000552

Kaganami, H. G. & Beiji, Z. (2009). Region-based segmentation versus edge detection. *IEEE Intelligent Information Hiding and Multimedia Signal Processing IIH-MSP'09,* 1217-1221. https://doi.org/10.1109/IIH-MSP.2009.13

Kainmueller, D., Lamecker, H., Zachow, S. & Hege, H.-C. (2009). An articulated statistical shape model for accurate hip joint segmentation. *IEEE* Engineering in Medicine and Biology Society (EMBC), 6345-6351. https://doi.org/10.1109/IEMBS.2009.5333269

Kainmueller, D., Lamecker, H., Zachow, S., Heller, M. & Hege, H.-C. (2008). Multi-object segmentation with coupled deformable models. *Proc. of Medical Image Understanding and Analysis,* 34-38.

Karduna, A. R., Williams, G. R., Iannotti, J. P. & Williams, J. L. (1996). Kinematics of the glenohumeral joint: influences of muscle forces, ligamentous constraints, and articular geometry. *Journal of Orthopaedic Research,* 14(6)**,** 986-993. https://doi.org/10.1002/jor.1100140620

Karelse, A., Kegels, L. & De Wilde, L. (2007). The pillars of the scapula. *Clinical Anatomy: The Official Journal of the American Association of Clinical Anatomists and the British Association of Clinical Anatomists,* 20(4)**,** 392-399. https://doi.org/10.1002/ca.20420

Krüger, J., Ehrhardt, J. & Handels, H. (2017). Statistical appearance models based on probabilistic correspondences. *Medical image analysis,* 37**,** 146-159. https://doi.org/10.1016/j.media.2017.02.004

Kumari, S. (2017). Detail and Comparative Study on Various Segmentation Techniques. *A Journal of Computer Science and Information Technology IJCSMC,* vol.6(5)**,** 308 - 315.

Ledoit, O. & Wolf, M. (2004). A well-conditioned estimator for large-dimensional covariance matrices. *Journal of multivariate analysis,* 88(2)**,** 365-411. https://doi.org/10.1016/S0047-259X(03)00096-4

Lee, Y. S. & Lee, T. Q. (2010). Specimen-specific method for quantifying glenohumeral joint kinematics. *Annals of biomedical engineering,* 38(10)**,** 3226-3236. https://doi.org/ 10.1007/s10439-010-0074-7

Lempereur, M., Leboeuf, F., Brochard, S., Rousset, J., Burdin, V. & Rémy-Néris, O. (2010). In vivo estimation of the glenohumeral joint centre by functional methods: accuracy and repeatability assessment. *Journal of biomechanics,* 43(2)**,** 370-374. https://doi.org/10.1016/j.jbiomech.2009.09.029

Levasseur, A., Tétreault, P., DE Guise, J., Nuño, N. & Hagemeister, N. (2007). The effect of axis alignment on shoulder joint kinematics analysis during arm abduction. *Clinical Biomechanics,* 22(7)**,** 758-766. https://doi.org/10.1016/j.clinbiomech.2007.04.009

Lipman, Y. & Funkhouser, T. (2009). Möbius voting for surface correspondence. *ACM Transactions on Graphics (TOG),* 28(3)**,** 72. https://doi.org/10.1145/1531326.1531378

Liu, J., Udupa, J. K., Saha, P. K., Odhner, D., Hirsch, B. E., Siegler, S., Simon, S. & Winkelstein, B. A. (2008). Rigid model-based 3D segmentation of the bones of joints in MR and CT images for motion analysis. *Medical physics,* 35(8)**,** 3637-3649. https://doi.org/10.1118/1.2953567

Lorensen, W. E. & Cline, H. E. (1987). Marching cubes: A high resolution 3D surface construction algorithm. *ACM siggraph computer graphics,* 21**,** 163-169. https://doi.org/10.1145/37402.37422

Lorenz, C. & Krahnstöver, N. (2000). Generation of point-based 3D statistical shape models for anatomical objects. *Computer vision and image understanding,* 77(2)**,** 175-191. https://doi.org/10.1006/cviu.1999.0814

Lugo, R., Kung, P. & Ma, C. B. (2008). Shoulder biomechanics. *European journal of radiology,* 68(1)**,** 16-24. https://doi.org/10.1016/j.ejrad.2008.02.051

Lüthi, M., Gerig, T., Jud, C. & Vetter, T. (2018). Gaussian process morphable models. *IEEE transactions on pattern analysis and machine intelligence,* 40(8)**,** 1860-1873. https://doi.org/10.1109/TPAMI.2017.2739743

Lynch, E., Lombard, A. J., Coopoo, Y., Shaw, I. & Shaw, B. S. (2013). Shoulder injury incidence and severity through identification of risk factors in rugby union players. *Pakistan journal of medical sciences,* 29(6)**,** 1400. https://dx.doi.org/10.1269/pjms.296.3769

Marin, F., Mannel, H., Claes, L. & Dürselen, L. (2003). Correction of axis misalignment in the analysis of knee rotations. *Human movement science,* 22(3)**,** 285-296. https://doi.org/10.1016/S0167-9457(03)00036-8

Massimini, D. F., Warner, J. J. & Li, G. (2011). Non-invasive determination of coupled motion of the scapula and humerus—an in-vitro validation. *Journal of biomechanics,* 44(3)**,** 408-412. https://doi.org/10.1016/j.jbiomech.2010.10.003

Mcminn, R. M. H. (2005). *Last's Anatomy: regional and applied. Ninth eddition,* Edinburgh ; New York : Churchill Livingstone. available: https://books.google.co.za/books?hl=en&lr=&id=4ihGmxzamekC&oi=fnd&pg=PP1&dq=Mcminn,+R.+M.+H.+(2005).+Last%27s+Anatomy:+regional+and+applied.+Ninth+eddition,+Edinburgh+%3B+New+York+:+Churchill+Livingstone.&ots=L1BghHRHDY&sig=8pbi4qAjcH5STorgVywpFt2Zx2c#v=onepage&q&f=false

Meskers, C., Van Der Helm, F. C., Rozendaal, L. & Rozing, P. (1997). In vivo estimation of the glenohumeral joint rotation center from scapular bony landmarks by linear regression. *Journal of biomechanics,* 31(1)**,** 93-96. https://doi.org/10.1016/S0021-9290(97)00101-2

Meskers, C. G., Van De Sande, M. A. & De Groot, J. H. (2007). Comparison between tripod and skin-fixed recording of scapular motion. *Journal of Biomechanics,* 40(4)**,** 941-946. https://doi.org/10.1016/j.jbiomech.2006.02.011

Moore, K. L., Dalley, A. F. & Agur, A. M. (2013). *Clinically oriented anatomy,* Lippincott Williams & Wilkins. *Seventh eddition,* Philadelphia. Available: https://books.google.co.za/books?hl=en&lr=&id=-Le5bc5F0sYC&oi=fnd&pg=PP2&dq=Moore,+K.+L.,+Dalley,+A.+F.+%26+Agur,+A.+M.+(2013).+Clinically+oriented+anatomy,+Lippincott+Williams+%26+Wilkins.+Seventh+eddition,+Philadelphia.&ots=jLAoO_frBG&sig=E27hajmyBAgOQZmg4jXg_ob1EyE#v=onepage&q&f=false

Mutsvangwa, T., Burdin, V., Borotikar, B. & Roux, C. (2014). An automated statistical shape model developmental pipeline: implications to shoulder surgery parameter. SHAPE

2014: *symposium on Statistical Shape Models & Application*s. https://hal.archives-ouvertes.fr/hal-01056659

Mutsvangwa, T., Burdin, V., Schwartz, C. & Roux, C. (2015). An automated statistical shape model developmental pipeline: application to the human scapula and humerus. *IEEE Transactions on Biomedical Engineering,* 62(4)**,** 1098-1107. https://doi.org/10.1109/TBME.2014.2368362

Mutsvangwa, T. E., Veeraragoo, M. & Douglas, T. S. (2011). Precision assessment of stereo-photogrammetrically derived facial landmarks in infants. *Annals of Anatomy-Anatomischer Anzeiger,* 193(2)**,** 100-105. https://doi.org/10.1016/j.aanat.2010.10.008

Myronenko, A., Song, X. & Carreira-Perpinán, M. A. (2007). Non-rigid point set registration: Coherent point drift. *Advances in Neural Information Processing Systems*. 1009-1016. Retrieved from http://papers.nips.cc/paper/2962-non-rigid-point-set-registration-coherent-point-drift.pdf

NGUYEN, N. T., LAURENDEAU, D. & BRANZAN-ALBU, A. A new segmentation method for MRI images of the shoulder joint. Computer and Robot Vision, 2007. CRV'07. Fourth Canadian Conference on, 2007. IEEE, 329-338.

Nguyen, N. T., Laurendeau, D. & Branzan-Albu, A. (2007). A new segmentation method for MRI images of the shoulder joint. *IEEE Computer and Robot Vision CRV'07,* 329-338. https://doi.org/10.1109/CRV.2007.4

Ning, J., Zhang, L., Zhang, D. & WU, C. (2010). Interactive image segmentation by maximal similarity based region merging. *Pattern Recognition,* 43(2)**,** 445-456. https://doi.org/10.1016/j.patcog.2009.03.004

Oliveira, F. P. & Tavares, J. M. R. (2014). Medical image registration: a review. *Computer methods in biomechanics and biomedical engineering,* 17(2)**,** 73-93. https://doi.org/10.1080/10255842.2012.670855

Owaydhah, W. H., Alobaidy, M. A., Alraddadi, A. S. & Soames, R. W. (2017). Three-dimensional analysis of the proximal humeral and glenoid geometry using MicroScribe 3D digitizer. *Surgical and Radiologic Anatomy,* 39(7)**,** 767-772. https://doi.org/10.1007/s00276-016-1782-y

Phadke, V., Braman, J. P., Laprade, R. F. & Ludewig, P. M. (2011). Comparison of glenohumeral motion using different rotation sequences. *Journal of biomechanics,* 44(4)**,** 700-705. https://doi.org/10.1016/j.jbiomech.2010.10.042

Pham, D. L., Xu, C. & Prince, J. L. (2000). Current methods in medical image segmentation. *Annual review of biomedical engineering,* 2(1)**,** 315-337. https://doi.org/10.1146/annurev.bioeng.2.1.315

Piazza, S. J. & Cavanagh, P. R. (2000). Measurement of the screw-home motion of the knee is sensitive to errors in axis alignment. *Journal of biomechanics,* 33(8)**,** 1029-1034. https://doi.org/10.1016/S0021-9290(00)00056-7

Pizer, S. M., Fritsch, D. S., Yushkevich, P. A., Johnson, V. E. & Chaney, E. L. (1999). Segmentation, registration, and measurement of shape variation via image object shape.

IEEE Transactions on Medical Imaging, 18(10)**,** 851-865. https://doi.org/10.1109/42.811263

Pizer, S. M., Jeong, J.-Y., LU, C., Muller, K. & Joshi, S. (2005). Estimating the statistics of multi-object anatomic geometry using inter-object relationships. *Deep Structure, Singularities, and Computer Vision.* Springer. https://doi.org/10.1007/11577812_6

Poltaretskyi, S., Chaoui, J., Mayya, M., Hamitouche, C., Bercik, M., Boileau, P. & Walch, G. (2017). Prediction of the pre-morbid 3D anatomy of the proximal humerus based on statistical shape modelling. *Bone Joint J,* 99(7)**,** 927-933. https://doi.org/10.1302/0301-620X.99B7.BJJ-2017-0014RACHAKONDA, P., MURALIKRISHNAN, B., COURNOYER, L., CHEOK, G., LEE, V., SHILLING, M. & SAWYER, D. 2017. Methods and considerations to determine sphere center from terrestrial laser scanner point cloud data. *Measurement Science and Technology,* 28**,** 105001.

Rachakonda, P., Muralikrishnan, B., Cournoyer, L., Cheok, G., Lee, V., Shilling, M. & Sawyer, D. (2017). Methods and considerations to determine sphere center from terrestrial laser scanner point cloud data. *Measurement Science and Technology,* 28(10)**,** 105001. https://doi.org/10.1088/1361-6501/aa8011

Rasmussen, C. E. (2006). Advances in Gaussian processes. *Advances in Neural Information Processing Systems,* 19. Available: https://www.lri.fr/~sebag/COURS/gpnt06.pdf

Roberts, M. G., Cootes, T. F. & Adams, J. E. (2005). Vertebral shape: automatic measurement with dynamically sequenced active appearance models. *International Conference on Medical Image Computing and Computer-Assisted Intervention*. Springer, 733-740. https://doi.org/10.1007/11566489_90

Rundquist, P. J. & Ludewig, P. M. (2004). Patterns of motion loss in subjects with idiopathic loss of shoulder range of motion. *Clinical biomechanics,* 19(8)**,** 810-818. https://doi.org/10.1016/j.clinbiomech.2004.05.006

Sarkalkan, N., Weinans, H. & Zadpoor, A. (2014). Statistical shape and appearance models of bones. *Bone,* 60**,** 129-140. https://doi.org/10.1016/j.bone.2013.12.006

Schmid, J., Kim, J. & Magnenat-Thalmann, N. (2011). Robust statistical shape models for MRI bone segmentation in presence of small field of view. *Medical image analysis,* 15**,** 155-168. https://doi.org/10.1016/j.media.2010.09.001

Sclaroff, S. & Pentland, A. P. (1995). Modal matching for correspondence and recognition. *IEEE Transactions on Pattern Analysis and Machine Intelligence,* 17(6)**,** 545-561. https://doi.org/10.1109/34.387502

Semechko, A. (2011). Development of a Multi-body Statistical Shape Model of the Wrist. *Ph.D. Thesis. University of Guelph.* Available: *http://hdl.handle.net/10214/3208*

Šenk, M. & Chèze, L. (2006). Rotation sequence as an important factor in shoulder kinematics. *Clinical biomechanics,* 21**,** S3-S8. https://doi.org/10.1016/j.clinbiomech.2005.09.007

Sharma, N., Mishra, M. & Shrivastava, M. (2012). Colour image segmentation techniques and issues: an approach. *International Journal of Scientific & Technology Research,* 1(4)**,** 9-12. Available: http://www.ijstr.org/paper-references.php?ref=IJSTR-0312-5019

Sinclair, J., Taylor, P. J., Edmundson, C. J., Brooks, D. & Hobbs, S. J. (2012). Influence of the helical and six available Cardan sequences on 3D ankle joint kinematic parameters. *Sports Biomechanics,* 11(3)**,** 430-437. https://doi.org/10.1080/14763141.2012.656762

Smoger, L. M., Fitzpatrick, C. K., Clary, C. W., Cyr, A. J., Maletsky, L. P., Rullkoetter, P. J. & Laz, P. J. (2015). Statistical modeling to characterize relationships between knee anatomy and kinematics. *Journal of Orthopaedic Research,* 33(11)**,** 1620-1630. https://doi.org/10.1002/jor.22948

Stegmann, M. B. & Gomez, D. D. (2002). A brief introduction to statistical shape analysis. *Informatics and mathematical modelling, Technical University of Denmark, DTU,* 15(11). Available: https://pdfs.semanticscholar.org/a704/6c9ad9b63e00dd4ff93cb26b2ffab8e55bbe.pdf

Stokdijk, M., Nagels, J. & Rozing, P. (2000). The glenohumeral joint rotation centre in vivo. *Journal of Biomechanics,* 33(12)**,** 1629-1636. https://doi.org/10.1016/S0021-9290(00)00121-4

Styner, M., Gorczowski, K., Fletcher, T., Jeong, J. Y., Pizer, S. M. & Gerig, G. (2006). Statistics of pose and shape in multi-object complexes using principal geodesic analysis. *International Workshop on Medical Imaging and Virtual Reality*. Springer, 1-8. https://doi.org/10.1007/11812715_1

Styner, M. A., Rajamani, K. T., Nolte, L.-P., Zsemlye, G., Székely, G., Taylor, C. J. & Davies, R. H. (2003). Evaluation of 3D correspondence methods for model building. *Biennial International Conference on Information Processing in Medical Imaging, 2003*. Springer, 63-75. https://doi.org/10.1007/978-3-540-45087-0_6

Swamy, M. M. & Holi, M. S. (2012). Knee joint articular cartilage segmentation, visualization and quantification using image processing techniques: a review. *Knee,* 42(19). https://doi.org/10.5120/5803-8151

Tejos, C., IrarrazavaL, P. & Cárdenas-blanco, A. (2009). Simplex mesh diffusion snakes: integrating 2D and 3D deformable models and statistical shape knowledge in a variational framework. *International journal of computer vision,* 85**,** 19-34. https://doi.org/10.1007/s11263-009-0241-1

Terry, G. C. & Chopp, T. M. (2000). Functional anatomy of the shoulder. *Journal of athletic training,* 35(3)**,** 248. Available: https://www.ncbi.nlm.nih.gov/pmc/articles/PMC1323385/

Tsai, A., Wells, W., Tempany, C., Grimson, E. & Willsky, A. (2004). Mutual information in coupled multi-shape model for medical image segmentation. *Medical image analysis,* 8(4)**,** 429-445. https://doi.org/10.1016/j.media.2004.01.003

Valstar, E. R., Botha, C. P., Van der Glas, M., Rozing, P. M., Van Der Helm, F. C., Post, F. H. & Vossepoel, A. M. (2002). Towards computer-assisted surgery in shoulder joint replacement. *ISPRS journal of photogrammetry and remote sensing,* 56(5)**,** 326-337. https://doi.org/10.1016/S0924-2716(02)00067-9

Van De Giessen, M., Streekstra, G. J., Strackee, S. D., Maas, M., Grimbergen, K. A., Van Vliet, L. J. & Vos, F. M. (2009). Constrained registration of the wrist joint. *IEEE*

Transactions on Medical Imaging, 28(12)**,** 1861-1869. https://doi.org/10.1109/TMI.2009.2021432

Van De Giessen, M., Vos, F., Strackee, S. D., Maas, M., Grimbergen, C. A., Van Vliet, L. J. & Streekstra, G. J. (2007). Constrained registration of multiple rigid objects in close proximity: application in the wrist joint. *IEEE Biomedical Imaging: From Nano to Macro. ISBI*, 704-707. https://doi.org/10.1109/ISBI.2007.356949

Van Der Heijden, G. J. (1999). Shoulder disorders: a state-of-the-art review. *Best Practice & Research Clinical Rheumatology,* 13(2)**,** 287-309. https://doi.org/10.1053/berh.1999.0021

Van Der Heijden, G. J. (1999). Shoulder disorders: a state-of-the-art review. *Best Practice & Research Clinical Rheumatology,* 13(2)**,** 287-309. https://doi.org/10.1053/berh.1999.0021

Van Kaick, O., Zhang, H., Hamarneh, G. & Cohen-Or, D. (2011). A survey on shape correspondence. *Computer Graphics Forum*. Wiley Online Library, 1681-1707. https://doi.org/10.1111/j.1467-8659.2011.01884.x

Weinberg, S. M., Scott, N. M., Neiswanger, K., Brandon, C. A. & Marazita, M. L. (2004). Digital three-dimensional photogrammetry: evaluation of anthropometric precision and accuracy using a Genex 3D camera system. *The Cleft palate-craniofacial journal,* 41**,** 507-518. https://doi.org/10.1597/03-066.1

Williams, T. G., Taylor, C. J., Gao, Z. & Waterton, J. C. (2003). Corresponding articular cartilage thickness measurements in the knee joint by modelling the underlying bone. *International Conference on Medical Image Computing and Computer-Assisted*. Springer, 480-487. https://doi.org/10.1007/978-3-540-39903-2_59

Woltring, H., Huiskes, R., De Lange, A. & Veldpaus, F. (1985). Finite centroid and helical axis estimation from noisy landmark measurements in the study of human joint kinematics. *Journal of biomechanics,* 18(5)**,** 379-389. https://doi.org/10.1016/0021-9290(85)90293-3

Wu, G., Van Der Helm, F. C., Veeger, H. D., Makhsous, M., Van Roy, P., Anglin, C., Nagels, J., Karduna, A. R., Mcquade, K. & Wang, X. (2005). ISB recommendation on definitions of joint coordinate systems of various joints for the reporting of human joint motion—Part II: shoulder, elbow, wrist and hand. *Journal of biomechanics,* 38(5)**,** 981-992. https://doi.org/10.1016/j.jbiomech.2004.05.042

Xia, Y., Chandra, S. S., Engstrom, C., Strudwick, M. W., Crozier, S. & Fripp, J. (2014). Automatic hip cartilage segmentation from 3D MR images using arc-weighted graph searching. *Physics in Medicine & Biology,* 59(23)**,** 7245. https://doi.org/10.1088/0031-9155/59/23/7245

Yang, J., Staib, L. H. & Duncan, J. S. (2004). Neighbor-constrained segmentation with level set based 3-D deformable models. *IEEE Transactions on Medical Imaging,* 23(8)**,** 940-948. https://doi.org/10.1109/TMI.2004.830802

Yang, Y. M., Rueckert, D. & BulL, A. M. (2008). Predicting the shapes of bones at a joint: application to the shoulder. *Computer Methods in Biomechanics and Biomedical Engineering,* 11(1)**,** 19-30. https://doi.org/10.1080/10255840701552721

Yang, Z., Fripp, J., Chandra, S. S., Neubert, A., Xia, Y., Strudwick, M., Paproki, A., Engstrom, C. & Crozier, S. (2015). Automatic bone segmentation and bone-cartilage interface extraction for the shoulder joint from magnetic resonance images. *Physics in medicine and biology,* 60(4)**,** 1441. https://doi.org/10.1088/0031-9155/60/4/1441

Yogamangalam, R. & Karthikeyan, B. (2013). Segmentation techniques comparison in image processing. *International Journal of Engineering and Technology (IJET),* 5**,** 307-313.

Zeng, Y., Wang, C., Wang, Y., Gu, X., Samaras, D. & Paragios, N. (2010). Dense non-rigid surface registration using high-order graph matching. *Computer Vision and Pattern Recognition (CVPR)*. IEEE, 382-389. https://doi.org/10.1109/CVPR.2010.5540189

Zhu, Z., Massimini, D. F., Wang, G., Warner, J. J. & LI, G. (2012). The accuracy and repeatability of an automatic 2D–3D fluoroscopic image-model registration technique for determining shoulder joint kinematics. *Medical engineering & physics,* 34(9)**,** 1303-1309. https://doi.org/10.1016/j.medengphy.2011.12.021

APPENDIX A: FULL LIST OF VALIDATION RESULTS

Remark: The red and indigo arrows point the smallest surface-to-surface distance error of the humerus and the scapula, respectively. The black arrow indicates the smallest pose error obtained between the model and the shape and pose instances generated.

A.1. Abduction motion validation results

Specificity

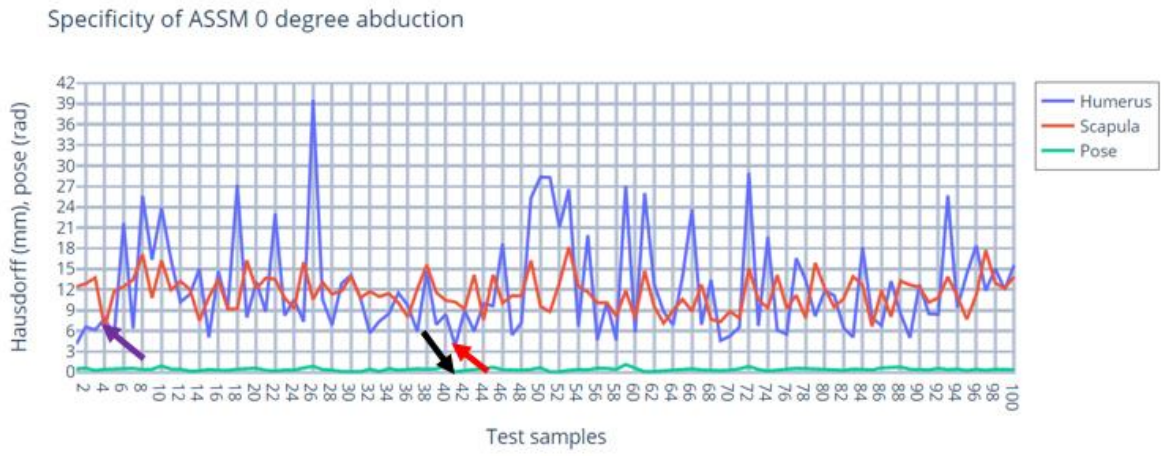

Figure A.1. Specificity of ASSM for 0^0 abduction.

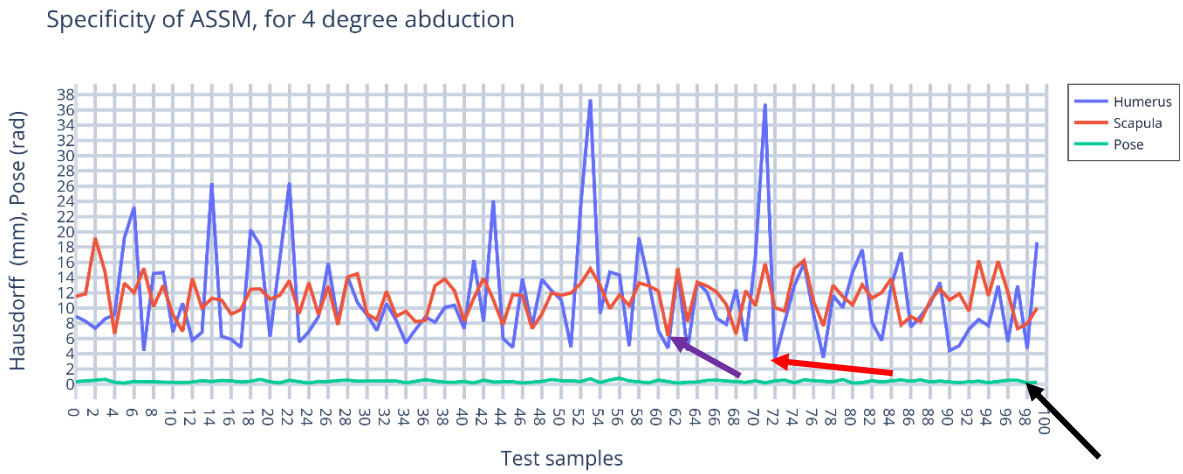

Figure A.2. Specificity of ASSM for 4^0 abduction.

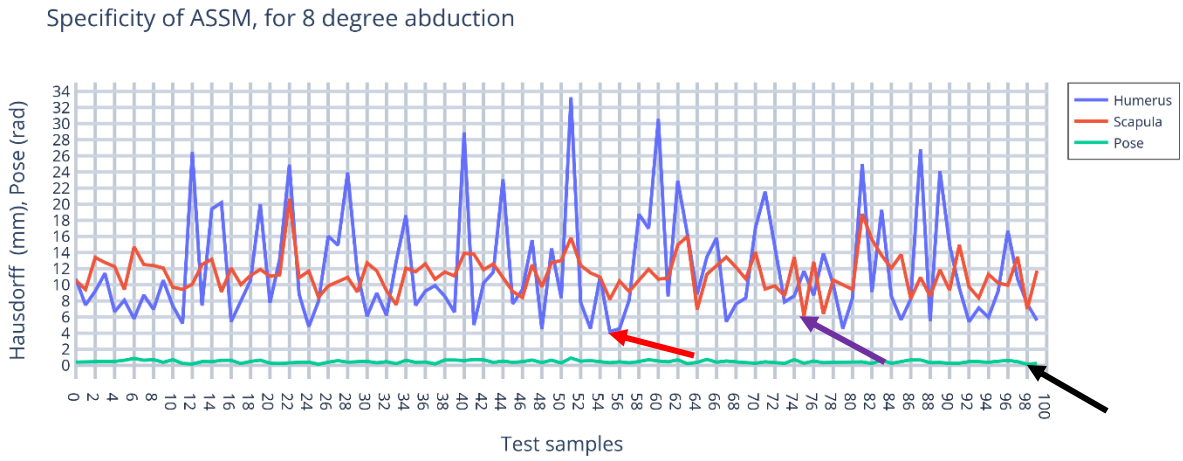

Figure A.3. Specificity of ASSM for 8^0 abduction.

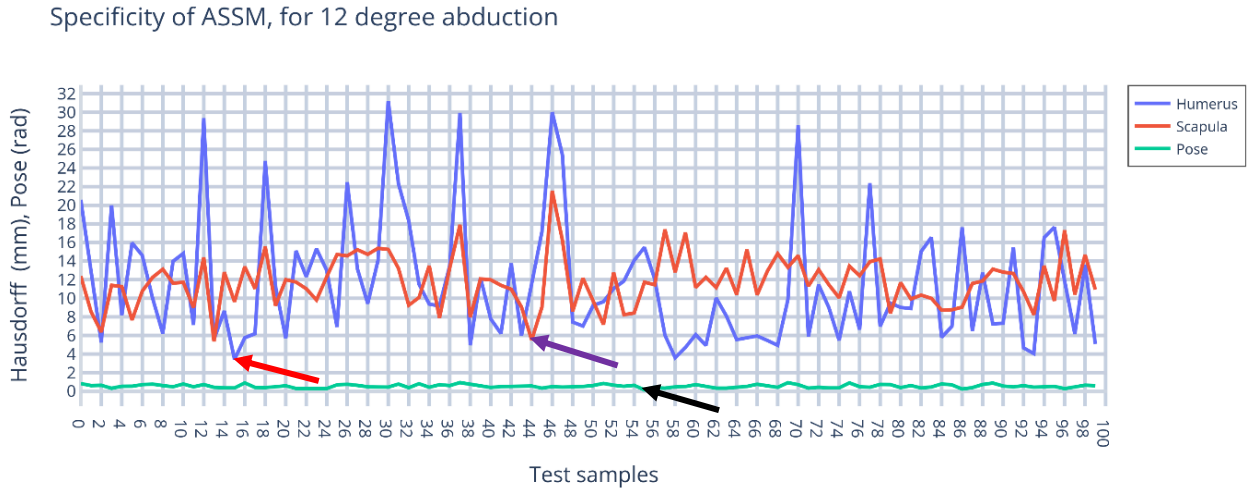

Figure A.4. Specificity of ASSM for 12^0 abduction.

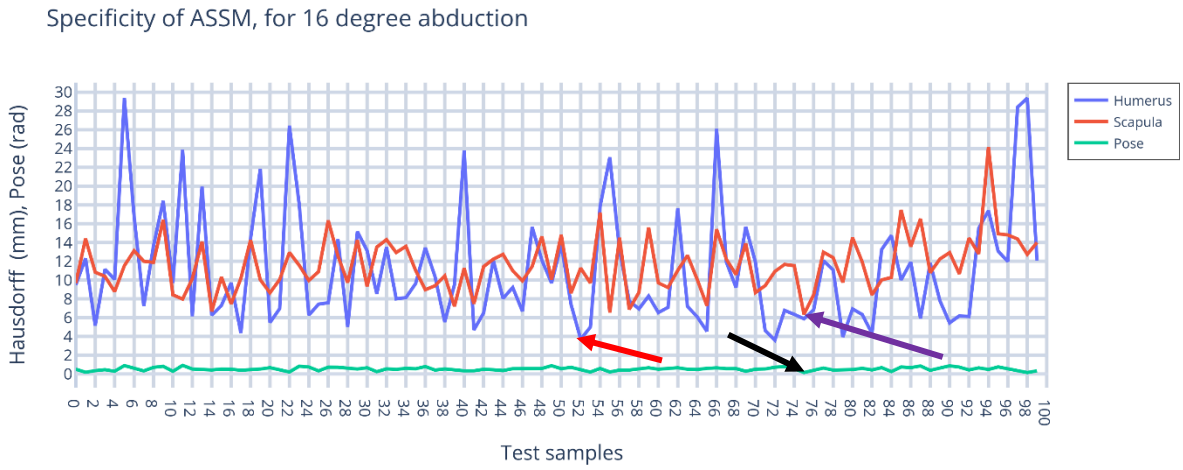

Figure A.5. Specificity of ASSM for 16^0 abduction.

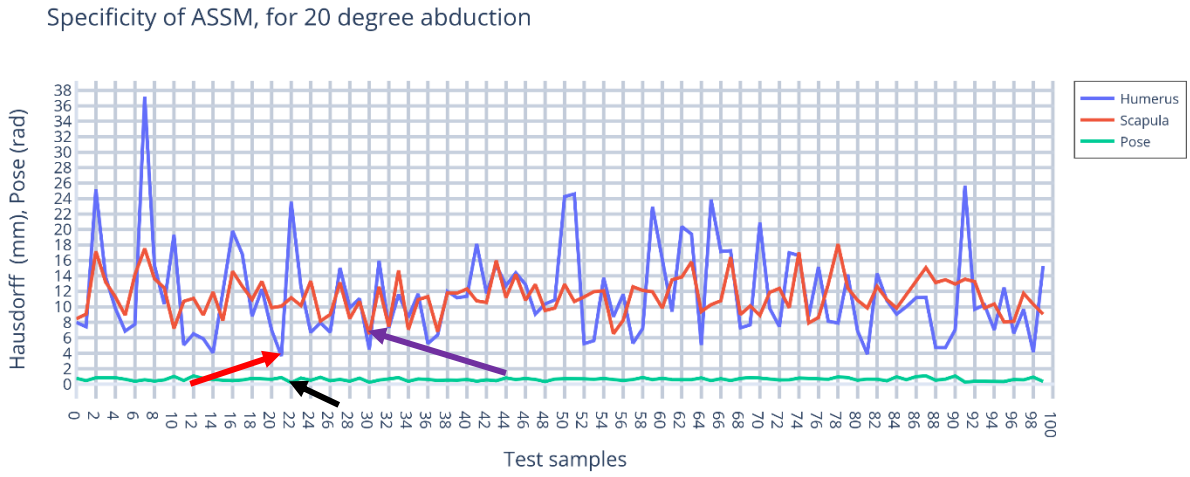

Figure A.6. Specificity of ASSM for 20^0 abduction.

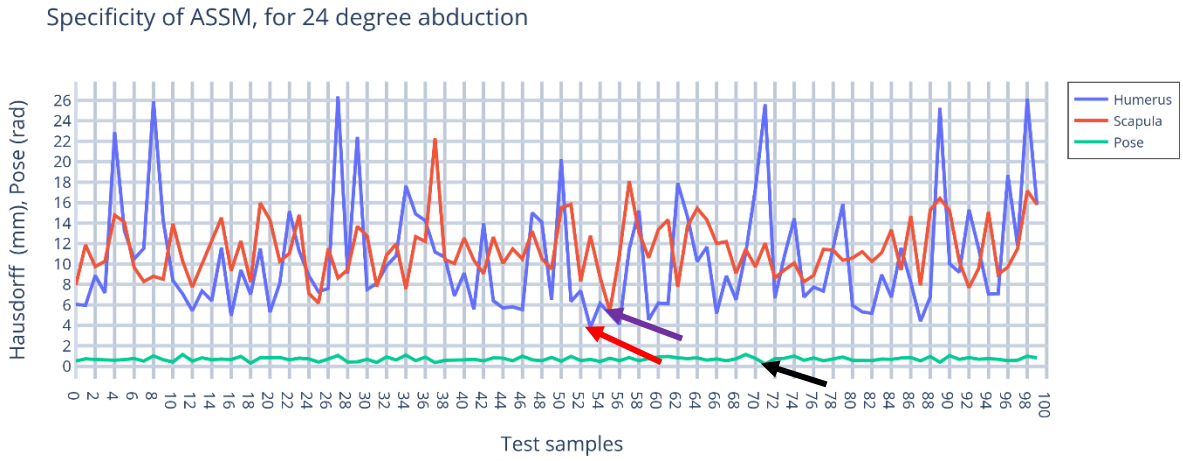

Figure A.7. Specificity of ASSM for 24^0 abduction.

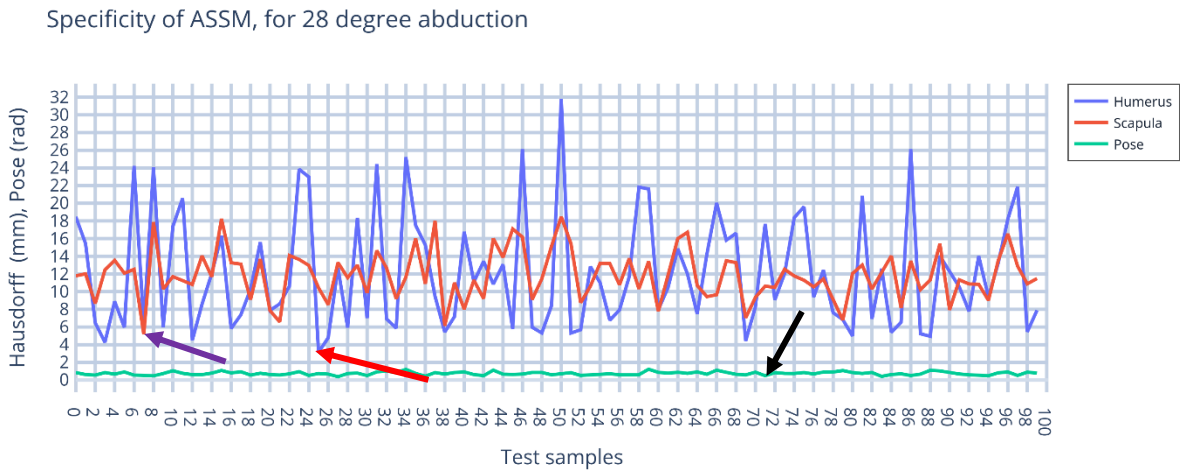

Figure A.8. Specificity of ASSM for 28^0 abduction

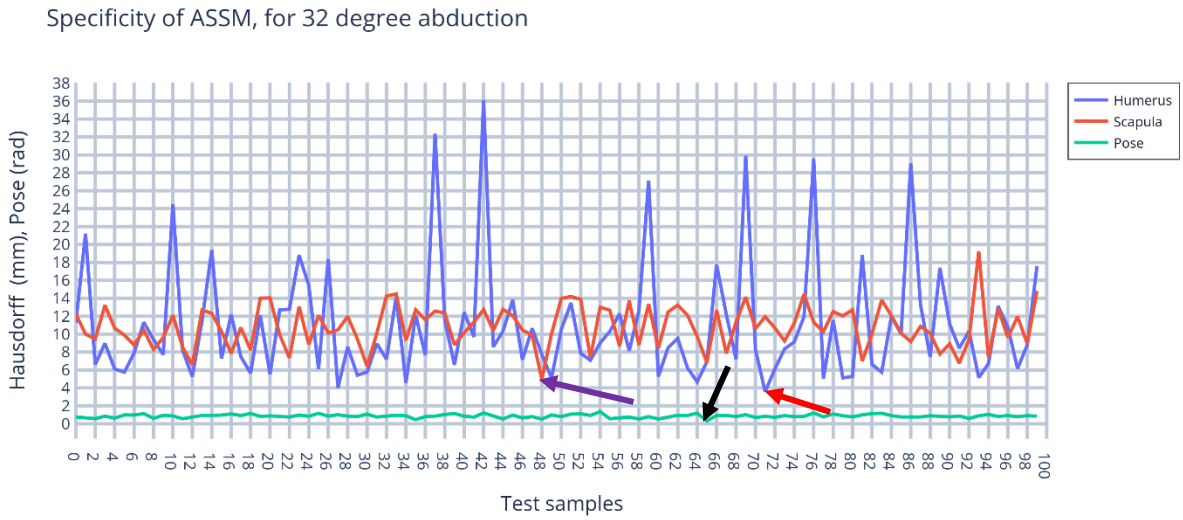

Figure A.9. Specificity of ASSM for 32^0 abduction

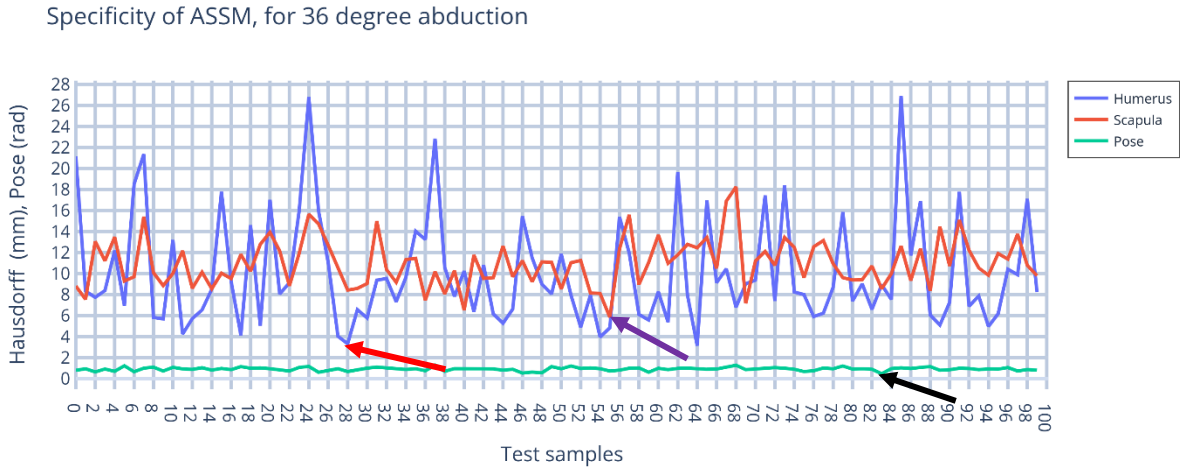

Figure A.10. Specificity of ASSM for 36^0 abduction

Generality

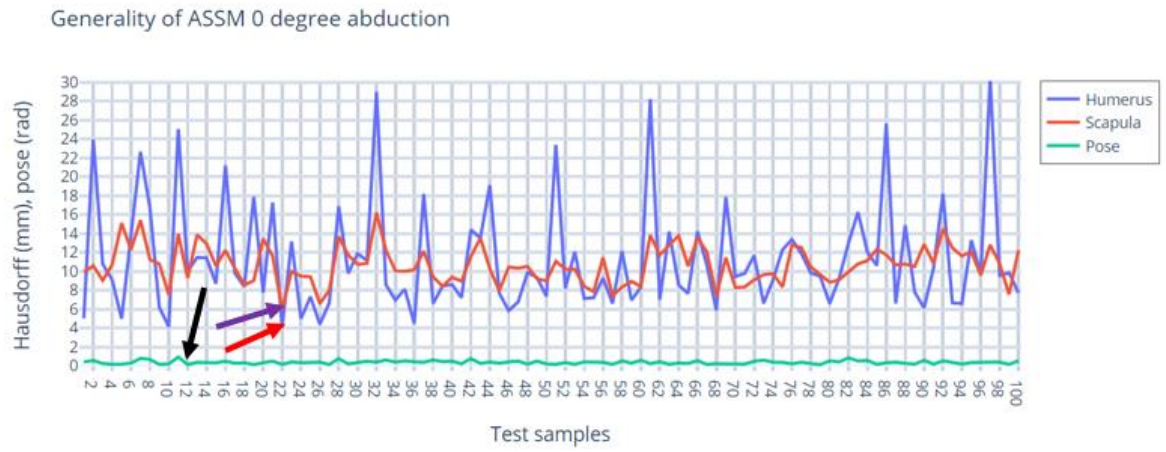

Figure A.11. Generality of ASSM for 0^0 abduction

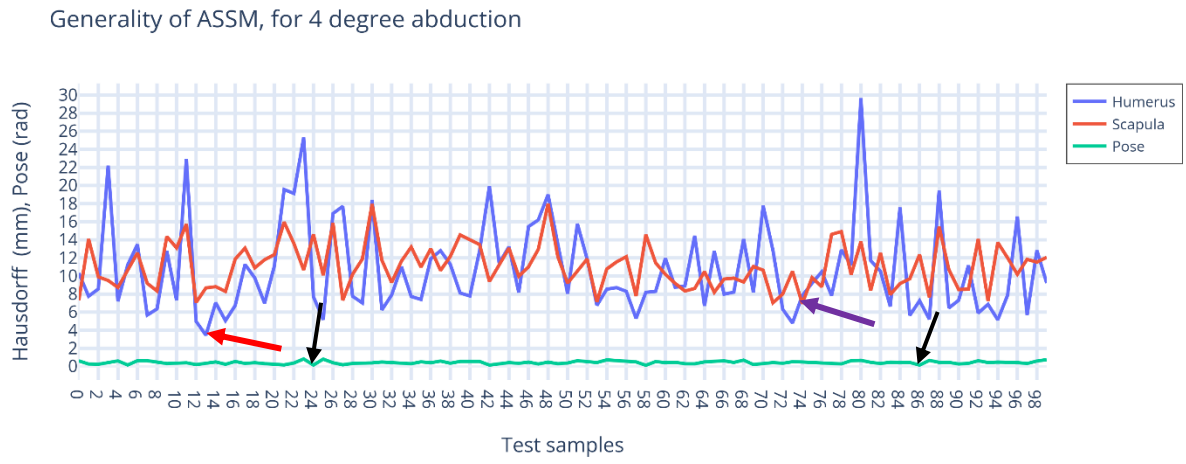

Figure A.12. Generality of ASSM for 4^0 abduction

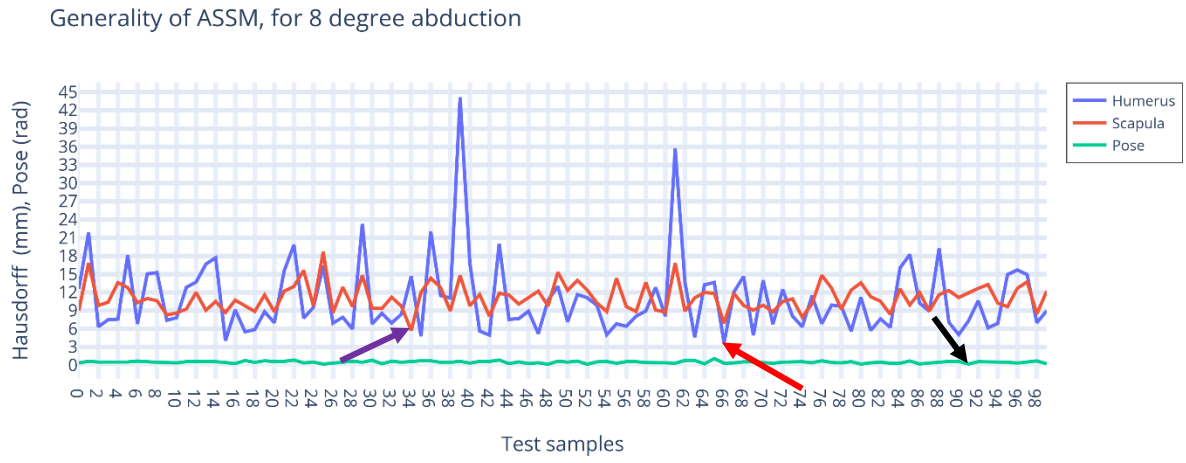

Figure A.13. Generality of ASSM for 8^0 abduction

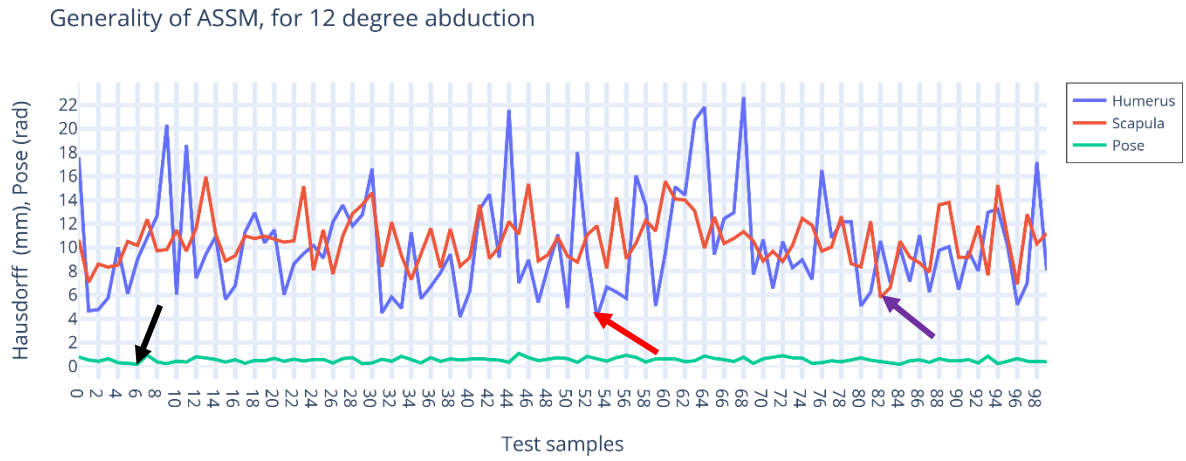

Figure A.14. Generality of ASSM for 12^0abduction

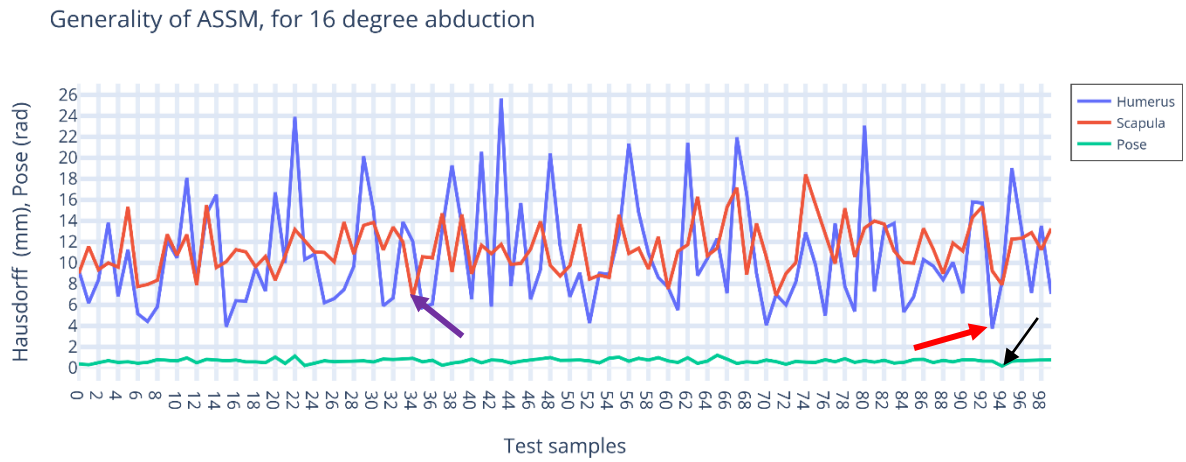

Figure A.15. Generality of ASSM for 16^0 abduction

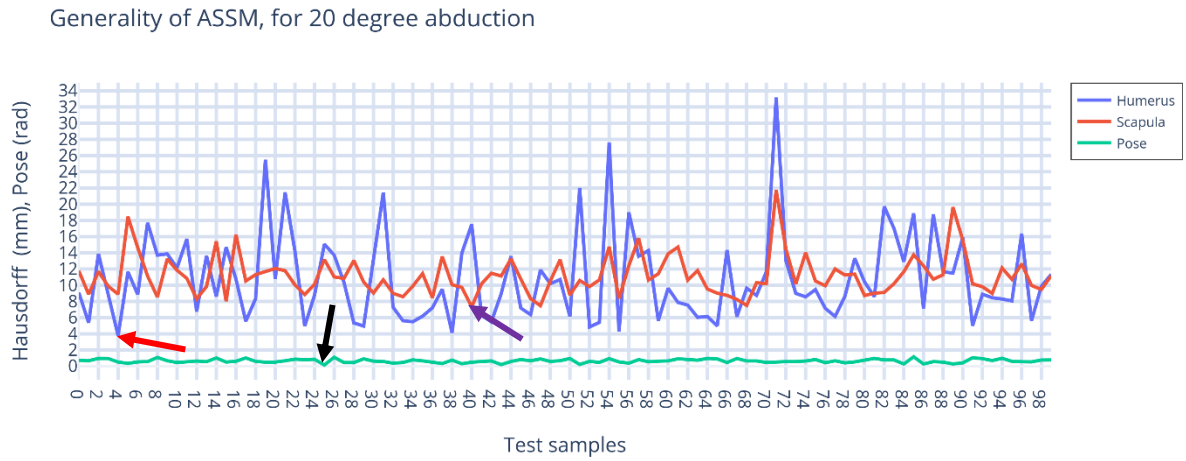

Figure A.16. Generality of ASSM for 20^0 abduction

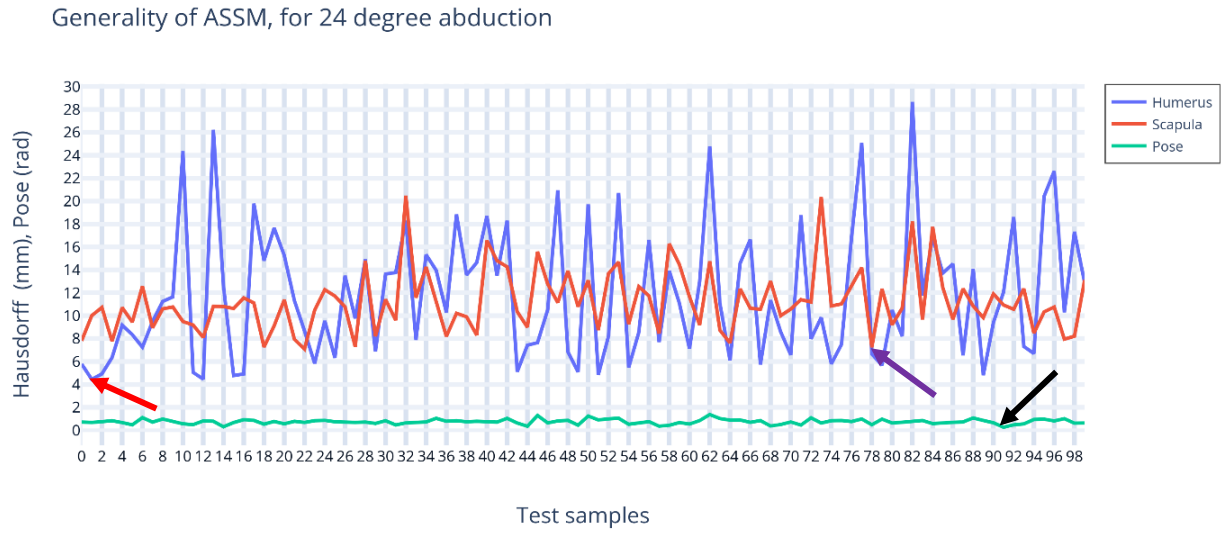

Figure A.17. Generality of ASSM for 24^0abduction

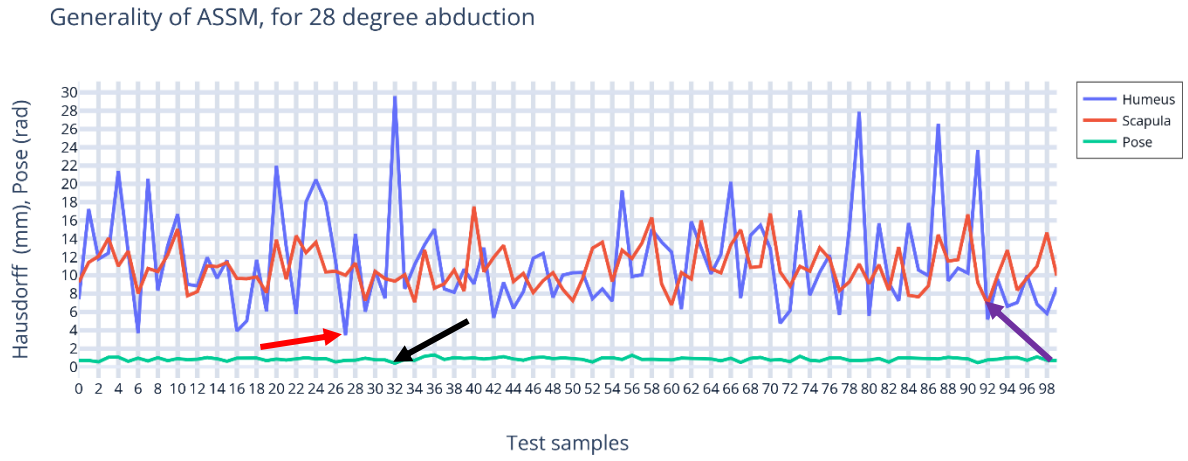

Figure A.18. Generality of ASSM for 28^0 abduction

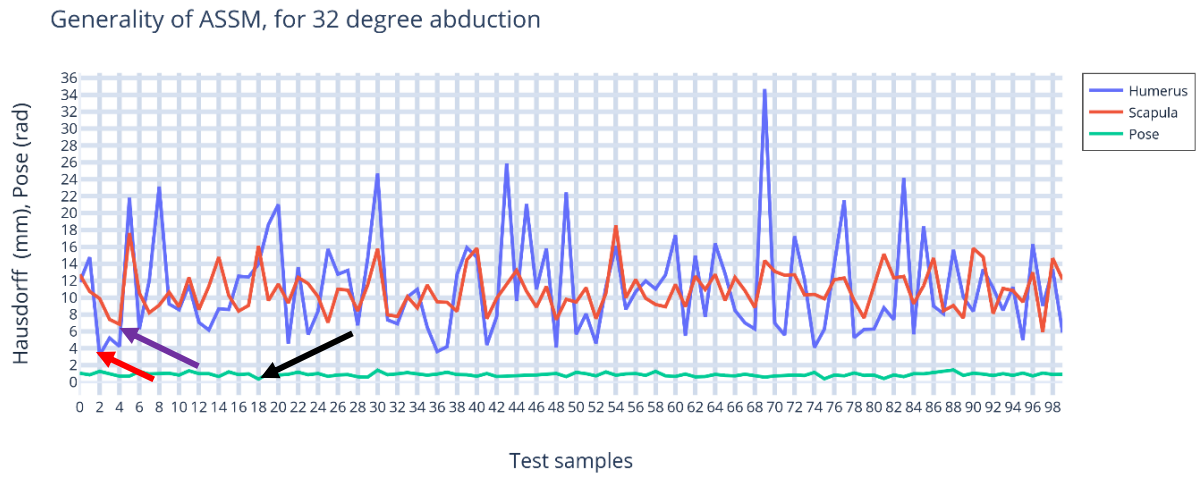

Figure A.19. Generality of ASSM for 32^0 abduction

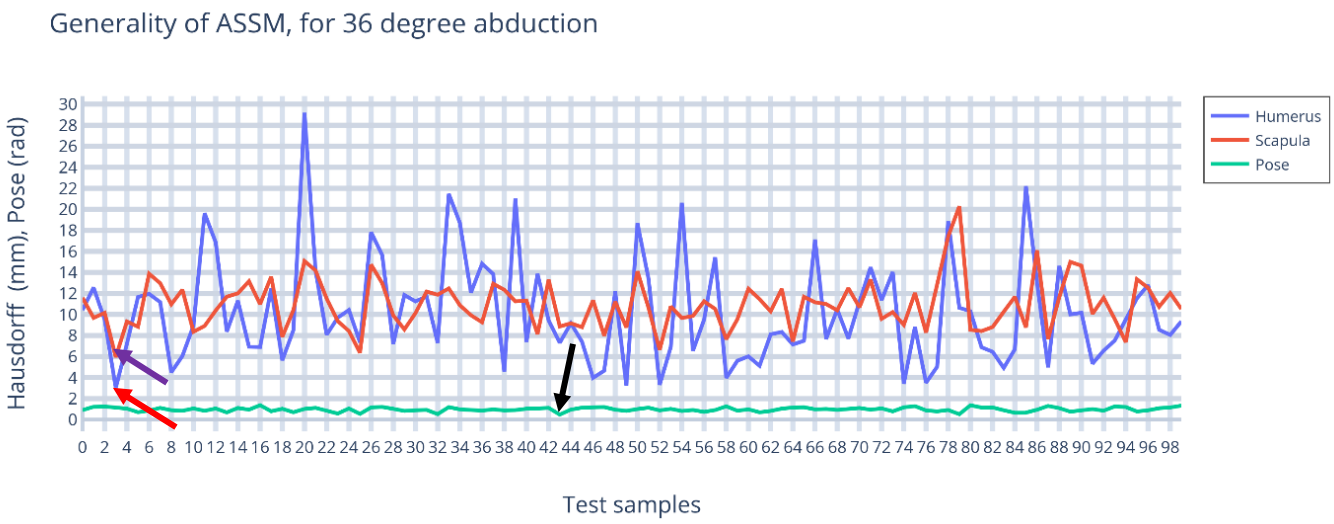

Figure A.20. Generality of ASSM for 36^0 abduction

A.2. Flexion motion validation results

Specificity

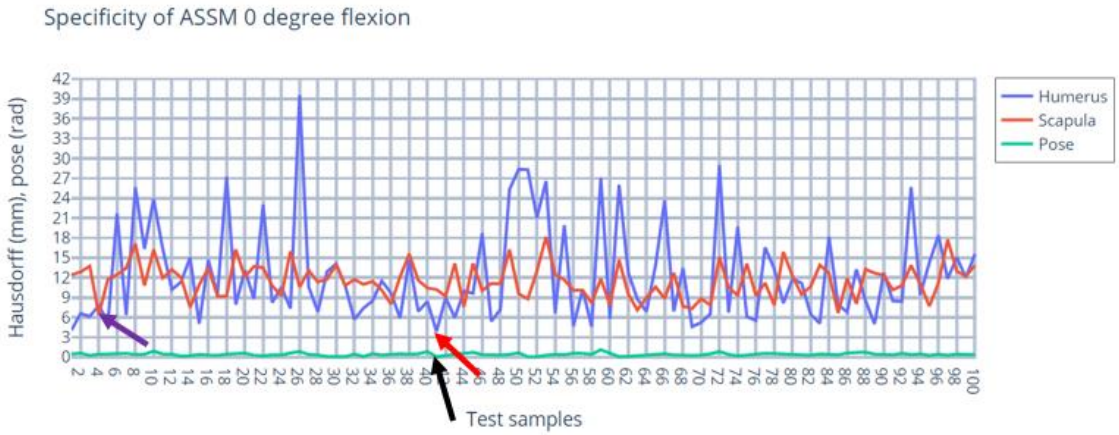

Figure A.21. Specificity of ASSM for 0^0 flexion

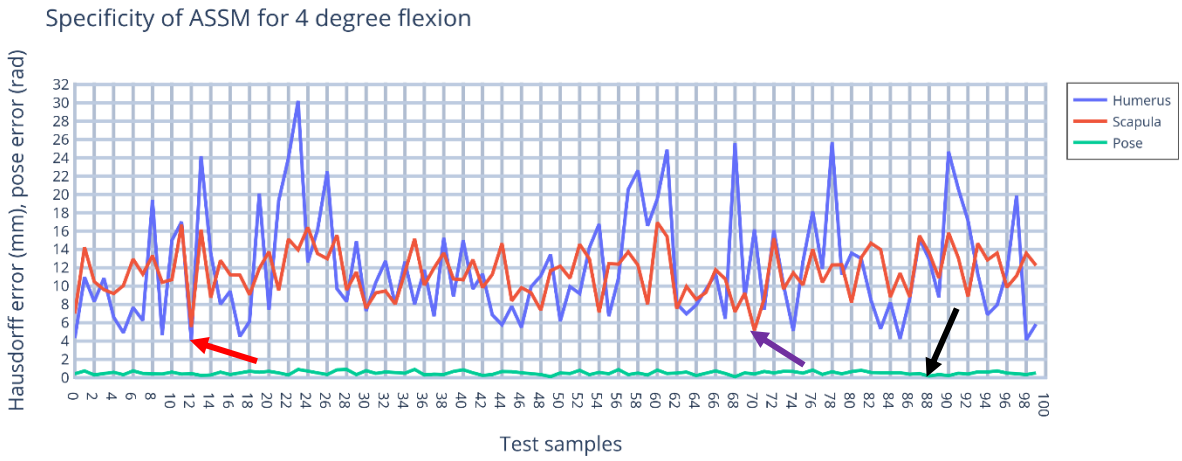

Figure A.22. Specificity of ASSM for 4^0 flexion

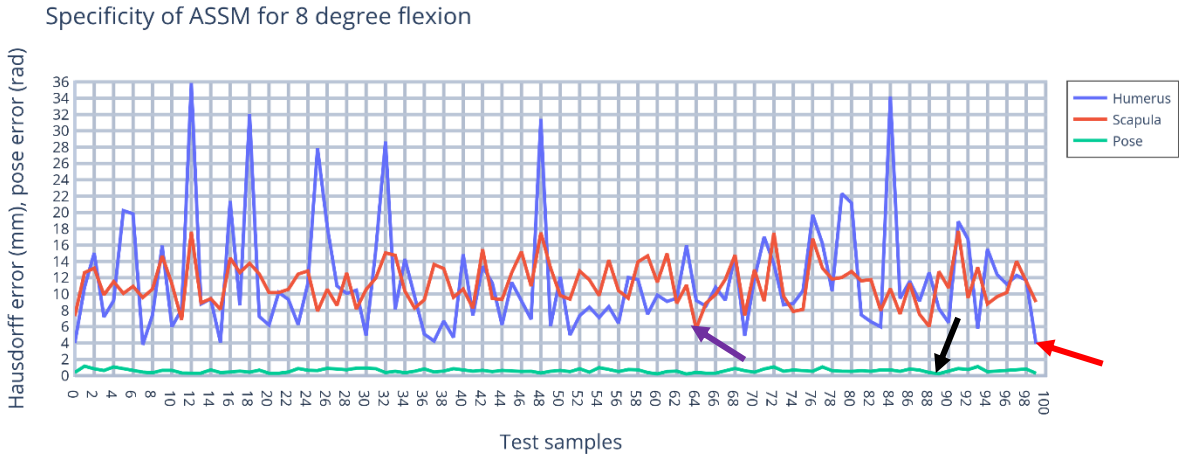

Figure A.23. Specificity of ASSM for 8^0 flexion

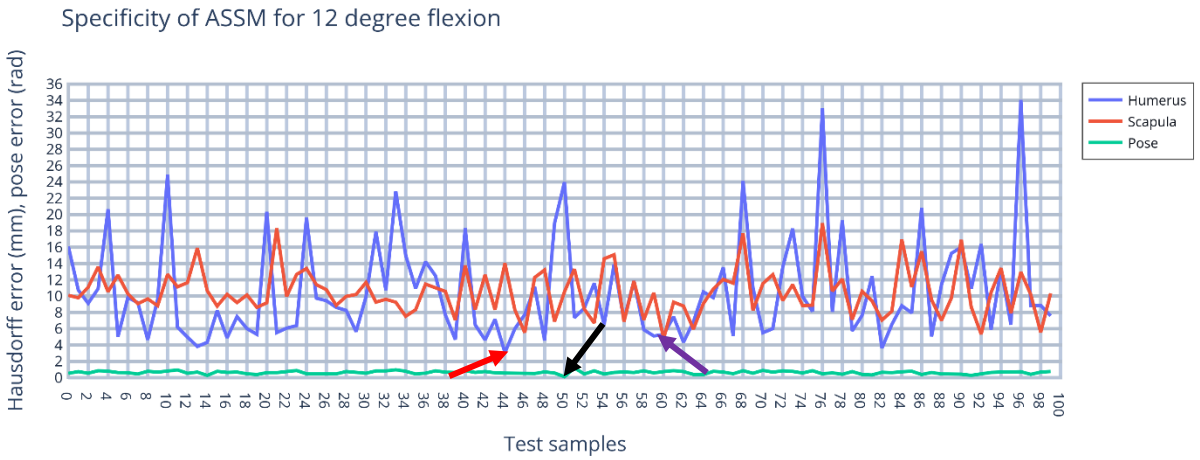

Figure A.24. Specificity of ASSM for 12^0 flexion

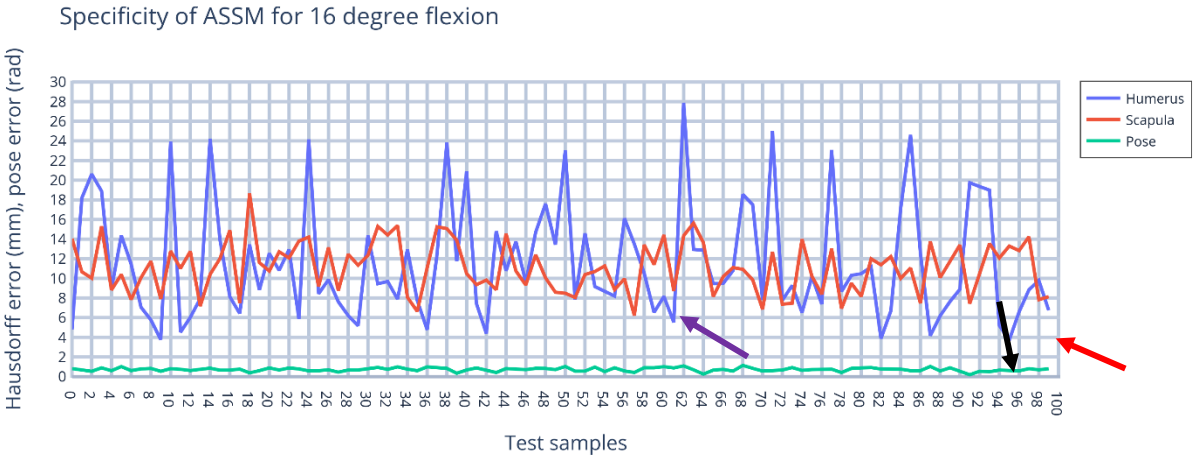

Figure A.25. Specificity of ASSM for 16^0 flexion

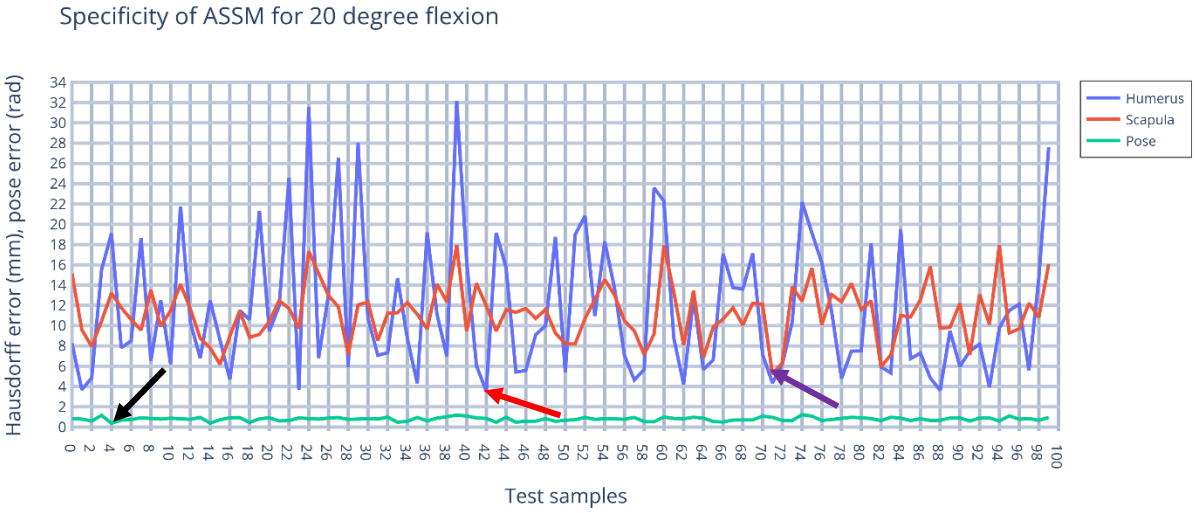

Figure A.26. Specificity of ASSM for 20^0 flexion

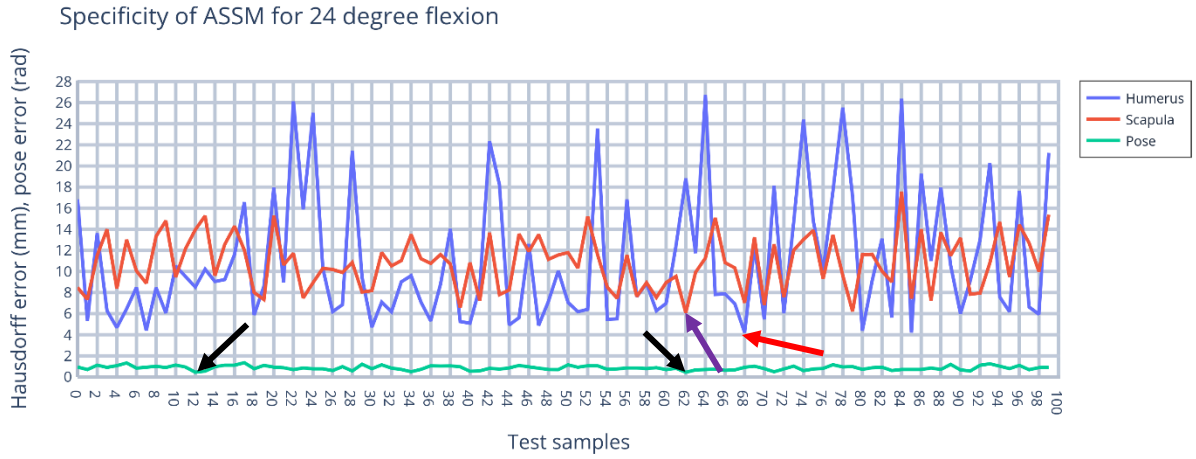

Figure A.27. Specificity of ASSM for 24^0 flexion

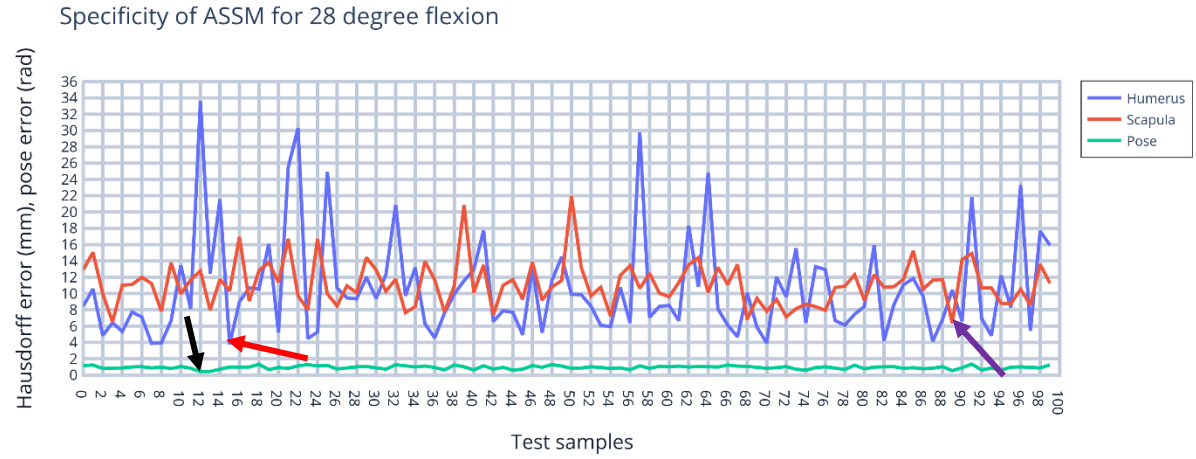

Figure A.28. Specificity of ASSM for 28^0 flexion

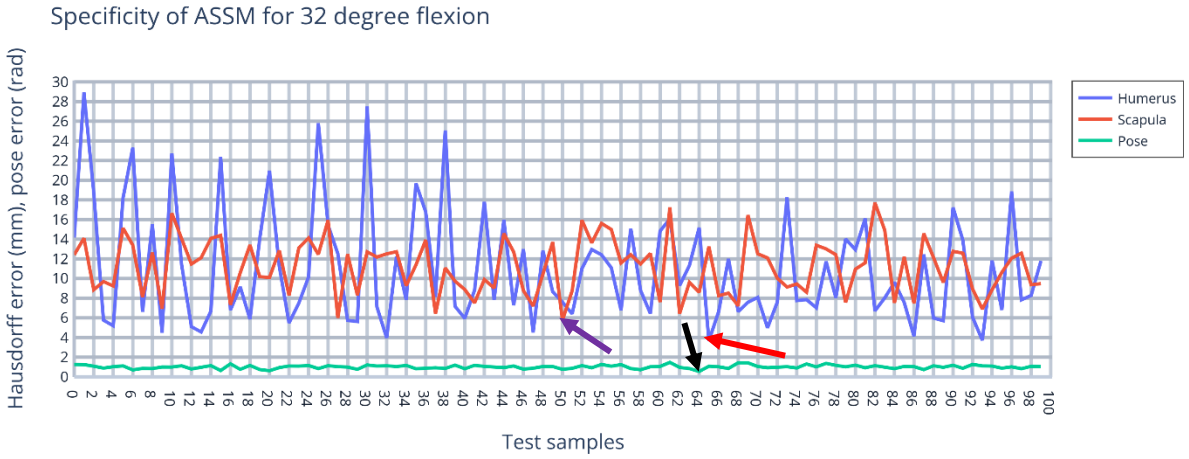

Figure A.29. Specificity of ASSM for 32^0 flexion

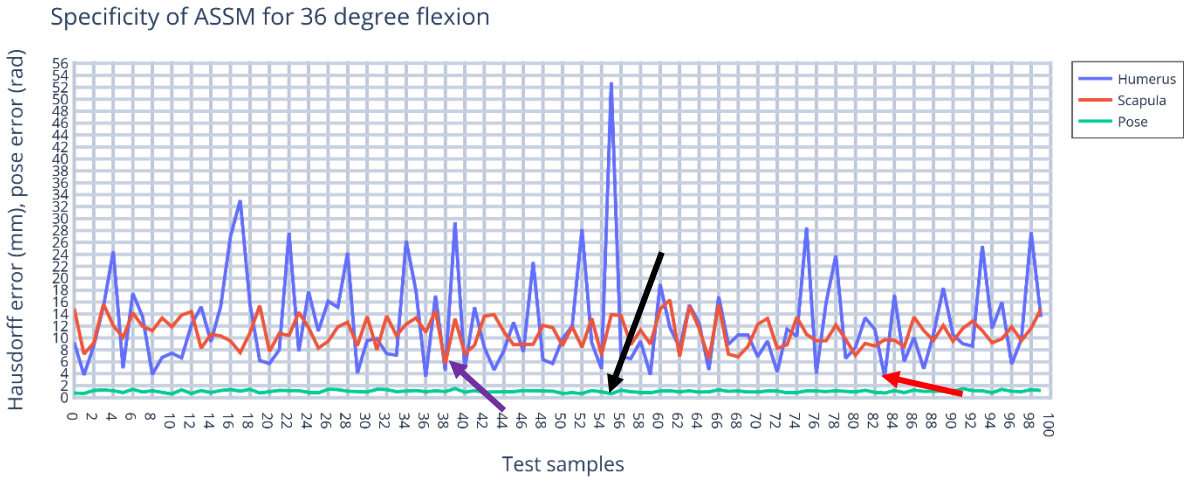

Figure A.30. Specificity of ASSM for 36^0 flexion

Generality

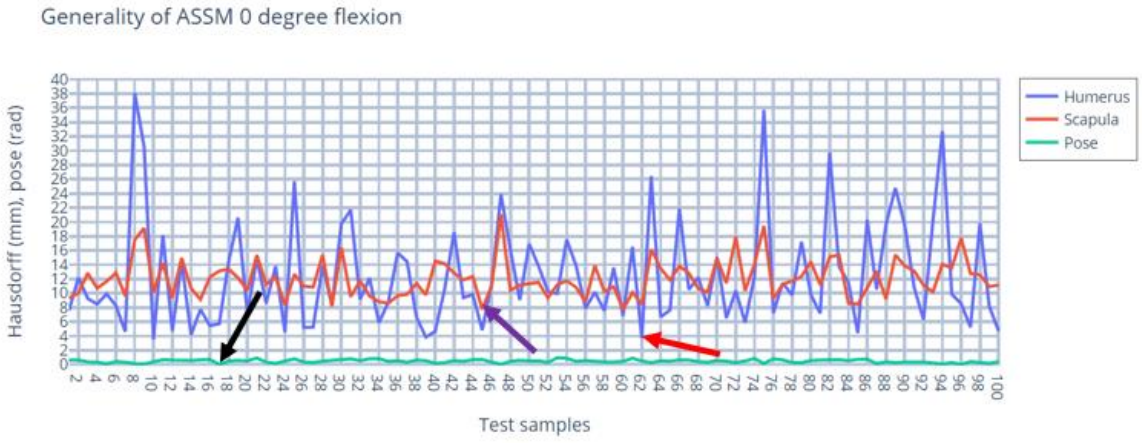

Figure A.31. Generality of ASSM for 0^0 flexion

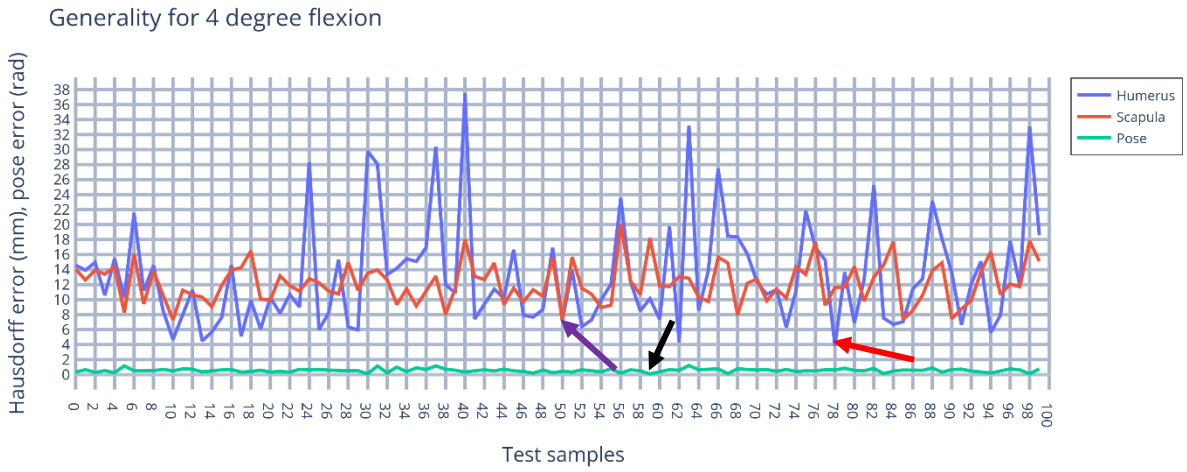

Figure A.32. Generality of ASSM for 4^0 flexion

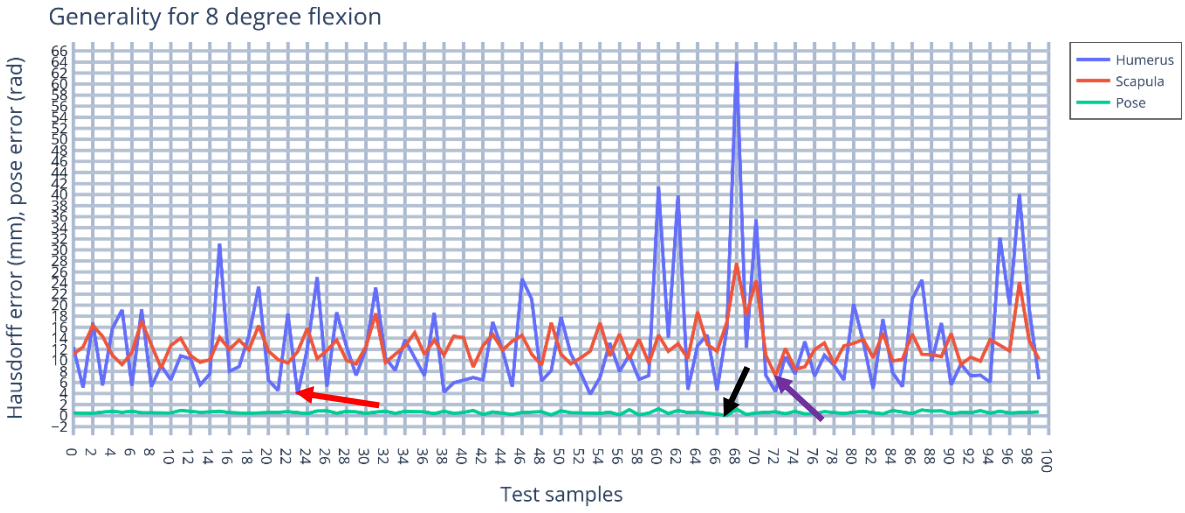

Figure A.33. Generality of ASSM for 8^0 flexion

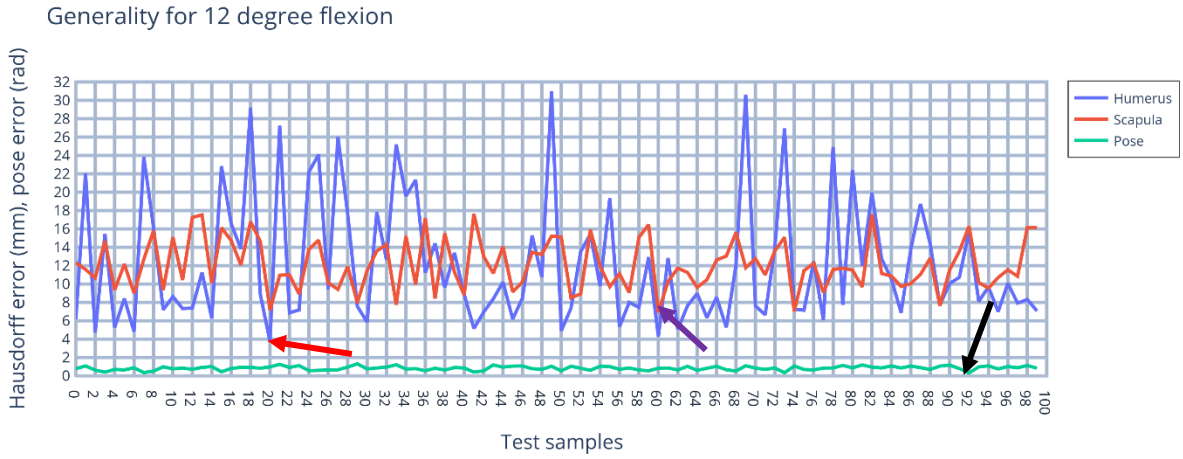

Figure A.34. Generality of ASSM for 12^0 flexion

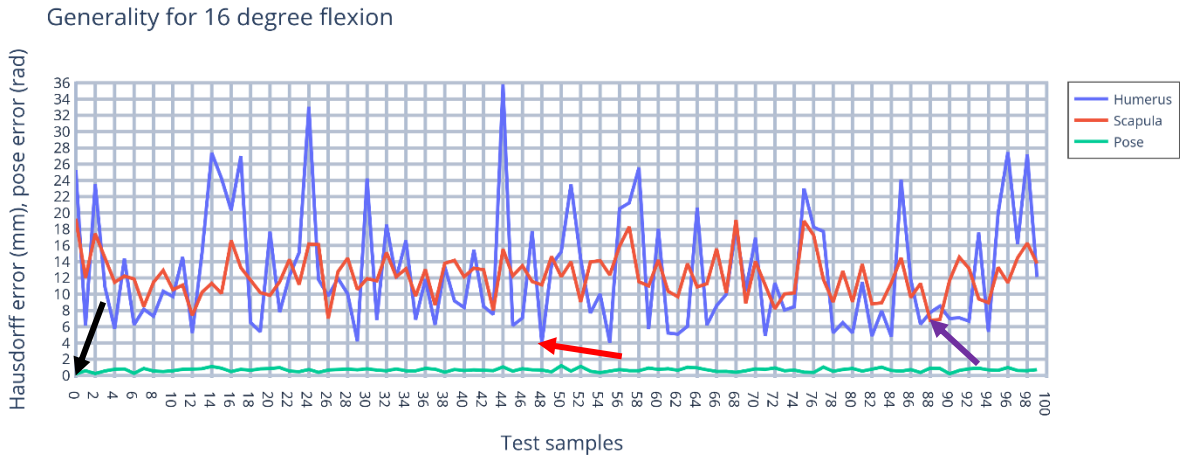

Figure A.35. Generality of ASSM for 16^0 flexion

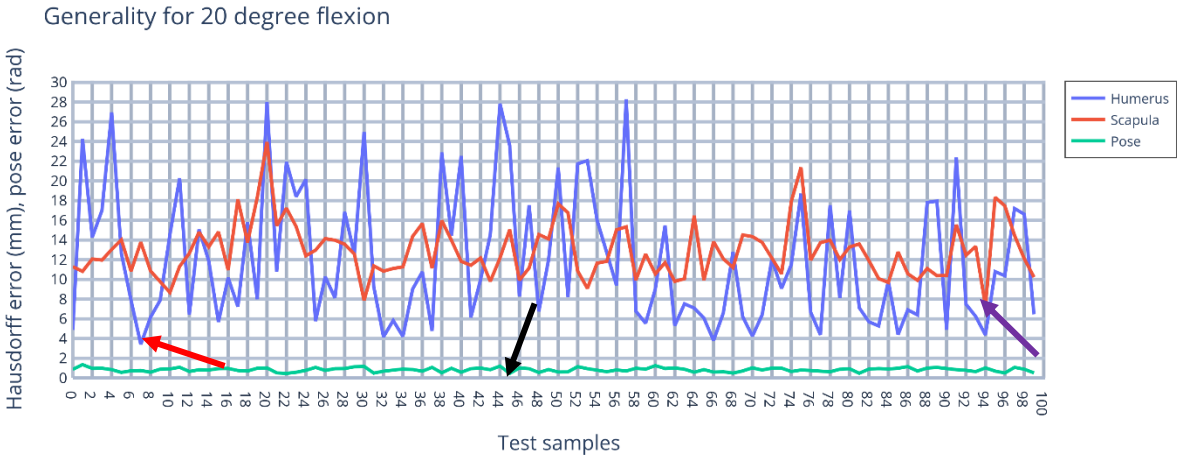

Figure A.36. Generality of ASSM for 20^0flexion

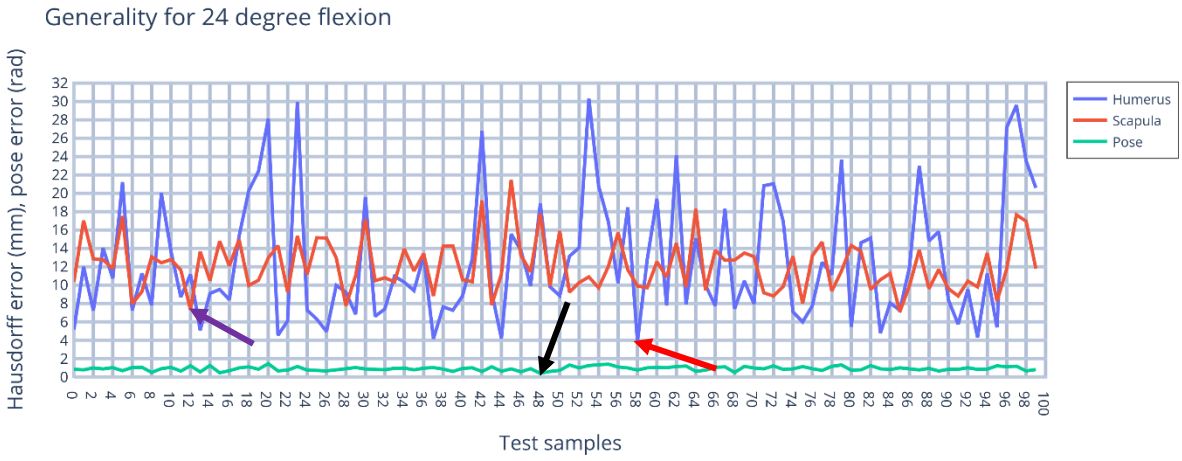

Figure A.37. Generality of ASSM for 24^0 flexion

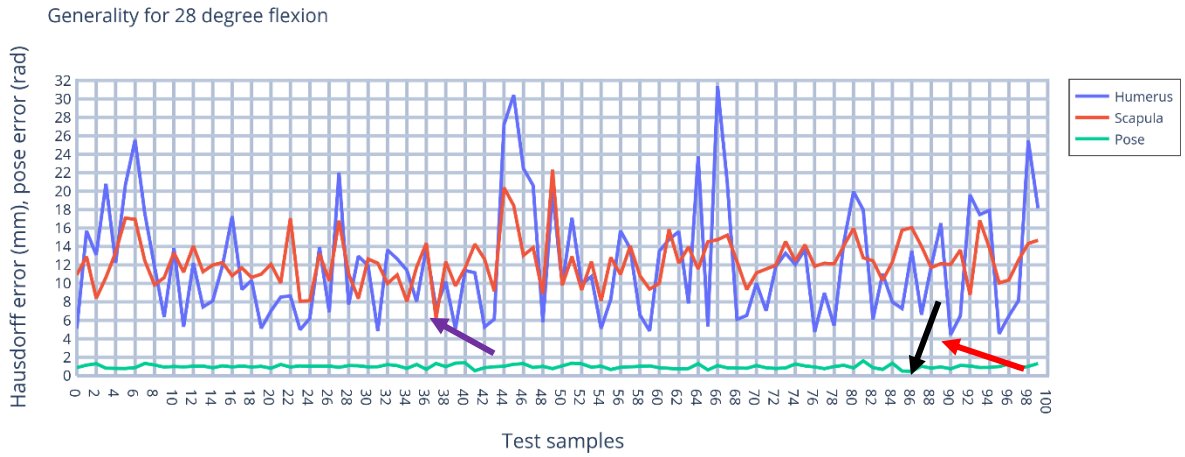

Figure A.38. Generality of ASSM for 28^0 flexion

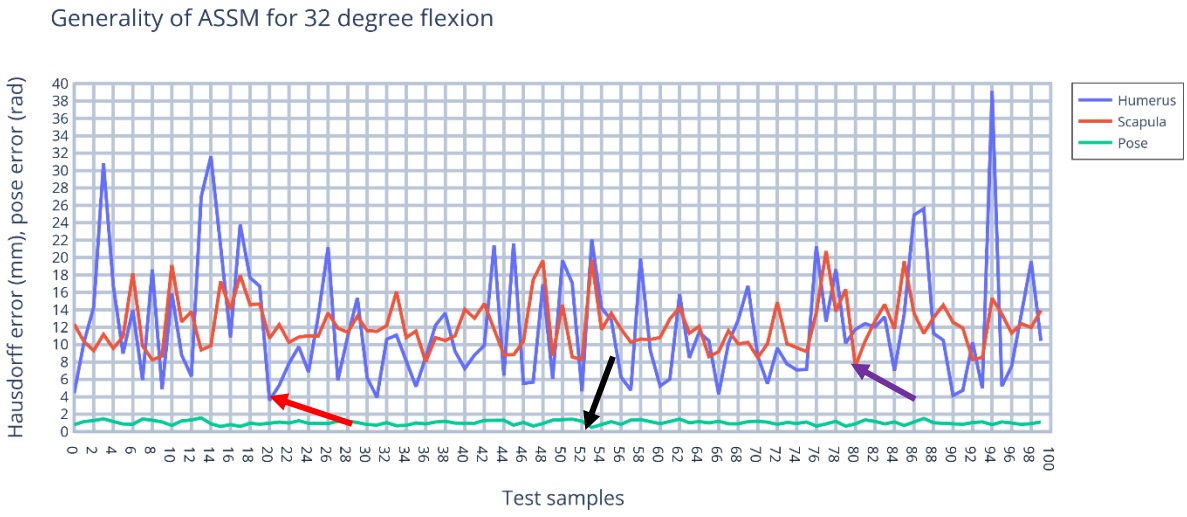

Figure A.39. Generality of ASSM for 32^0 flexion

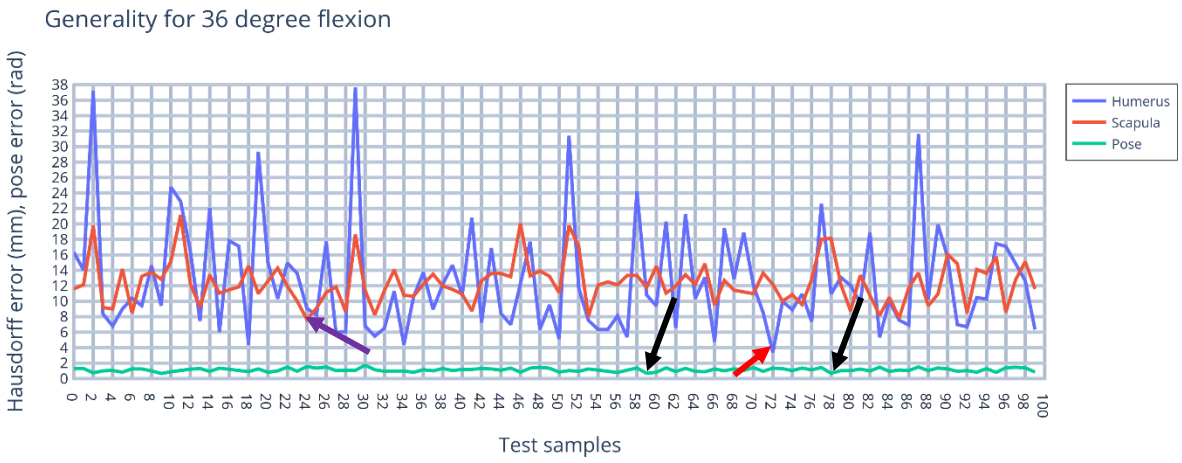

Figure A.40. Generality of ASSM for 36^0 flexion

A.3. Internal rotation validation results

Specificity

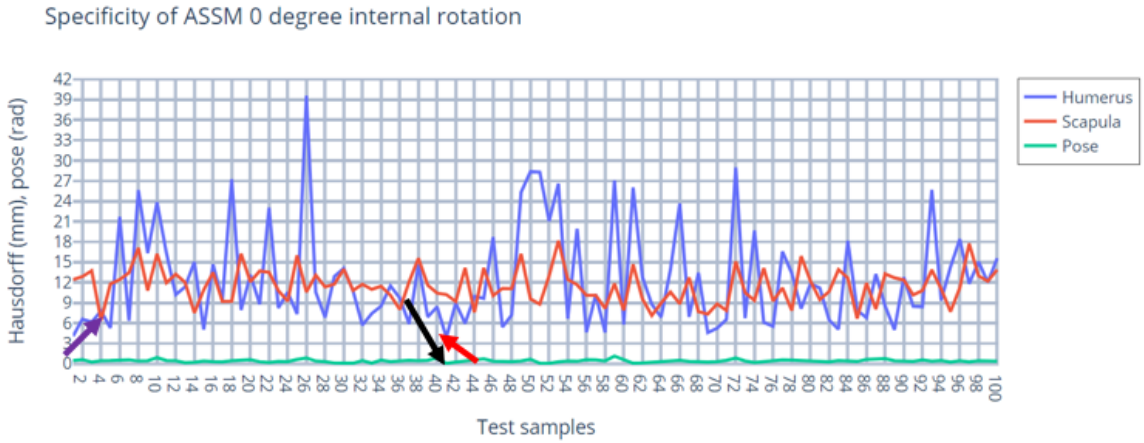

Figure A.41. Specificity of ASSM for 0^0 internal rotation

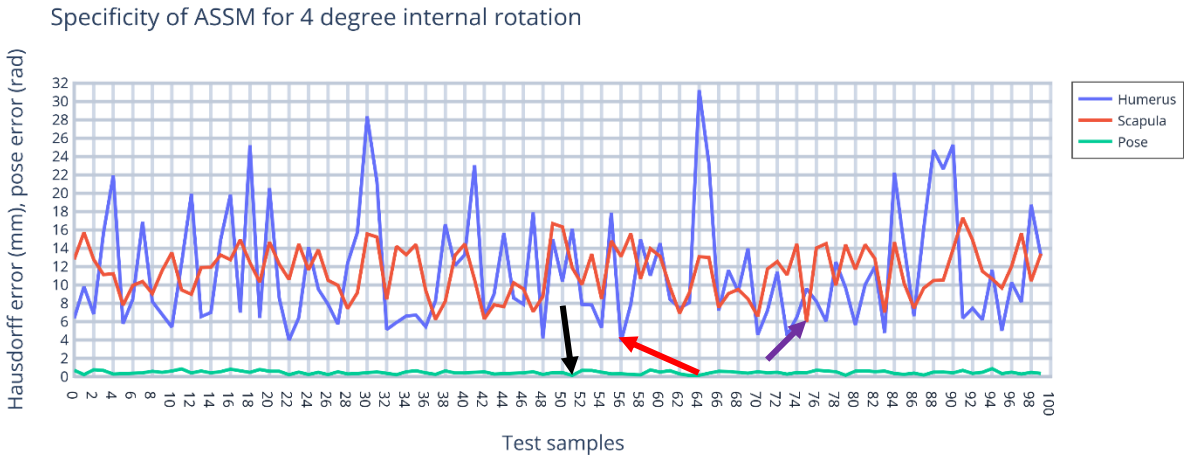

Figure A.42. Specificity of ASSM for 4^0 internal rotation

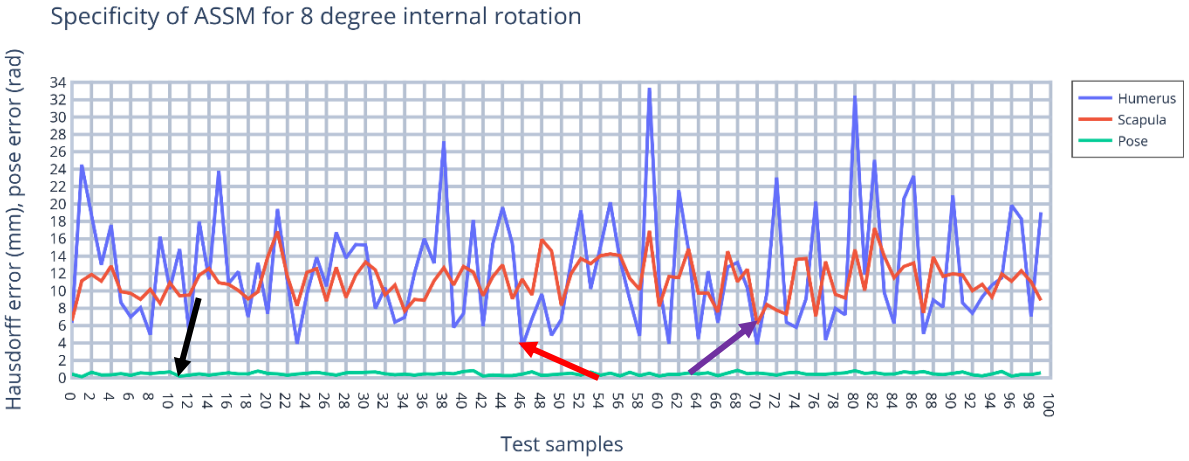

Figure A.43. Specificity of ASSM for 8^0 internal rotation

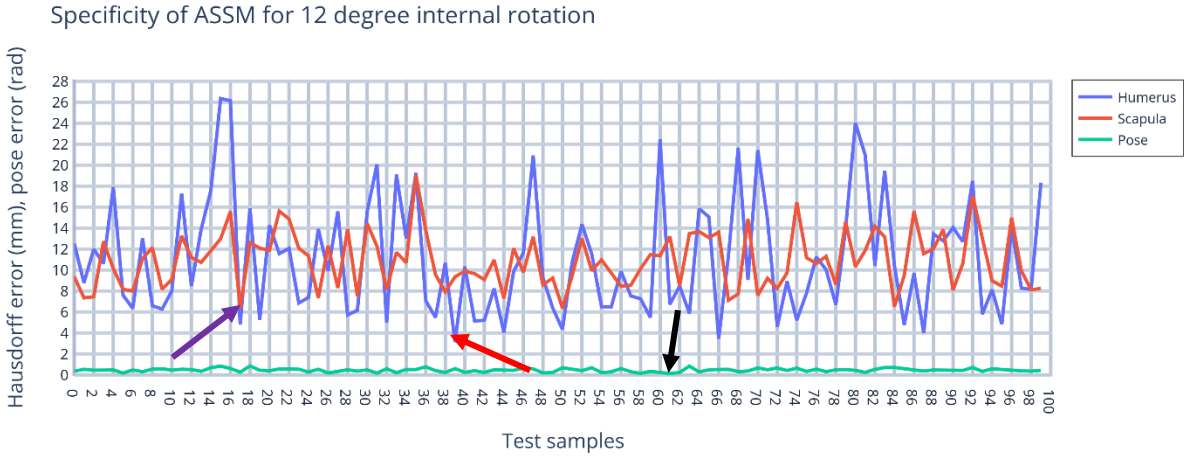

Figure A.44. Specificity of ASSM for 12^0 internal rotation

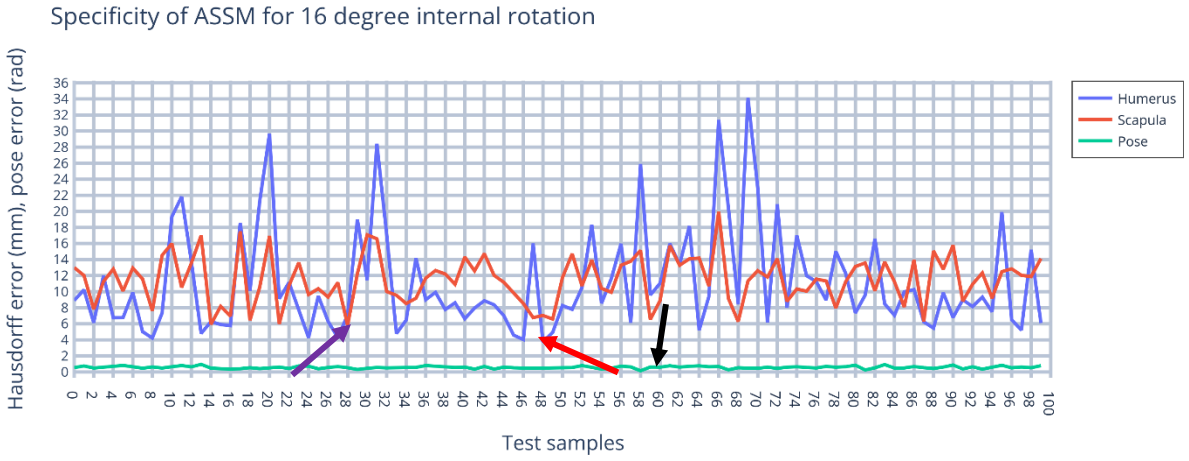

Figure A.45. Specificity of ASSM for 16^0 internal rotation

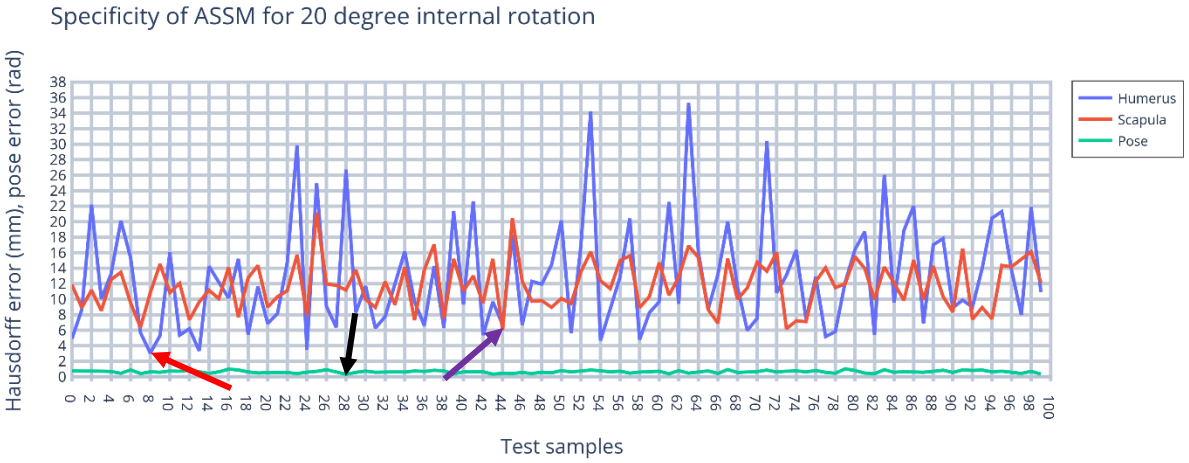

Figure A.46. Specificity of ASSM for 20^0 internal rotation

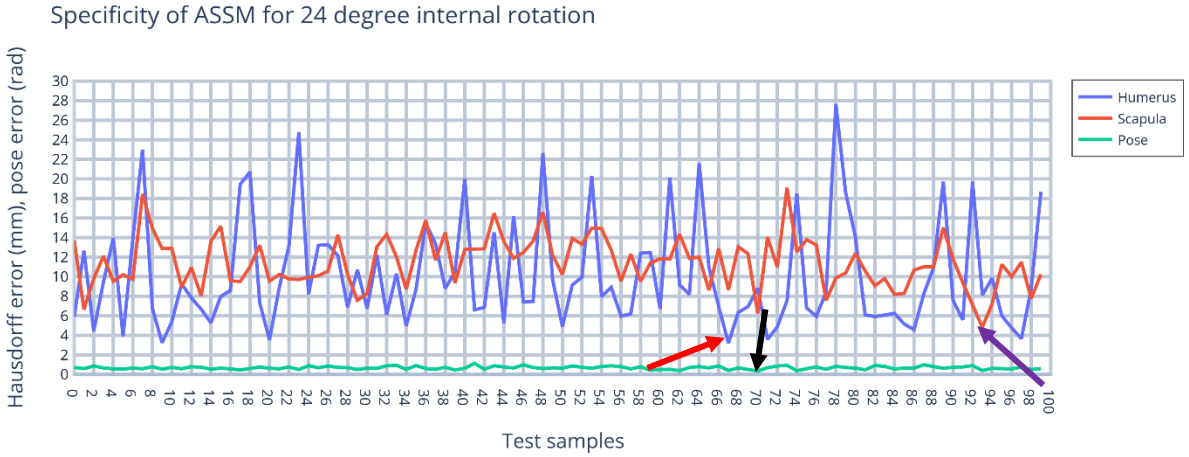

Figure A.47. Specificity of ASSM for 24^0 internal rotation

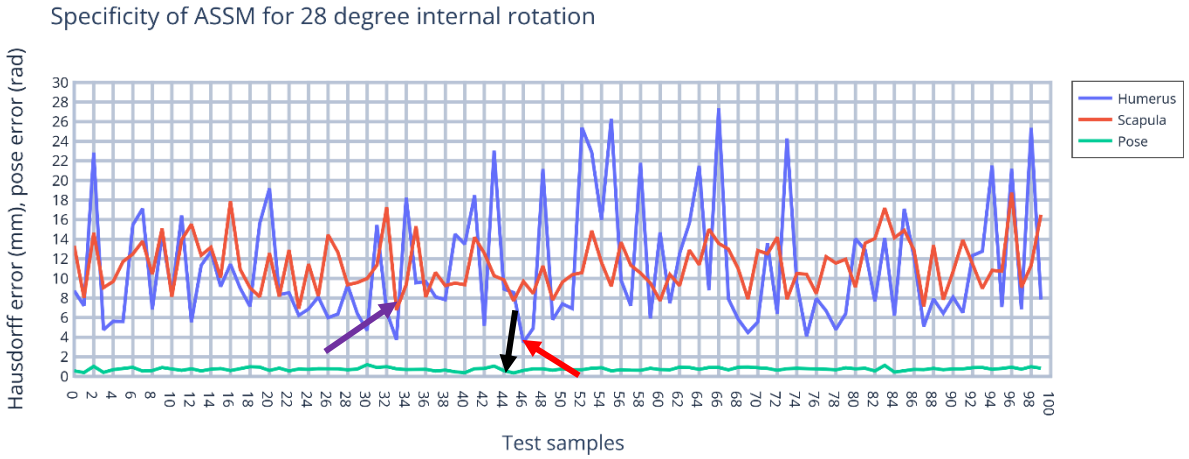

Figure A.48. Specificity of ASSM for 28^0 internal rotation

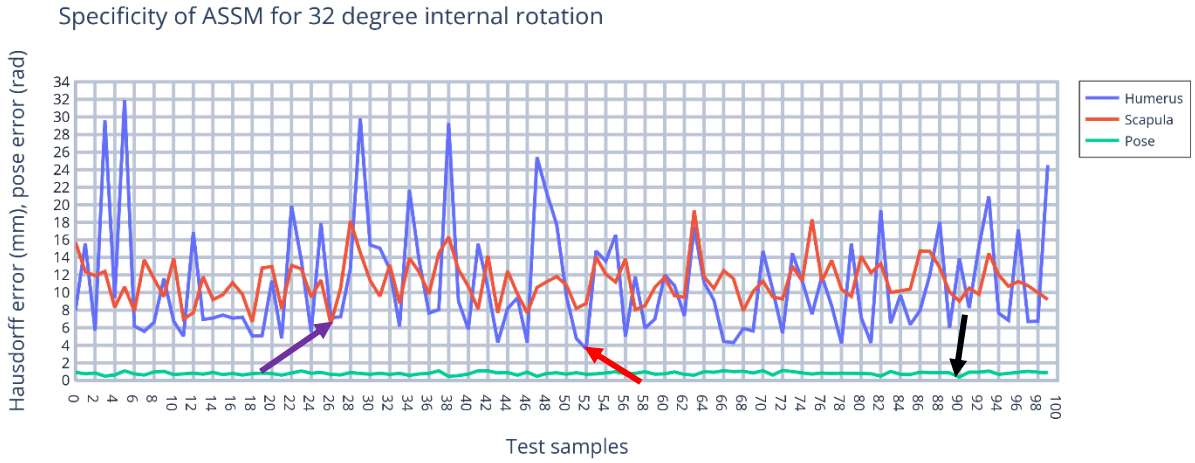

Figure A.49. Specificity of ASSM for 32^0 internal rotation

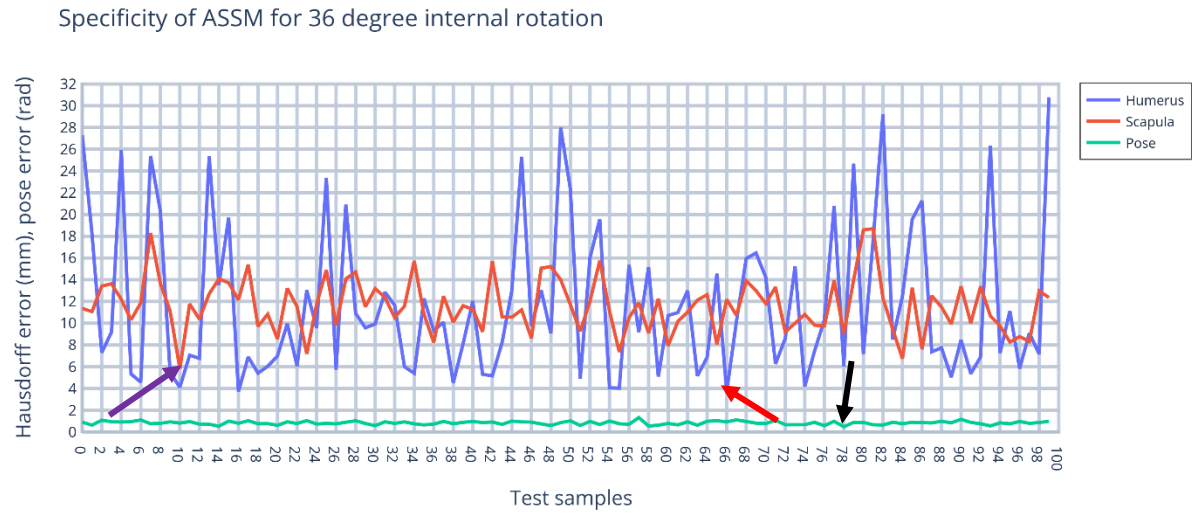

Figure A.50. Specificity of ASSM for 36^0 internal rotation

Generality

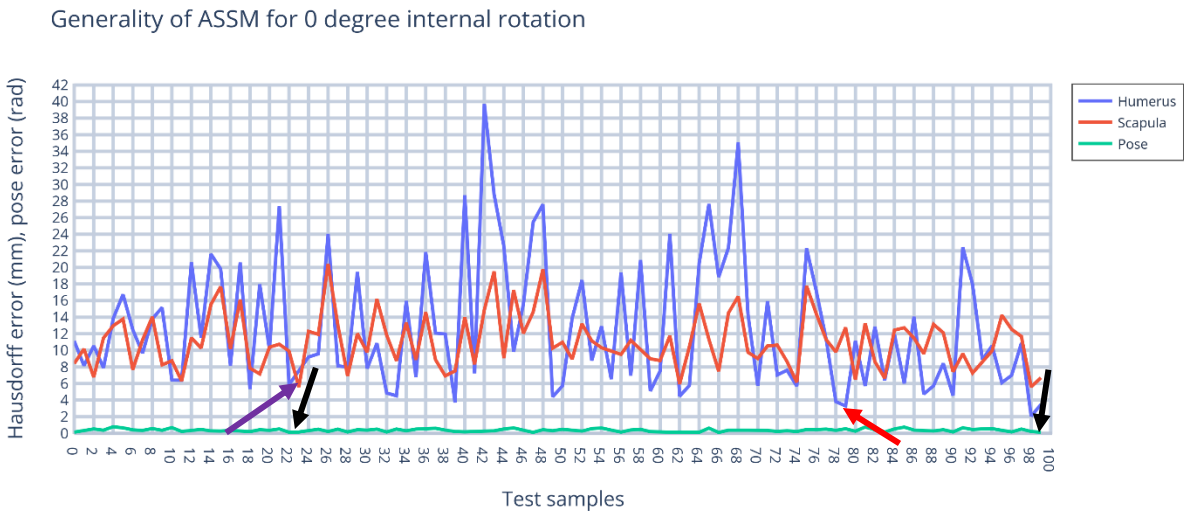

Figure A.51. Generality of ASSM for 0^0 internal rotation

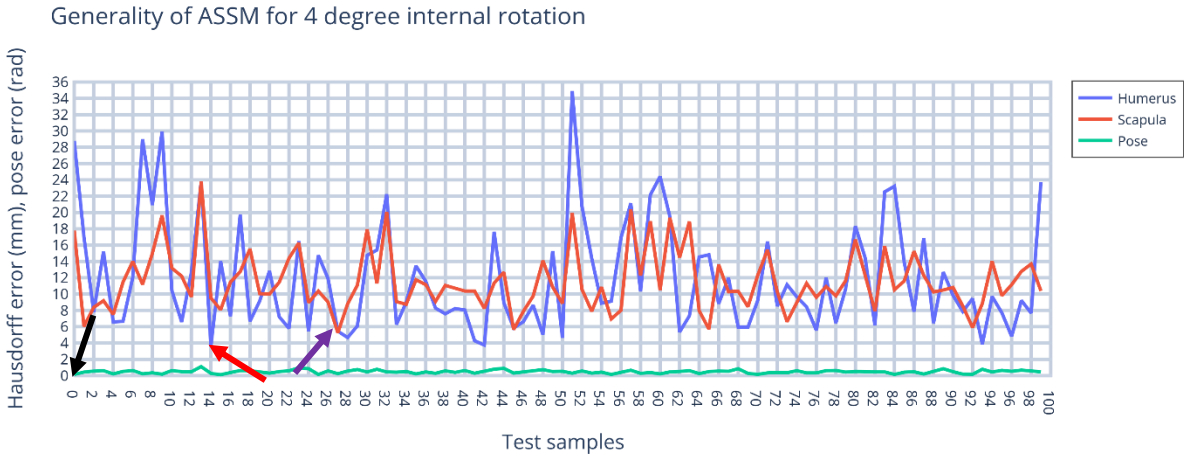

Figure A.52. Generality of ASSM for 4^0 internal rotation

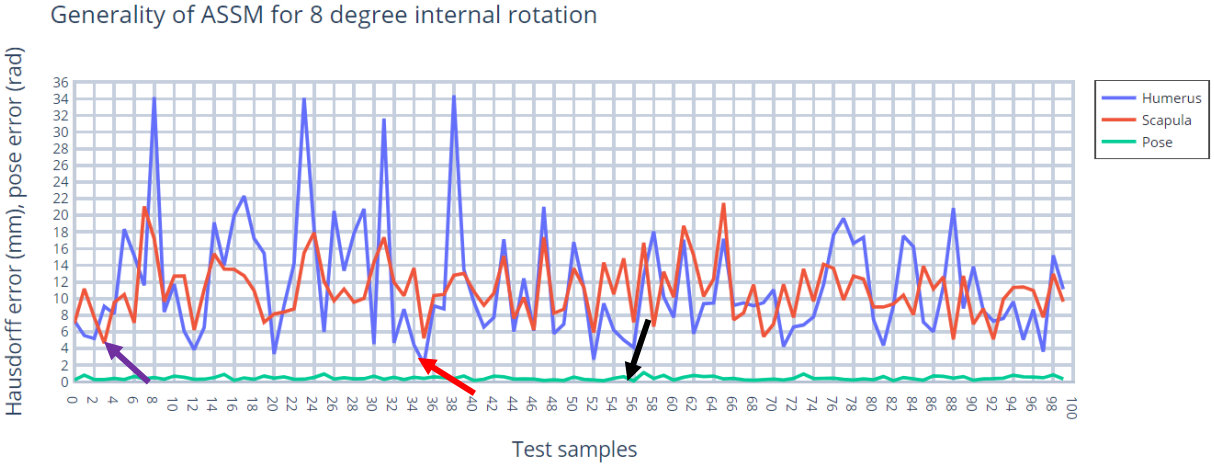

Figure A.53. Generality of ASSM for 8^0 internal rotation

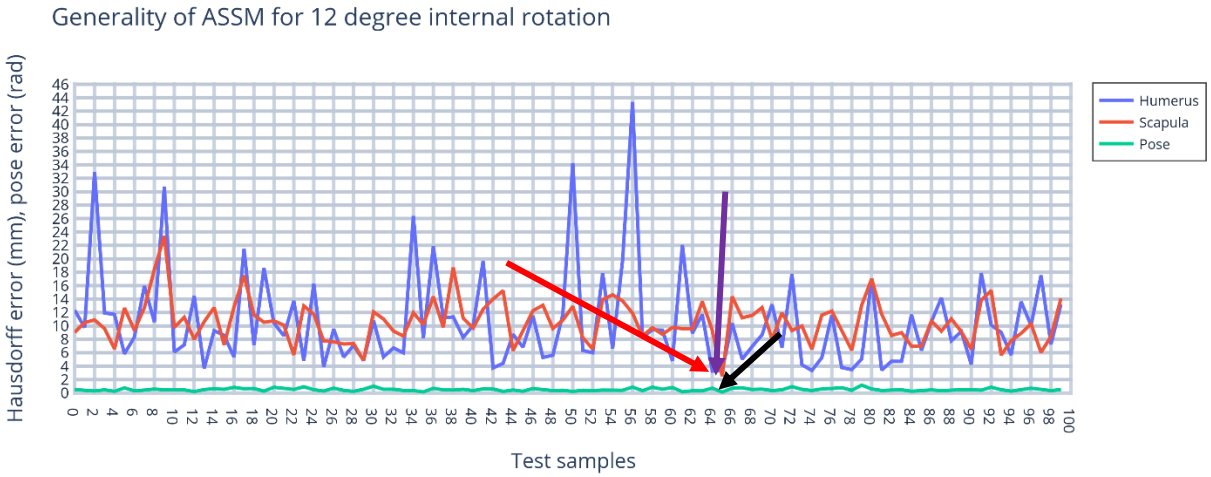

Figure A.54. Generality of ASSM for 12^0 internal rotation

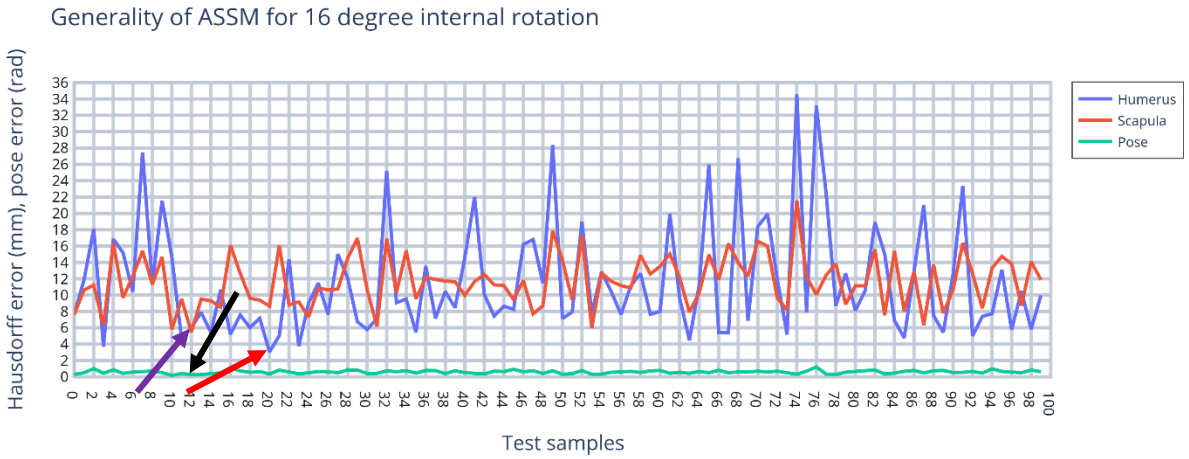

Figure A.55. Generality of ASSM for 16^0 internal rotation

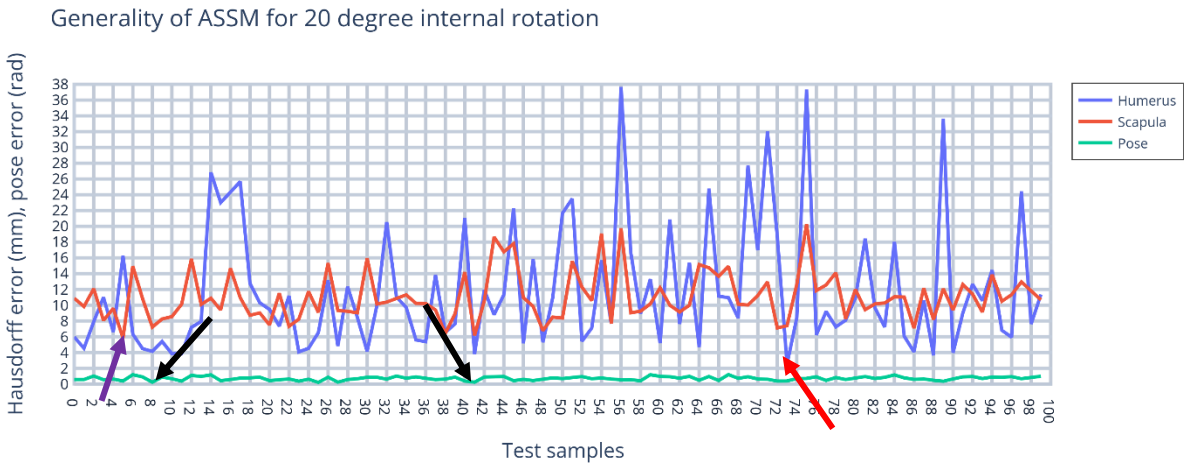

Figure A.56. Generality of ASSM for 20^0 internal rotation

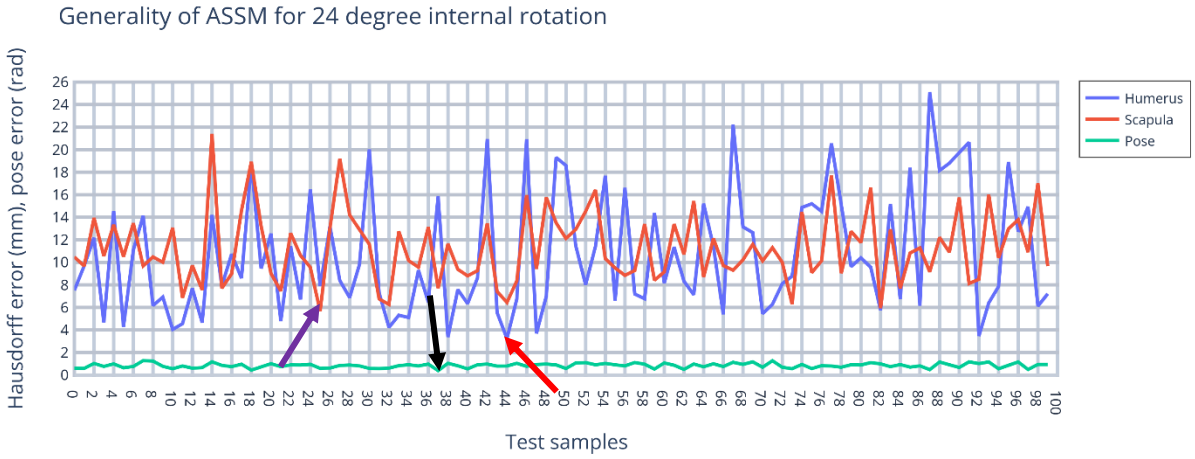

Figure A.57. Generality of ASSM for 24^0 internal rotation

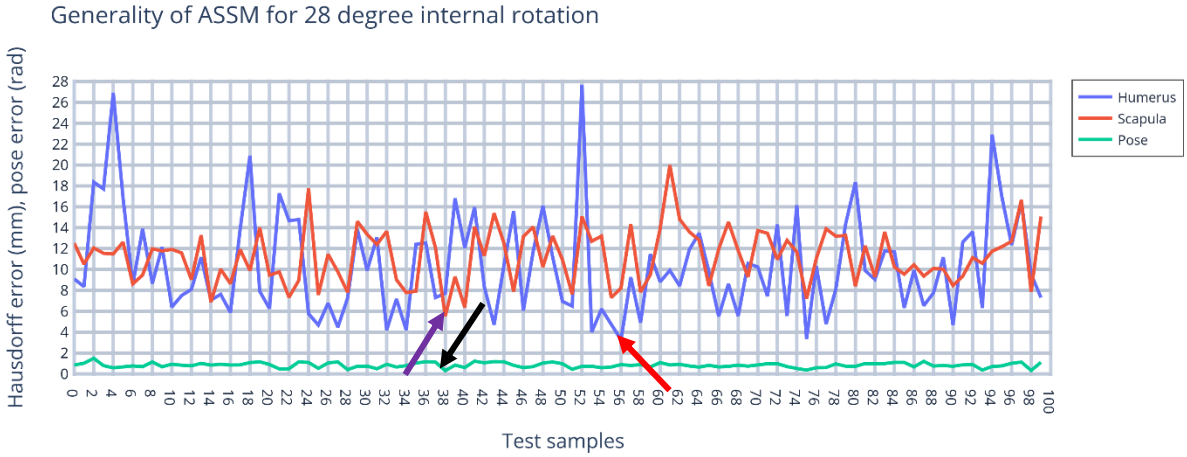

Figure A.58. Generality of ASSM for 28^0 internal rotation

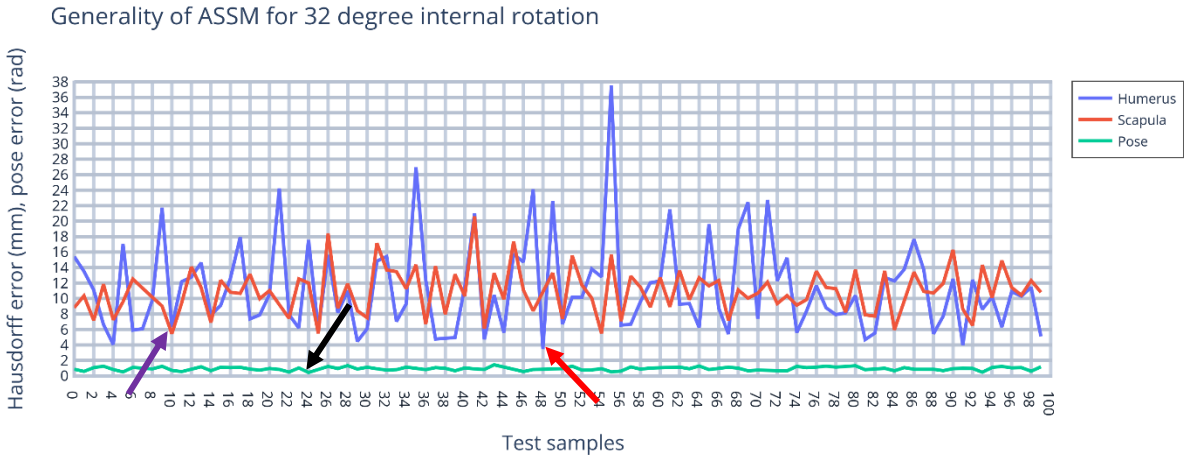

Figure A.59. Generality of ASSM for 32^0 internal rotation

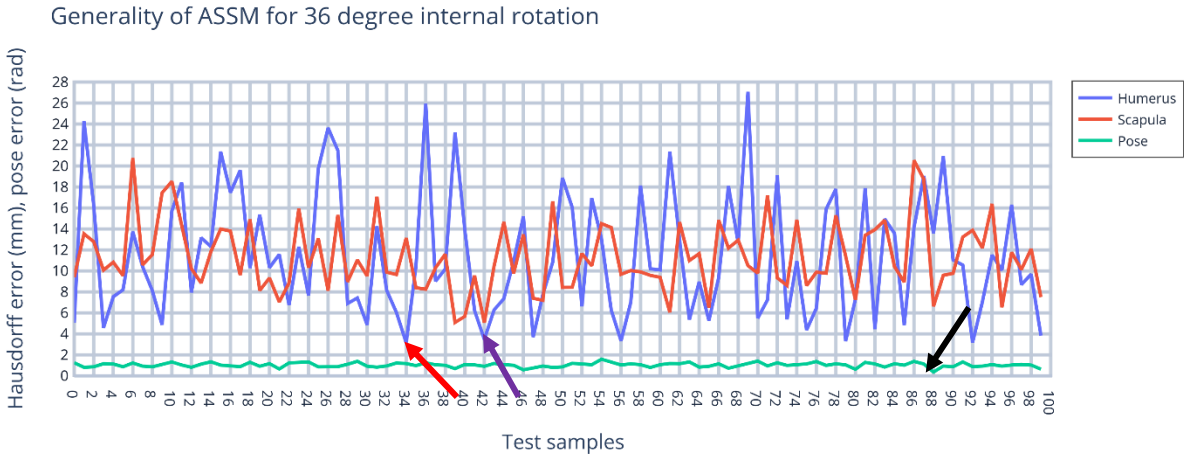

Figure A.60. *Generality of ASSM for 36^0 internal rotation*